UNIVERSIDADE FEDERAL DE MINAS GERAIS
Programa de Pós-Graduação em Engenharia Metalúrgica, Materiais e de Minas

Tese de Doutorado

# "Efeito da deformação a frio e recozimento sobre a microestrutura, textura e propriedades mecânicas de um aço baixo C contendo 17%Mn"

Autora: Sara Silva Ferreira de Dafé
Orientador: Prof. Dr. Dagoberto Brandão Santos

Dezembro de 2013

UNIVERSIDADE FEDERAL DE MINAS GERAIS
Programa de Pós-Graduação em Engenharia Metalúrgica, Materiais e de Minas

Sara Silva Ferreira de Dafé

# "Efeito da deformação a frio e recozimento sobre a microestrutura, textura e propriedades mecânicas de um aço baixo C contendo 17%Mn"

# "Effect of cold rolling and annealing on the microstructure, texture and mechanical properties of a 17%Mn TRIP/TWIP steel with low C"

Tese de Doutorado apresentada ao Programa de Pós-Graduação
em Engenharia Metalúrgica, Materiais e de Minas
da Universidade Federal de Minas Gerais

Área de concentração: Metalurgia Física
Orientador: Prof. Dr. Dagoberto Brandão Santos

Belo Horizonte
Escola de Engenharia da UFMG
2013

**AGRADECIMENTOS**

Primeiramente agradeço a Deus e a Maria pelas oportunidades e por me darem forças e determinação para concluir este trabalho.

Aos meus pais, Darcy e Magda Ferreira, e ao meu irmão, Gessé Dafé, pelo apoio e amor incondicionais e inesgotáveis.

Ao meu namorado Marcos Flávio Taveira pelo carinho, incentivo e companheirismo diário.

Ao Prof. Dr. Dagoberto Santos pela credibilidade e pelo aprendizado proporcionado por sua orientação e amizade.

Aos servidores Patrícia Azevedo, Andréia Bicalho e Estevesson Miqueletti por não medirem esforços em colaborar com a produção e/ou análise das amostras. Em especial, à Patrícia Azevedo pela amizade e incentivo constante, mesmo a distância.

Ao Dr. Denilson José do Carmo e ao Serviço Nacional de Aprendizagem Industrial (SENAI)/Centro Tecnológico de Fundição Marcelino Corradi (CETEF), Itaúna-MG, pelas análises de dilatometria.

À Prof. Dra. Berenice Mendonça Gonzalez e ao Felipe Gustavo Gomes Cunha pelos ensaios de tração.

Não só agradeço, como parabenizo, os alunos de iniciação científica, os quais foram colaboradores diretos das análises realizadas no Brasil (Capítulos 3, 4 e 5): Mirelle Oliveira Spindola, Débora Rezende Moreira, Felipe Lucas Sicupira, Flávia Cristina Silva Matos, Naiara Silva Cruz, Patrícia Bertolini Valadão, Thiara Francis Martins Rodrigues e Luiz Paulo Torres. O êxito do sucesso deve-se ao trabalho de uma grande equipe como esta.

I am very grateful to PhD. Andrii Kostryzhev, University of Wollongong, Australia, for his teachings and great effort on TEM analysis, as well as for his friendship. Thank you for everything!

I would like to thank Greg Tillman (Mettalografy Laboratory, University of Wollongong, Australia) for his friendship and also for his assistance in the hardness Vickers measurements and preparation of XRD, EBSD and TEM samples.

I thank Prof. Elena Pereloma and the Electron Microscopy Center (EMC), University of Wollongong, Australia, for the doctoral internship and for the hardness Vickers, EBSD, XRD and TEM analysis.

Ao PPGEM pela oportunidade.

À CAPES pela bolsa de doutorado no Brasil e pela bolsa de doutorado sanduíche no exterior (PDSE), processo n. 0804-12-6 do Programa Ciência sem Fronteiras, Ministério da Educação, Brasil.

De forma geral, a todos os amigos e familiares que torceram por mim e me incentivaram durante os quatro anos desta jornada.

Ao Skype®, Microsoft, por encurtar distâncias e estreitar laços afetivos em momentos difíceis.

“O saber a gente aprende com os mestres e os livros.
A sabedoria se aprende é com a vida
e com os humildes.”
Cora Coralina
(1889-1985)

**SUMMARY**

**LIST OF FIGURES**

**LIST OF TABLES**

## LIST OF SYMBOLS

| | |
|---|---|
| a | lattice parameter |
| AHSS | Advanced High-Strength Steel |
| AS | air cooled sample |
| b | Burgers vector |
| bcc | body centered cubic |
| CR | cold rolled |
| d | molar surface density |
| D | crystallite size |
| DP | Dual-Phase |
| EBSD | Electron Backscatter Diffraction |
| FEG | Field Emission Gun |
| fcc | face centered cubic |
| FS | furnance cooled sample |
| FWHM; B | full-width at half maximum |
| GOF | goodness of fit |
| HAGBs | high angle grain boundaries |
| hcp | hexagonal close packed |
| $HV_{CR}$ | Hardness Vickers of cold rolled sample |
| $HV_s$ | Hardness Vickers of completely austenitic sample |
| $HV_X$ | Hardness Vickers of completely annealed sample |
| IPF | inverse pole figure |
| IQ | image quality |
| K | Form factor |
| K-S OR | Kurdjumov-Sachs orientation relationship |
| LAGBs | low angle grain boundaries |
| $M_s$ | $\alpha$' martensite starting temperature |
| $M_{\varepsilon s}$ | $\varepsilon$ martensite starting temperature |
| MAUD | Materials Analysis Using Diffraction |
| n | strain hardening exponent |
| ND | normal direction |

| | |
|---|---|
| ODF | Orientation Distribution Function |
| OR | orientation relationship |
| PAGS | prior austenite grain size |
| RD | rolling direction |
| $R_W$ | expected error |
| $R_{exp}$ | weighed residual error |
| SEM | Scanning Electron Microscopy |
| SFE; Γ | stacking fault energy |
| S-N OR | Shoji- Nyshiyama orientation relationship |
| T | temperature |
| $T_N^{\varphi}$ | Néel temperature |
| TD | transversal direction |
| TBs | twin boundaries |
| TEM | Transmission Electron Microscopy |
| THAGBs | total high angle grain boundaries |
| TRIP | Transformation Induced Plasticity |
| TWIP | Twinning Induced Plasticity |
| V | full-width at half maximum for a standard sample |
| $x_i$ | mole fraction of each chemical element |
| XRD | X-Ray Diffraction |
| WD | work distance |
| α’ | α’ martensite |
| $\beta^{\varphi}$ | magnetic moment |
| $\beta_i^{\varphi}$ | magnetic moment contribution of element *i* in phase ϕ |
| γ | austenite |
| $\Delta G^{\gamma\rightarrow\varepsilon}$ | molar Gibbs free energy of γ→ε transformation |
| $\Delta G_{FeMnX}^{\gamma\rightarrow\varepsilon}$ | molar Gibbs free energy contribution of substitutional chemical elements in fcc structure |
| $\Delta G_{FeMnX/C}^{\gamma\rightarrow\varepsilon}$ | molar Gibbs free energy associated with the carbon content in combination with the manganese content |

| | |
|---|---|
| $\Delta G_{mg}^{\gamma \to \varepsilon}$ | molar Gibbs free energy due to néel magnetic transition |
| $\varepsilon$ | ε martensite |
| $\left\langle \varepsilon^2 \right\rangle^{1/2}$ | microstrain |
| $\lambda$ | wavelength |
| $\mu_\beta$ | Bohr magneton |
| $\rho$ | dislocation density |
| $\Sigma_3$ | twin boundaries of first order |
| $\Sigma_9$ | twin boundaries of second order |
| $\sigma^{\gamma \to \varepsilon}$ | surface energy associated with γ/ε interface |
| *%Soft* | softened fraction |

**RESUMO**

Os aços com teores elevados de Mn, Si e Al apresentam uma boa conformabilidade aliada a uma elevada resistência mecânica. Este excelente desempenho mecânico ocorre devido à maclação, efeito conhecido como TWIP (Twinning Induced Plasticity), ou à transformação martensítica, este denominado TRIP (Transformation Induced Plasticity). Atualmente, a ductilidade e a conformabilidade são parâmetros importantes na fabricação dos componentes externos automotivos, pois favorecem a estampagem, além de proporcionarem maior segurança aos passageiros em eventuais colisões. Este trabalho teve como objetivo a avaliação microestrutural e da textura cristalográfica, bem como a influência destes parâmetros sobre o comportamento mecânico de um aço TRIP/TWIP contendo 17%Mn. A energia de falha de empilhamento para este material é de 14,5 $mJ/m^2$, indicando a ocorrência de transformação martensítica e maclação como mecanismos de deformação. Foi verificado que a cinética de transformação de fases, austenita em martensita $\varepsilon$ e $\alpha$', é favorecida por um maior tempo de resfriamento. O efeito TRIP mostrou-se responsável pelo aumento da capacidade de encruamento devido à transformação martensítica. Quando martensita $\alpha'$ reverte-se em austenita há ocorrência do mecanismo de reversão por cisalhamento juntamente com o de difusão. A reversão da austenita é mais eficaz e mais rápida a temperaturas mais elevadas quando se tem uma maior energia armazenada na deformação. Este processo é concluído a 700°C independente da quantidade de deformação na laminação a frio. Provou-se também que a transformação martensítica ocorre em duas etapas: $\gamma \rightarrow \varepsilon \rightarrow \alpha'$ e que a martensita $\alpha'$ tende a ser a fase majoritária com o aumento da deformação. As diferenças de orientação nos contornos das fases mostraram-se correspondentes à relação de orientação de Kurdjumov-Sachs (K-S) entre austenita e martensita $\alpha'$ e do tipo Shoji–Nishiyama (S-N) entre a martensita $\varepsilon$ e a austenita. Os resultados de textura mostraram que a reversão da austenita ocorre sem recristalização simultânea, uma vez que a componente Cubo não foi observada em amostras recozidas até 700ºC. Durante o recozimento a componente Goss tende a dar lugar à componente Latão na austenita. Esse fato é benéfico, pois esta componente torna-se {332}<113> na martensita $\alpha'$ após a transformação de fases, podendo proporcionar boa formabilidade, bem como alta resistência e tenacidade ao material.

**ABSTRACT**

Steels containing high Mn, Si and Al have a great formability combined with a high mechanical strength. This excellent mechanical performance occurs due to twinning, TWIP effect (Twinning Induced Plasticity), or martensitic transformation, called TRIP effect (Transformation Induced Plasticity). Currently, the ductility and formability are two important parameters in external automotive components manufacture, due to favoring of drawing and providing greater safety for passengers in eventual collisions. This study evaluated the microstructure and crystallographic texture, as well as the influence of these parameters on the mechanical behavior of a TRIP/TWIP steel containing 17% Mn. The stacking fault energy for this material is 14.5 $mJ/m^2$, indicating the occurrence of martensitic transformation and twinning as deformation mechanisms. It was checked that phase transformation kinetics is favored by a longer cooling time. TRIP effect was assumed to enhance the hardening ability due to the martensitic transformation. When α' martensite reverts into shearing occurs together with diffusion mechanism. Austenite reversion is more effective and faster at higher temperatures and when it has greater stored energy from deformation. This process completes at 700°C regardless of the cold deformation amount in cold rolling. It was also proved that the martensitic transformation occurs in two steps γ → ε → α' and that α' martensite tends to be the major phase with the deformation increasing. The misorientations at phase boundaries were shown to be corresponding to Kurdjumov-Sachs (K-S) orientation relationship between austenite and α' martensite and to Shoji–Nishiyama (S-N) between ε martensite and austenite. Texture results proved that the reversion of austenite occurs without simultaneously recrystallization once the Cube component was not observed in annealed samples until 700ºC. As annealing proceeds, Goss component tends to give place to Brass in austenite. This fact is beneficial because it becomes {332}<113> in α' martensite after phase transformation and could promote good formability as well as high strength and toughness to the material.

## CHAPTER 1: Introduction

There is a constant demand by customers on safer and more economic cars. On the other hand, governments worldwide have regulating more strictly crashworthiness as well as the greenhouse gas emission. In this direction, steel and automotive industries feel the responsibility to lead the way by improving the use of steel and its life cycle to reduce vehicle $CO_2$ emission.

One important parameter which is essential to evaluate greenhouse gas emission is the life cycle assessment approach. It assists automakers in evaluating and reducing the total energy consumed and greenhouse gas emissions of their products.

Projects which consider just the vehicle use for reducing carbon footprint encourage the employment of low-density materials, as aluminum. This can provide lighter weight components that improve fuel economy and then lower greenhouse gas emission. However, these components production will account for a much larger amount of total car life cycle $CO_2$ emission.

Therefore, it is noteworthy that steel is the only material efficient in achieve reductions in all life cycle phases of cars, not only those from the vehicle use. In this sense, worldwide steel industries have been engaged year after year to propose new steel solutions to the challenges of increasing car fuel efficiency and reducing greenhouse gas emissions, while improving safety and performance.

The engineers are developing new materials and designs to reach these aims by reinventing whole new classes of steels that are over 50% stronger than those of a decade ago. At the core of this innovation lie new types of steels as Advanced High-Strength Steel (AHSS), Dual-Phase (DP), Transformation-Induced Plasticity (TRIP) and Twinning-Induced Plasticity (TWIP). These steels are designed to reduce density, improve strength and increase elongation. In addition, they can answer the demand of automakers for stronger and more formable steels needed for lighter structures that meet

increasingly stringent crash requirements. These steels are evidence of continual self-reinvention of materials to meet automotive design challenges.

In this sense this work investigates through thermodynamic, kinetic, crystallographic, microstructural and mechanical studies the properties of a TRIP/TWIP steel with 17% Mn and low C submitted to different thermomechanical processes.

## CHAPTER 2: Overview

### 2.1. Brief review

*2.1.1. The importance of the development of austenitic Fe-Mn alloys*

Currently, ductility and formability are important parameters in the manufacture of external vehicle components. These parameters besides facilitating the draw process also provide greater safety to passengers in possible collisions due to higher energy absorption on impact, as shown in Figure 2.1 for steels with high Mn content[1, 2].

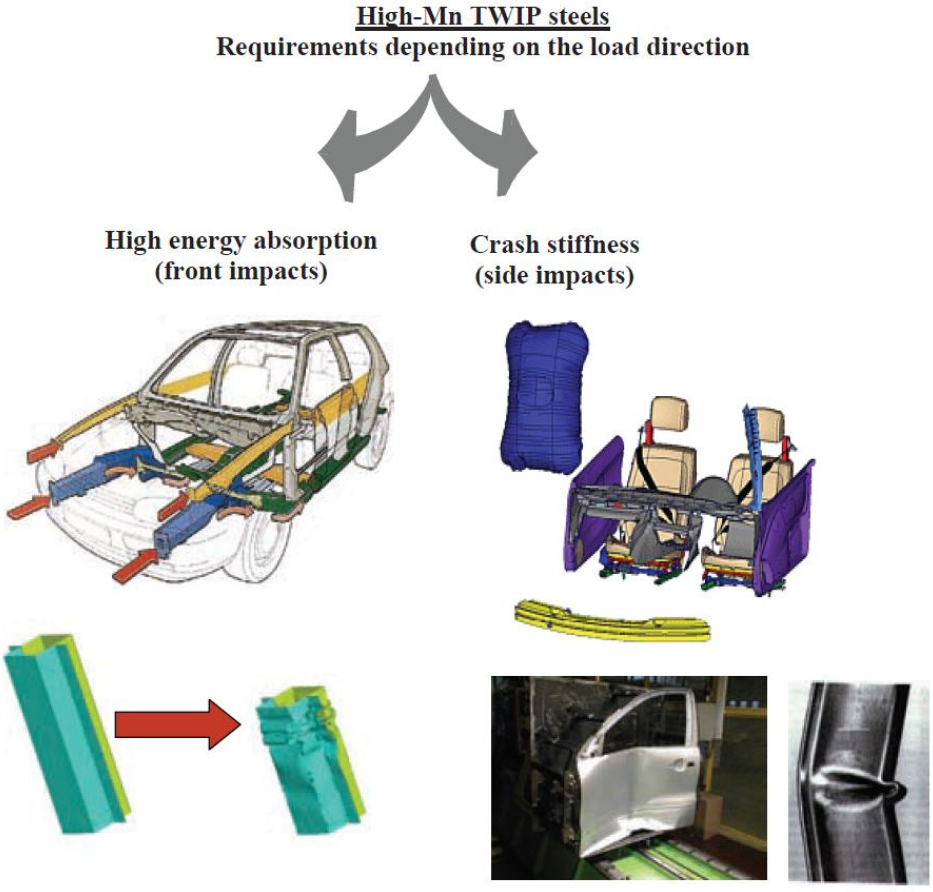


Figure 2.1. Automotive applications of high-Mn steels[1, 2].

In order to obtain good formability combined with a high mechanical strength, new concepts for high-strength steels have been developed. The most important groups of

these new materials are those austenitic alloys based on Fe-Mn, Fe-Mn-C[3-6], Fe-Mn-C-Al[2,7] and Fe-Mn-Si-Al[8, 9].

These new materials have good mechanical properties such as high tensile strength, reaching 1000 MPa, and very high uniform elongation, above 50%, as shown in Figure 2.2[10]. Moreover, these alloys exhibit excellent cost-benefit compared to the austenitic stainless steels, because its processing used is the conventional one, besides having lower content of alloying elements such as Cr and Ni that are present in stainless steels[2,11-13].

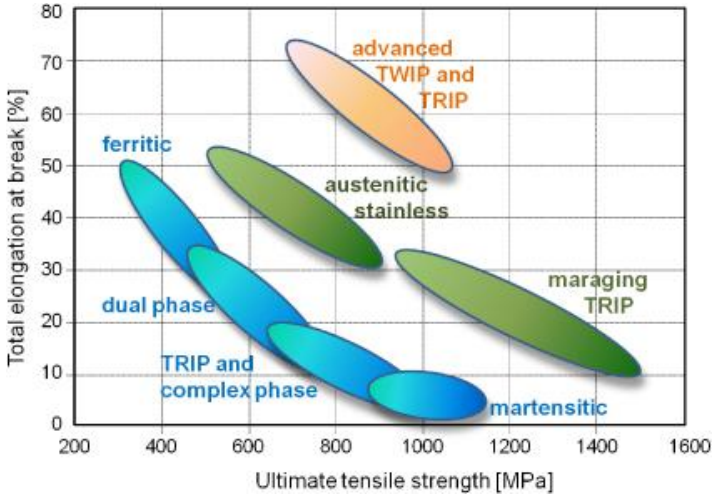


Figure 2.2. Total elongation as a function of the yield strength for various steels[10].

*2.1.2. Deformation mechanisms in TRIP/TWIP steels*

In high manganese austenitic steels with TRIP/TWIP effect, martensite formation can be induced by deformation in reactions which austenite (fcc) transforms into ε martensite (hcp) or in two steps, when austenite transforms initially into ε martensite and then to α' martensite (bcc). Besides this transformation, there are two other fundamental mechanisms by which metals and alloys deform plastically by homogeneous way: dislocations slip in specific slip systems and twinning[7]. These deformation modes are directly related to the stacking fault energy (SFE) of the austenitic structure. Therefore, SFE has traditionally been used as an indicator of the trend in twinning for TWIP steels and martensitic transformation for TRIP steels[14].

Chemical composition and temperature are considered the major factors in controlling the stacking fault energy and hence determine the main deformation mechanisms, as shown in Figure 2.3. If the SFE is very low ($\leq$ 20 mJ/m$^2$) a strain-induced martensitic transformation is favored[14]. Higher values of SFE, about 25 mJ/m$^2$, suppress martensitic transformation and promote mechanical twinning until 60 mJ/m$^2$. However, the twinning intensity varies with the SFE. Therefore, for SFE values relatively low (25 mJ/m$^2$) the density of twins is high and this mechanism results in an almost homogeneous deformation. At higher SFE values, the partial decomposition of dislocations into partials is hindered and thus the major deformation mechanism is the slipping of dislocations. Thus, alloys with intermediate SFE tend to show mechanical twinning in place of phase transformation or dislocation glide[2, 9, 15, 16].

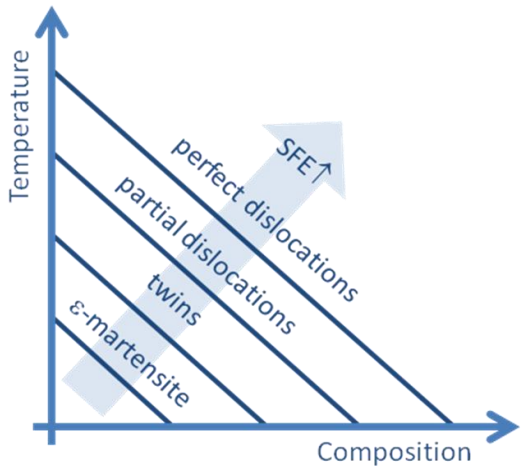


Figure 2.3. Schematic representation of the stacking fault energy influence, which is controlled by the temperature and composition, on the deformation mechanisms in austenite[2,9].

The twinning deformation mechanism associated with the dislocation motion is very beneficial as it provides a high work hardening rate. This is due to the twin boundaries act as barriers which inhibit dislocation movement[2].

*2.1.3. Alloy elements in steels with high Mn content*

Manganese is the main alloying element in TWIP steels. It has the function of controlling the SFE and preserving the austenitic structure according to the ternary Fe-Al-Mn system[17]. Figure 2.4 shows experimental data concerning the effect of Mn addition on the SFE in Fe-Mn system[18, 19]. These data show that with increasing Mn content, SFE decreases to a minimum and then increases again. By this way, the increase on the Mn content will change the deformation mode from TRIP to TWIP due to the increase in SFE from low values (<20 mJ/m$^2$) to moderate values (> 20 mJ/m$^2$)[2].

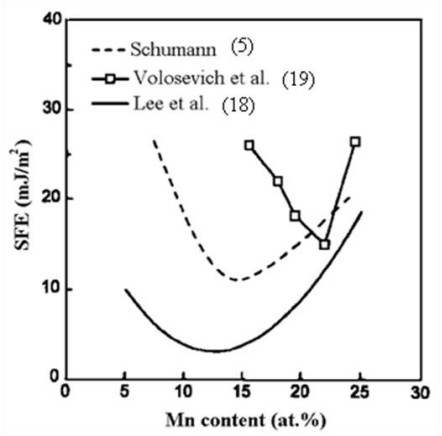


Figure 2.4. Variation of stacking fault energy as a function of Mn content in Fe-Mn alloys[5, 17-20].

The addition of aluminum in high-Mn steels has several functions. The aluminum increases the stacking fault energy significantly and then stabilizes austenite against the $\gamma \rightarrow \varepsilon \rightarrow \alpha'$ transformation which occurs in Fe-(15-25%)Mn during deformation[20, 21]. Furthermore, it increases the mechanical strength of austenite by solid solution and increases corrosion resistance[2, 22].

Silicon, in contrast to aluminum, decreases the stability of austenite and promotes its transformation into ε martensite during deformation or cooling[23]. In steels with 27%Mn additions of 2%Si decreases the SFE of austenite, resulting in an increase in stacking faults, which favors the ε martensite formation[24]. Furthermore, the addition of silicon hardens of austenite through solid solution[22].

*2.1.4. Phase transformations in high-Mn steels exhibiting effects TRIP and TWIP*

The addition of Al and Si to Fe-Mn alloys affects the stacking fault energy, as well as the phases stability, and gives rise to distinct properties such as high work hardening associated with deformation twinning and deformation-induced martensitic transformation[8, 25-28].

In TRIP/TWIP steels with 18.8%Mn, for true strains from 0.06 to 0.14, austenite transforms into ε martensite and, subsequently, into α' martensite. Atomic movement by shear stress creates a new stacking fault on {111} plane, which give rise to thin plates of ε martensite[29].

In the early stages of ε martensite formation, stacking faults overlap in the intersections between active slip planes of different families, or in grain boundaries and annealing twins. Only small deformation energy can induce the formation of ε martensite and for this reason its volume fraction suddenly increases in the initial stage of plastic deformation. Subsequently it transforms into α' martensite[29, 30].

The α' martensite is usually formed at the intersection of two ε martensite crystals plates. Due to the great distortion at the intersection, a crystal nucleus of α' martensite grows easily from a ε martensite crystal. The strain energy accumulation, the growth of ε martensite and the increasing in dislocation density provide conditions for α' martensite formation[29].

In TRIP/TWIP steels with 18.8%Mn, deformed between 0.14 and 0.35 true strains in tensile test, the amount of phases remains unchanged. When true stress increases there is separation between twinned and not twinned regions within the γ grains. The twinning occurs as an energetically favorable rearrangement of partial dislocations. The grains rotate to crystallographic orientations which are more advantageous in relation to the plastic deformation direction. The dislocations pinning due to presence of twin boundaries cause stress concentration. When it is difficult for twinning to occur dislocation glide starts again. Twinning and dislocation glide occur simultaneously,

which provides the increasing in steel strength[29, 31]. As illustrated in the literature[32], among all deformation modes for austenitic steels, twinning has the most positive effect on hardening. It is believed that deformation by twinning increases the hardening rate due to its action as obstacles to dislocation glide.

For the same TRIP/TWIP steels with 18.8%Mn stress concentration becomes larger with increasing deformation (0.35 and 0.45 true strains) due to the partial transformation of austenite into α' martensite, characterizing also the TRIP effect presence[29]. The α' martensite is formed inside ε martensite plates and it often change its morphology (Fig. 2.5 (a)). The α' martensite usually starts forming in the boundaries between austenite and ε martensite extending into the ε martensite plates until they reach the next γ/ε boundarie. The more narrow the ε plates are, smaller are the α' martensite ones. There are also irregular and larger α' martensite morphologies (Fig. 2.5 (b)), beyond the plates. The α' martensite morphology depends mainly on the number of variants and the transformation time. Figure 2.5 (c) shows schematically ε and α' martensite morphologies at different transformation stages. The first stage corresponds to the α'martensite formation from the boundary between γ and ε phases, while the second stage is related to the growth of α' martensite plates. Finally, in the third stage the formed α' martensite plates reaches the subsequent γ/ε boundaries[33].

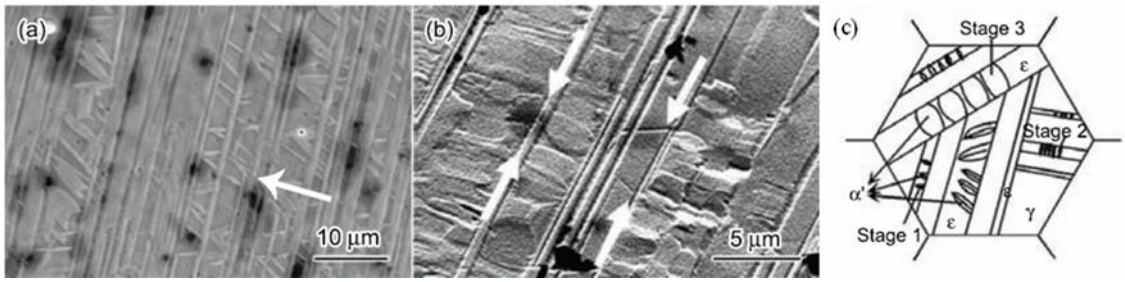


Figure 2.5. Morphologies of martensites in a steel with 18%Mn: (a) the arrow denotes the α' martensite plates between ε martensite laths; (b) the arrows indicate α' martensite irregular shapes; (c) martensites schematic drawing at different stages of growth[35].

It was also reported for a Fe-24Mn alloy submitted to a tensile test at 20°C that martensitic transformation tends to act as a deformation mechanism besides twinning when the deformation increases above 20%. Regions containing ε martensite are formed from austenitic grains with different crystal orientations[34].

## 2.2. Objectives

Studies for development of steels with TRIP/TWIP effect have focused on optimizing properties such as strength, ductility and density. Thermomechanical processing to produce a microstructure suitable for obtaining these properties in the final product are constantly targets of these researches. However, few studies have focused on the study of the effect of cold deformation and annealing on the microstructure, crystallographic texture and deformation mechanisms which will determine the mechanical properties of these steels. In this scope, this work has as main objectives:

- To evaluate the influence of cold deformation and annealing on crystallographic texture and mechanical properties of a 17% Mn steel and 0.06%C.
- To investigate the deformation mechanisms that occur in samples submitted to tensile test or cold rolling under different strains by means of microstructure and crystallographic texture analysis.
- To investigate the reversion mechanisms of ε and α' martensites in austenite and how they can influence the microstructure after annealing.
- To correlate the effect of texture and deformation mechanisms, generated from the thermomechanical processing, on the microstructure and mechanical properties of this 17%Mn steel.

## 2.3. Thesis structure and organization

This thesis presents 8 chapters. Chapter 1 is an introduction to the scope of this investigation.

Chapter 2 shows a brief literature review with some important works using similar steels.

Chapter 3 presents the effect of austenitic grain size and cooling rate on the formation of ε and α' martensite. The stacking fault energy for this steel was also calculated in this chapter.

Chapter 4 presents a study of microstructural evolution and its influence on the mechanical behavior for the 17%Mn steel after warm rolling at 700ºC, cold rolling, with reductions from 4 to 81%, and annealing at 700 and 800°C.

Chapter 5 shows a kinetic study of the evolution of the microstructure and its influence on the mechanical behavior when the material was hot rolled at 1070°C, cold rolled with 44% reduction, and annealed at 700°C with different times.

Chapter 6 shows an investigation on the relative amount of the phases and microstructural parameters which give an idea about the austenite reversion mechanisms involved during the annealing at different temperatures for the steel initially submitted to 60 and 90% cold reduction. In this study it was used X-ray diffraction and the software Materials Analysis Using Diffraction (MAUD)[15] based on Rietveld method[16] besides hardness Vickers and transmission electron microscopy (TEM).

Chapter 7 presents the evolution of the microstructure and transformation texture for this new TRIP/TWIP steel via EBSD (Electron backscatter diffraction) and TEM techniques in the material subjected to cold rolling with 60 and 90% reduction followed by annealing at different temperatures.

Chapter 8 brings the final considerations of the thesis, including the main conclusions, suggestions for future works, and original contributions.

**References**


1. BRACKE, L. Deformation Behaviour of Austenitic Fe-Mn Alloys by Twinning and Martensitic Transformation. Belgium: Ghent University, 2007. Ph.D. Thesis.
2. HAMADA, A. S. Manufacturing, Mechanical Properties and Corrosion Behaviour of High-Mn TWIP Steels. Finland: Faculty of Technology, University of Oulu, 2007. 56p. Academic Dissertation.
3. REMY, L., PINEAU, A. Twinning and strain-induced F.C.C. → H.C.P. transformation in the Fe-Mn-Cr-C system, *Materials Science and Engineering*, v. 28, n. 1, p. 99-107, 1977.
4. ALLAIN, S. Caractérisation et modélisation thermomécaniques multi-échelles des mécanismes de déformation et d'écrouissage d'aciers austénitiques à haute teneur en manganèse – Application à l'effet TWIP. France: INPL, Ecole des Mines de Nancy, 2002. Ph.D. Thesis.
5. SCHUMANN, H. Martensitic Transformations in Austenitic Manganese Carbon Steels, *Neue Hütte*, v. 17, n. 10, p. 605-609, October, 1972.
6. SCOTT, C., GUELTON, N., ALLAIN, S., FARAL, M. Materials Science and Technology Conference and Exhibition, 05, Pittsburgh, USA. Proceedings of the MS&T'05 Conference, p. 26-28, 2005.
7. OH, B.W., CHO, S.J., KIM, Y.G., KIM, W.S., HONG, S.H. Effect of aluminium on deformation mode and mechanical properties of austenitic Fe-Mn-Cr-Al-C alloys, *Materials Science and Engineering A*, v.197, p. 147-156, 1995.
8. FROMMEYER, G., BRÜX, U., NEUMANN, P. Supra-ductile and high-strength manganese-TRIP/TWIP steels for high energy absorption purposes, *ISIJ International*, v. 43, n. 3, p. 438-446, 2003.
9. VERCAMMEN, S. Processing and Tensile Behaviour of TWIP Steels Microstructural and Texture Analysis. Belgium: Katholieke Universiteit Leuven, 2004. PhD thesis.
10. HICKEL, T., GRABOWSKI, B., KÖRMANN, F., NEUGEBAUER, J., Advancing density functional theory to finite temperatures: methods and

applications in steel design, *Journal of Physics: Condensed Matter*, v. 424, n. 5, p. 1-17, 2012.

11. MESPLONT, C., DE COOMAN, B.C. Effect of austenite deformation on crystallographic texture during transformations in microalloyed bainitic steel, *Materials Science and Technology*, v. 19, n. 7, p. 875-886, 2003.
12. FRANKS, R., BINDER, W.O., THOMPSON, J. Austenitic chromium-manganese-nickel steels containing nitrogen. *Transactions of the ASM*, v. 47, p.231-266, 1955.
13. NIJHAWAN, B.R., GUPTE, P.K., BHATGANAR, S.S., GUHA, B.K., DHANJAL, S.S. Substitute Nickel-free Austenitic Stainless Steel, *Journal of the Iron and Steel Institute*, p. 292-304, March, 1967.
14. KRÜGER, L., MEYER, L. W., BRÜX, U., FROMMEYER, G., GRÄSSEL, O. Stress-deformation behaviour of high manganese (Al, Si) TRIP and TWIP steels, *J. Phys. IV France*, v. 110, p. 189-194, 2003.
15. HAN, Y. S., HONG, S. H. The effect of Al on mechanical properties and microstructures of Fe-32Mn-12Cr-xAl-0.4C cryogenic alloys, *Materials Science and Engineering A*, v. 222, n. 1, p. 76-83, 1997.
16. ROHATGI, A., VECCHIO, K. S., GRAY, G. T. The influence of stacking fault energy on the mechanical behavior of Cu and Cu-Al alloys: deformation twinning, work hardening, and dynamic recovery, *Metallurgical and Materials Transactions A*, v. 32, n. 1, p. 135-145, 2001.
17. SATO, K., TANAKA, K., INOUE, Y. Determination of the a/g Equilibrium in the Iron Rich Portion of the Fe-Mn-Al System, *ISIJ Int*, v. 29, p. 788-792, 1989.
18. LEE, Y. K., CHOI, C. S. Driving force for γ→ε martensitic transformation and stacking fault energy of γ in Fe-Mn binary system, Metallurgical and Materials Transactions A, v. 31, n. 2, p. 355-360, 2000.
19. VOLOSEVICH, P. Y., GRINDNEV, V. N., PETROV, Y. N. Manganese Influence on Stacking-Fault Energy in Iron-Manganese Alloys, Physics of Metals and Metallography, v. 42, p. 126 -130, 1976.
20. GRÄSSEL, O., FROMMEYER, G., DERDER, C., HOFMANN, H. Phase Transformation and Mechanical Properties of Fe-Mn-Si-Al TRIP-Steels, *J. Phys. IV France*, v. 110, p. 383-388, 1997.

21. WAN, J., CHEN, S., HSU, T. Y. The stability of transition phase in Fe-Mn-Si based alloys, *Calphad*, v. 25, n. 3, p. 355-362, 2001.
22. CHARLES, J., BERGHÉZAN, A., LUTTS, A. Structure and Mechanical Properties of High-Alloy Manganese-Aluminum Steels, *Journal Physique*, v. 43, n. 12, p. C4-435, 1982.
23. SCHRAMM, R. E., REED, R. P. Stacking fault energies of seven commercial austenitic stainless steels, *Metallurgical and Materials Transactions A*, v. 6, n. 7, p. 1345-1351, 1975.
24. TAKAKI, S., FURUYA, T. Tokunaga, Y. Effect of Si and Al Additions on the Low Temperature Toughness and Fracture Mode of Fe-27Mn Alloys, *ISIJ Int*, v. 30, p. 632-638, 1990.
25. HIROSHI, F., TETSUYA, K. In-situ Observation of Strain-Induced $\gamma \rightarrow \varepsilon \rightarrow \alpha'$ Martensitic Transformations in Fe-Cr-Ni Alloys. *Materials Transactions*, v. 33, n. 3, p. 243–251, 1992.
26. HYOUNG, C. C., TAE, K. H., HONG, C. S., YONG, W. C. The formation kinetics of deformation twin and deformation induced ε-martensite in an austenitic Fe-C-Mn steel, *Scripta Materialia*, v. 40, p. 1171–1177, 1999.
27. LUDWIGSON, D.C. Modified stress-strain relation for FCC metals and alloys. *Metallurgical Transactions*, v. 2, n.10, p. 2825–2828, 1971.
28. SATO, K., ICHINOSE, M., HIROTSU, Y., INOUE, Y. Effects of deformation induced phase transformation and twinning on the mechanical properties of austenitic Fe-Mn-Al alloys, *ISIJ International*, v. 29, p. 868-876, 1989.
29. DING, H., DING, H., SONG, D., TANG, Z., YANG, P. Strain hardening behavior of a TRIP/TWIP steel with 18.8% Mn, *Materials Science and Engineering: A*, v. 528, n. 3, p. 868-873, January, 2011.
30. XU, Z. Y. Martensitic transformation fcc(γ)→hcp(ε), *Science in China Series E: Technological Sciences*, v.40, n. 6, p. 561-566, December, 1997.
31. KARAMAN, I., SEHITOGLU, H., GALL, K., CHUMLYAKOV, Y. I., MAIER, H. J. Deformation of single crystal Hadfield steel by twinning and slip, *Acta Materialia*, v. 48, n. 6, p. 1345–1359, 2000.

32. BOUAZIZ, O., ALLAIN, S., SCOTT, C. Effect of grain and twin boundaries on the hardening mechanisms of twinning-induced plasticity steels, *Scripta Materialia*, v. 58, n. 6, p. 484-487, March, 2008.
33. LU, F., YANG, P., MENG, L., CUI, F., DING, H. Influences of Thermal Martensites and Grain Orientations on Strain-induced Martensites in High Manganese TRIP/TWIP Steels, *Journal of Materials Science & Technology*, v. 27, n. 3, p. 257-265, 2011.
34. LIANG, X. Structure and Mechanical Properties of Fe-Mn Alloys. Beijing: University of Science and Technology Beijing, 2008. 254p. (Thesis, Degree of Master of Applied Science).

## CHAPTER 3: Effect of cooling rate on (ε, α′) martensite formation in Twinning/Transformation-Induced Plasticity Fe–17Mn–0.06C steel


### Abstract

Cooling rate, density of stacking faults, austenite grain size, and temperature strongly influence the $\gamma_{fcc} \rightarrow \varepsilon_{hcp} \rightarrow \alpha'_{bcc}$ martensite transformation in austenitic alloys. During cooling, austenitic Fe–Mn steels within a restricted chemical composition can partially transform to ε and α′ martensites. Martensite formation will influence the mechanical behavior of the alloy. The microstructure evolution under three cooling rates of a hot rolled austenitic steel, Fe–17.0Mn–0.06C (wt%), was analyzed by optical microscopy and scanning electron microscopy/electron backscatter diffraction. The volume fraction of martensite and austenite were measured by X-ray diffraction line profile analysis by directly comparing the as-cast alloy, alloy subjected to different cooling conditions, and this processed with hot rolling.



**Keywords:** Cooling rate; martensite formation; grain boundaries; stacking fault energy.


### 3.1. Introduction

Fe–C–Mn–Al–Si alloys have attracted significant interest in physical metallurgy and materials science because their mechanical properties such as high ductility and strength are important for industries[1-5]. Steels with high Mn content (15–30%) and alloy elements, such as Si and Al, have high strength and exceptional plasticity owing to either twinning-induced plasticity (TWIP) or the transformation-induced plasticity (TRIP) that results from multiple martensitic transformations such as $\gamma_{fcc}$ (austenite) $\rightarrow \varepsilon_{hcp}$ (hcp-martensite) $\rightarrow \alpha'_{bcc}$ (bcc-martensite)[5-8].

As cited in the Chapter 2, for twinning to occur, it is usually necessary for the steel stacking fault energy (SFE) to be in the range of 18–35 mJ/m$^2$. If the SFE is <18 mJ/m$^2$, twinning is replaced by martensitic transformation. However, if it is >35 mJ/m$^2$, then

the dislocation slipping will be the only mechanism that contributes to the plastic deformation of steel[9,10].

The stability of austenite in these steels is of great importance because of the phase transformation that accompanies the plastic deformation which occurs either through twinning or martensitic transformation. The latter depends on steel chemical composition, temperature, austenite grain size, and amount of applied stress. The formation of martensite can be induced thermally or by deformation[10-14]. During cooling, the austenitic Fe–Mn steel, within a restricted range of chemical composition, partially transforms into $\varepsilon_{hcp}$ and $\alpha'_{bcc}$ martensite, while retaining some the untransformed austenite[12-15].

Stacking faults and twinning are important for the formation of martensite in Fe–Mn–Si–Al steels because they act as nucleation sites for martensite formation[16-19]. The phase transformation $\gamma \rightarrow \varepsilon_{hcp}$ occurs through the formation of alternate layers of stacking faults in the (111) planes of austenite. $\alpha'$ martensite is formed either directly from austenite or at the intersections of different variants of $\varepsilon$ martensite[8,9,20].

In addition to the cooling rate and crystallographic defects, the prior austenite grain size (PAGS) is another parameter that controls the stability of the austenite because the formation of martensite can be prevented by the presence of a large numbers of barriers in the microstructure, such as twin or grain boundaries and deformation defects[11,12,14].

The industrial production of TRIP and TWIP steels always involves thermo-mechanical processing such as hot rolling, cold rolling at room temperature, and annealing. In all these stages, the steel goes through thermal cycles involving both heating and cooling. However, research has tended to focus on the martensitic transformation from deformed structures[2-4,9,10,15]. Few studies have considered the formation of martensite in TRIP and TWIP steels in the absence of strain. Only those transformations resulting from cooling, or the reversal of martensite to austenite in alloys that exhibit the shape memory effect, have been considered[11-13,19,20].

This study evaluates the effect of austenitic grain size and cooling rate on the formation of ε and α' martensite in a steel with 17%Mn and 0.06%C. TWIP steels with similar Mn content but much higher carbon content (0.2–0.6%C) have been analyzed in previous reports[7,10,12,15,21]. However, the chemical composition of the steel discussed in this study has not been reported in the literature yet. This chemical composition provides the steel a low SFE, thereby greatly facilitating the formation of martensite[8]. Therefore, it is need to improve the knowledge of the physical characteristics of these alloys in order to better understand the stability of austenite during their industrial processing.

### 3.2. Experimental procedure

In this study, TRIP/TWIP steel was used and its composition is listed in Table III.1. The steel was melted in Keel ASTM A370 block by air in an induction furnace (Power Trak 250-10 R Inductotherm®). The steel was melted and cast at 1558°C and 1510°C, respectively. Plates were removed from the Keel blocks, austenitized at 1100°C for 2 h, and then cooled in water to homogenize their microstructure and chemical composition. After homogenization, samples were cut for hot rolling, which was performed at 1070°C with four passes of equal reduction leading to a total thickness reduction of 50%. The resulting thickness was 12 mm[3].

Table III.1. Chemical composition of TRIP/TWIP* steel.

| **Element** | **Mn** | **Al** | **Si** | **Ni** | **C** |
|---|---|---|---|---|---|
| **Mass %** | 17.0 | 3.0 | 2.0 | 1.0 | 0.06 |

* TRIP, transformation-induced plasticity; TWIP, twinning-induced plasticity

From the hot rolled sheet, a 100 × 20 × 12 mm sample was divided into three equal parts, which were then heated at 1000°C for 3600 s. After soaking, three different cooling methods were applied: natural air (AS), immersion in water (WS), and inside the furnace after its shutdown (FS). The samples were also examined in the as-cast and hot rolled conditions. After the heat treatment, each sample was divided into two parts. One part was hot-mounted for metallographic examination while the other was used for X-ray diffraction (XRD) analysis. All the samples were carefully and conventionally

ground and polished with 0.25 μm diamond paste. Their microstructure was analyzed via optical and scanning electron microscopy (SEM), etched initially with 4% Nital. The grain size was measured using the software Image Pro Plus®. Electron backscatter diffraction (EBSD) analysis was also carried out to study the crystallography of the phase transformation, for which the samples were additionally polished with colloidal silica (size 0.02 μm) before the final examination.

The retained austenite and the ε and α′ martensite volume fractions were quantified by XRD with Cu Kα radiation via the direct comparison method[22]. This method uses the integration of the most intensive peaks of (i) austenite, characterized by the (111), (200), (220), and (311) planes; (ii) α′ martensite, characterized by the (110), (200), (211), and (220) planes; and (iii) ε martensite, characterized by the (100), (002), (101), and (102) planes. The Origin™ software was used for integrating these peaks with a peak-fitting tool.

### 3.3. Results and discussion

#### *3.3.1. Stacking fault energy*

The addition of alloying elements such as Al and Ni increases the SFE and tends to inhibit the martensitic transformation (γ→ε→α′), whereas the addition of Si decreases the SFE, thereby favoring the formation of martensite during cooling and deformation.

The SFE (Γ) in TRIP/TWIP steel can be estimated using the model proposed by Dumay *et al.* [18], according to Equation 3.1[23]:

$$\Gamma = 2d\Delta G^{\gamma\to\varepsilon} + 2\sigma^{\gamma\to\varepsilon} \tag{3.1}$$

Where "d" is the molar surface density of atoms in the plane {111} and it is equal to $2.94*10^{-5}$ mol.m$^{-2}$, $\Delta G^{\gamma\to\varepsilon}$ is the molar the Gibbs free energy of γ→ε transformation, and

$\sigma^{\gamma \to \varepsilon}$ is the surface energy associated with the interface between the γ and ε phases and corresponds to 8 $mJm^{-2}$.

The free energy of martensite formation can be represented by Equation 3.2:

$$\Delta G^{\gamma \to \varepsilon} = \Delta G^{\gamma \to \varepsilon}_{FeMnX} + x_c \Delta G^{\gamma \to \varepsilon}_{FeMnX/C} + \Delta G^{\gamma \to \varepsilon}_{mg} \qquad (3.2)$$

$\Delta G^{\gamma \to \varepsilon}_{FeMnX}$ is the contribution of the substitutional chemical elements in fcc lattice phase. The terms in excess of Fe, Mn, Si, Al and Ni are considered in this calculation, but other elements are neglected due to their low level in this alloy. This contribution is shown in Equation 3.3:

$$\Delta G^{\gamma \to \varepsilon}_{FeMnX} = \sum_i x_i \Delta G^{\gamma \to \varepsilon}_i + x_{Fe} x_{Mn}[C + D(x_{Fe} - x_{Mn})] + x_{Fe} x_{Si}[E + F(x_{Fe} - x_{Si})] \qquad (3.3)$$

Where: $x_i$ is the mole fraction of each element, T is temperature and C, D, E and F are adjusted values.

The effect of the carbon content in combination with the manganese content is given by Equation 3.4, where a, b and c are adjusted values.

$$\Delta G^{\gamma \to \varepsilon}_{FeMnX/C} = \frac{a}{x_c}(1 - e^{-bx_c}) + cx_{Mn} \qquad (3.4)$$

$\Delta G^{\gamma \to \varepsilon}_{mg}$ is a term due to Néel magnetic transition, which corresponds to the phase transformation of the paramagnetic phase to the antiferromagnetic γ and ε.

$$\Delta G^{\gamma \to \varepsilon}_{mg} = G^{\varepsilon}_m + G^{\gamma}_m \qquad (3.5)$$

Where:

$$G_m^{\varphi} = RT \ln\left(1+\frac{\beta^{\varphi}}{\mu_B}\right) * f\left(\frac{T}{T_N^{\varphi}}\right)$$ , φ are the phases γ e ε (3.6)

Since the magnetic moment, $\beta^{\varphi}$, (Eq. 3.8), $T_N^{\varphi}$ the Néel temperature, $\mu_B$, the Bohr magneton and *f* is a function given by Equation 3.7:

$$f^{\varphi}(\tau^{\varphi}) = \frac{-1}{2{,}34}\left[\frac{\tau^{-5}}{10}+\frac{\tau^{-15}}{315}+\frac{\tau^{-25}}{1500}\right], \tau = \left(\frac{T}{T_N^{\varphi}}\right) > 1 \quad (3.7)$$

$$\beta^{\gamma} = \beta^{\gamma}_{Fe} x_{Fe} + \beta^{\gamma}_{Mn} x_{Mn} - \beta^{\gamma}_{FeMn} x_{Fe} x_{Mn} - \beta^{\gamma}_{C} x_{C} \quad (3.8a)$$

$$\beta^{\varepsilon} = \beta^{\varepsilon}_{Mn} x_{Mn} - \beta^{\varepsilon}_{C} x_{C} \quad (3.8b)$$

Where $\beta_i^{\varphi}$ is the contribution of the element *i* in phase φ and $\beta_{ij}^{\varphi}$ is the term in excess. The Néel temperature for the different phases is given by Equation 3.9 a,b.

$$T_N^{\gamma} = 250\ln(x_{Mn}) - 4750 x_c x_{Mn} - 222 x_{Cu} - 2{,}6 x_{Cr} - 6{,}2 x_{Al} - 13 x_{Si} + 720 \text{ (K)} \quad (3.9a)$$

$$T_N^{\varepsilon} = 580 x_{Mn} \text{ (K)} \quad (3.9b)$$

The values required for the calculation of the SFE are shown in Table III.2. Using an electronic spreadsheet, the calculated value of the SFE for steel in this work is 14.5 mJ/m².

Table III.2. Summary of the parameters used in the model of Dumay *et al*[18].

| | |
|---|---|
| $\Delta G_{Fe}^{\gamma\to\varepsilon}$ | -2243.38 + 4.309T (Jmol$^{-1}$) |
| $\Delta G_{Mn}^{\gamma\to\varepsilon}$ | -1000 + 1.123T (Jmol$^{-1}$) |
| $\Delta G_{FeMn}^{\gamma\to\varepsilon}$ | C = 2873 Jmol$^{-1}$, D =-717 Jmol$^{-1}$ |
| $\Delta G_{FeMnX/C}^{\gamma\to\varepsilon}$ | a = 1246 Jmol$^{-1}$, b = 24.29 Jmol$^{-1}$, c = -17175 Jmol$^{-1}$ |
| $\frac{\beta^{\gamma}}{\mu_B}$ | $0{,}7x_{Fe} + 0.62x_{Mn} - 0.64x_{Fe}\,x_{Mn} - 4x_C$ |
| $\frac{\beta^{\varepsilon}}{\mu_B}$ | $0.62x_{Mn} - 4x_C$ |
| $\Delta G_{Al}^{\gamma\to\varepsilon}$ | 2800 + 5T (Jmol$^{-1}$) |
| $\Delta G_{Si}^{\gamma\to\varepsilon}$ | -560 – 8T (Jmol$^{-1}$) |
| $\Delta G_{FeSi}^{\gamma\to\varepsilon}$ | E= 2850 J mol$^{-1}$, F = 3520 Jmol$^{-1}$ |
| $\Delta G_{Ni}^{\gamma\to\varepsilon}$ | 1423 Jmol$^{-1}$ |

*3.3.2. Analysis by X-ray diffraction*

Figure 3.1 shows the XRD patterns of samples subjected to the three different cooling rates and those of the as-cast and hot rolled conditions. The coexistence of austenitic and martensitic phases in the samples can be confirmed by their respective peaks in the diffraction patterns, the EBSD images shown in Figure 3.2, and the results in Table III.3.

The ε-martensite-starting temperature ($M\varepsilon_s$) gradually decreases with increasing Mn content and alloy elements. Equation 3.10, derived from the multiple regression analysis by Yang *et al.*[24], provides $M\varepsilon_s$ value for the steel used in present work as 174°C. Coincidentally, $M\varepsilon_s$ reported by Tsuzaki *et al.*[25] for 16Mn–0.006C steel was also 174°C. ε martensite transforms from austenite before α′ martensite does. However, no relation was found in the literature for calculating $M\alpha'_s$ after ε martensite formation.

$$M\varepsilon_s\,(K) = 576 - 489(\%C) - 9.1(\%Mn) - 17.6(\%Ni) - 9.2(\%Cr) + 21.3(\%Al) + \\ + 4.1(\%Si) - 19.4(\%Mo) - 1(\%Co) - 41.3(\%Cu) - 50(\%Nb) - 86(\%Ti) - 4(\%V) - \\ - 13(\%W) \qquad (3.10)$$

The ε and α′ martensite transformations occur in the steel used in the present work because of different cooling rates, mainly in an athermal mode, assisted by some strain resulting from solidification or thermal contraction. However, it was not possible to separate the amount of each transformation.

In the as-cast sample, despite the slow cooling during the thermal cycle, residual stress was generated because of the contraction during the solidification of the alloy. These stresses can result into a larger volume fraction of ε and α′ martensite.

The same reasoning is applied to the WS sample. In this case, the stress was owing to thermal contraction[11]. For the FS sample, the steel is subjected to a high temperature for a longer period of time, which allows stress relief, resulting in a lower volume fraction of α′ martensite and greater stabilization of austenite. On the other hand, the AS sample led to a greater fraction of ε martensite (Table III.3).

According to Sahu *et al.*[15], the increase in the volume fraction of ε martensite would be justified because of its isothermally transformed amount. The phase-transformation kinetics would be favored by a longer cooling time in air in relation to the cooling carried out in water. Because the cooling in air and in the furnace are continuous and slow processes, they would favor the formation of isothermal martensite during cooling from temperatures higher than $M_{\varepsilon s}$. It is expected that α′ martensite formed during cooling in water will be athermal and dependent only on the temperature, whereas the amount of isothermal martensite depends on both the temperature and the time.

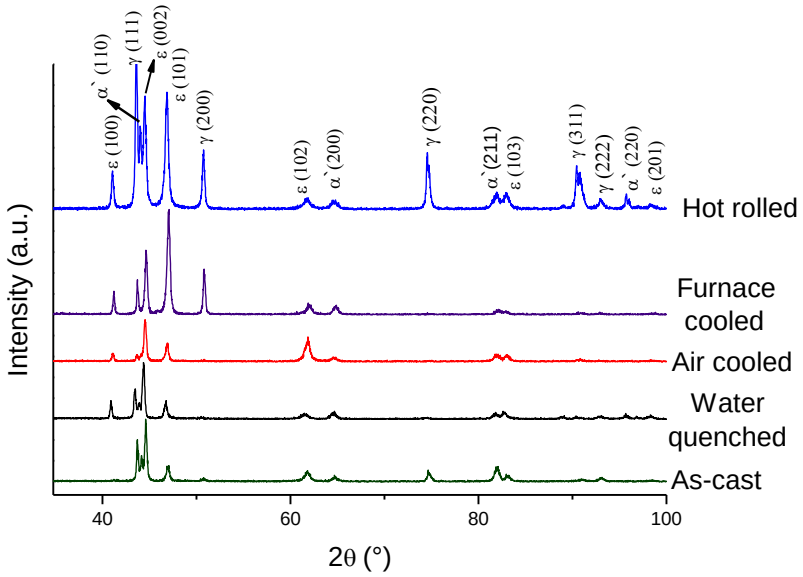


Figure 3.1. X-ray diffractograms after different processing conditions of the steel.

Table III.3. Phase volume fractions of samples measured by X-ray diffraction.

| Sample | Volume fraction (%) | | |
|---|---|---|---|
| | ε | α′ | γ |
| As-cast | 50.4 | 26.1 | 23.6 |
| Furnace cooled | 70.6 | 7.9 | 21.5 |
| Air cooled | 78.1 | 16.6 | 5.5 |
| Water quenched | 60.4 | 20.6 | 18.8 |
| Hot rolled | 41.7 | 15.8 | 42.5 |

### *3.3.3. Metallographic characterization*

#### *3.3.3.1. EBSD analysis*

Figure 3.2 shows the EBSD results of the sample annealed at 1000°C for 1 h and furnace cooled.

Verbeken *et al.*[20] demonstrated that although the specific nature of the austenite to ε martensite transformation is still in question, EBSD has a high potential for identifying ε martensite. In Figure 3.2 (a), the black arrows indicate α′ martensite, whereas the red

arrows show ε martensite; the blue background is austenite in different orientations. In the annealed specimen, the austenite grain boundaries are not delineated because of the high magnification used in the EBSD image. Figure 3.2 (b) shows a phase-contour delineation of the microstructure inside the austenitic grains, where different crystallographic variants of α′ and ε martensite coexist.

Figure 3.2 (c) shows a strong interaction between α′ and ε martensite. There is no α′ martensite that is not associated with ε martensite. This observation highlights the fact that α′ is being formed from ε and not directly from the austenite in the steel under study. The lenticular and bulk morphologies of α′ are well defined, as indicated in Figure 3.2 (a) by the black arrows. One difficulty indicated by Verbeken *et al.*[20] in evaluating austenite and ε martensite phases by EBSD results from the close proximity of each unit. As long as ε martensite is formed as extremely thin plates[9,26] resulting from twinning, some austenite is invariably left between the plates, leading to increased difficulty in obtaining Kikuchi indexing lines. Quantitatively, it can also lead to a lower image quality (IQ) index, as seen in Figure 3.2 (b), assessed by the system software.

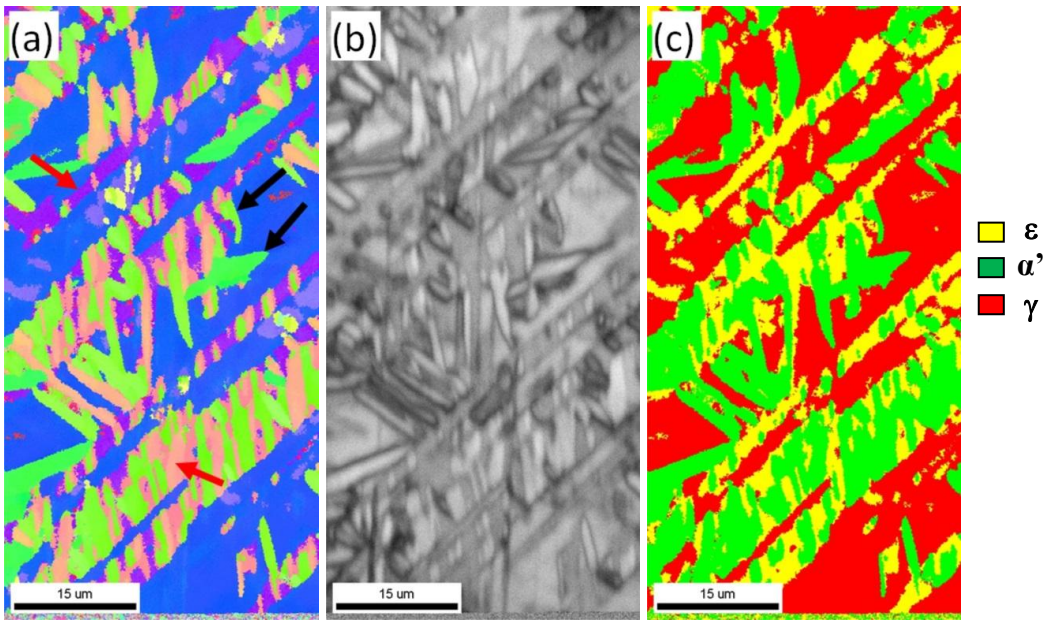


Figure 3.2. Electron backscatter diffraction evaluation. (a) IPF (inverse pole figure), (b) IQ (image quality) map, and (c) phase map for the sample annealed at 1000°C for 1 h and furnace cooled.

*3.3.3.2. Optical and SEM metallography*

*As-cast and heat-treated structures*

Figures 3.3 to 3.5 show the optical and scanning electron micrographs of the as-cast samples and cooled under the three different cooling conditions: water, air, and furnace. The prior austenitic grain size (PAGS) reached a wide range of 200–1000 μm, as seen in Figure 3.5.

Figures 3.4 (a) and (b) show that α′ martensite grew in different directions. This is due the continuous nucleation and growth. Although the growth rate can be fast, in order to reach the $M_{\varepsilon f}$ (ε martensite finish temperature), α′ martensite must nucleate in the ε martensite plates because they are formed during the cooling process.

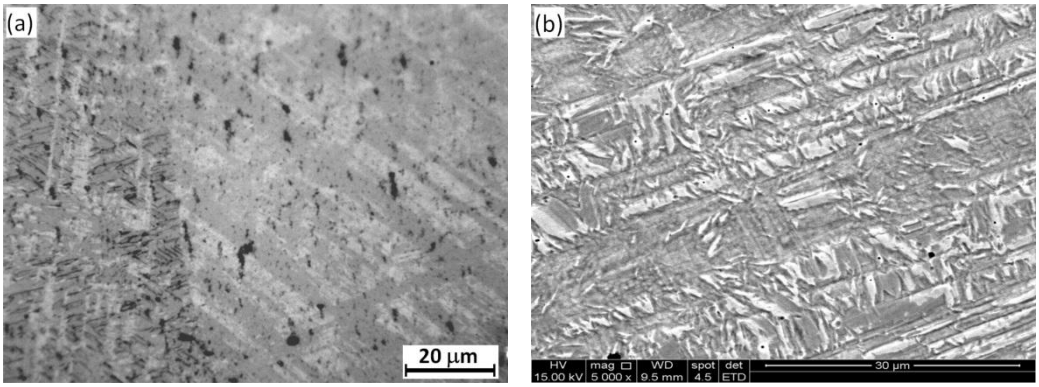


Figure 3.3. (a) Optical and (b) scanning electron micrographs of the as-cast sample. Samples were etched with 4% Nital.

Figures 3.4a and d show that ε martensite is formed within the austenitic grain, which then spreads until it reaches the opposite grain boundary where the orientation of the plates changes. The plates of ε martensite are formed by low-angle laths, thus forming packages (Fig. 3.5 (a–c)). It can also be observed that the formation of several packets of martensite occurs in the same grain. These packets tend to maintain an orientation of 60° (to each other), thereby forming equilateral triangles (Fig. 3.4 (c,d)). The size of the packet is limited by its neighbors (Fig. 3.4 (e,f)).

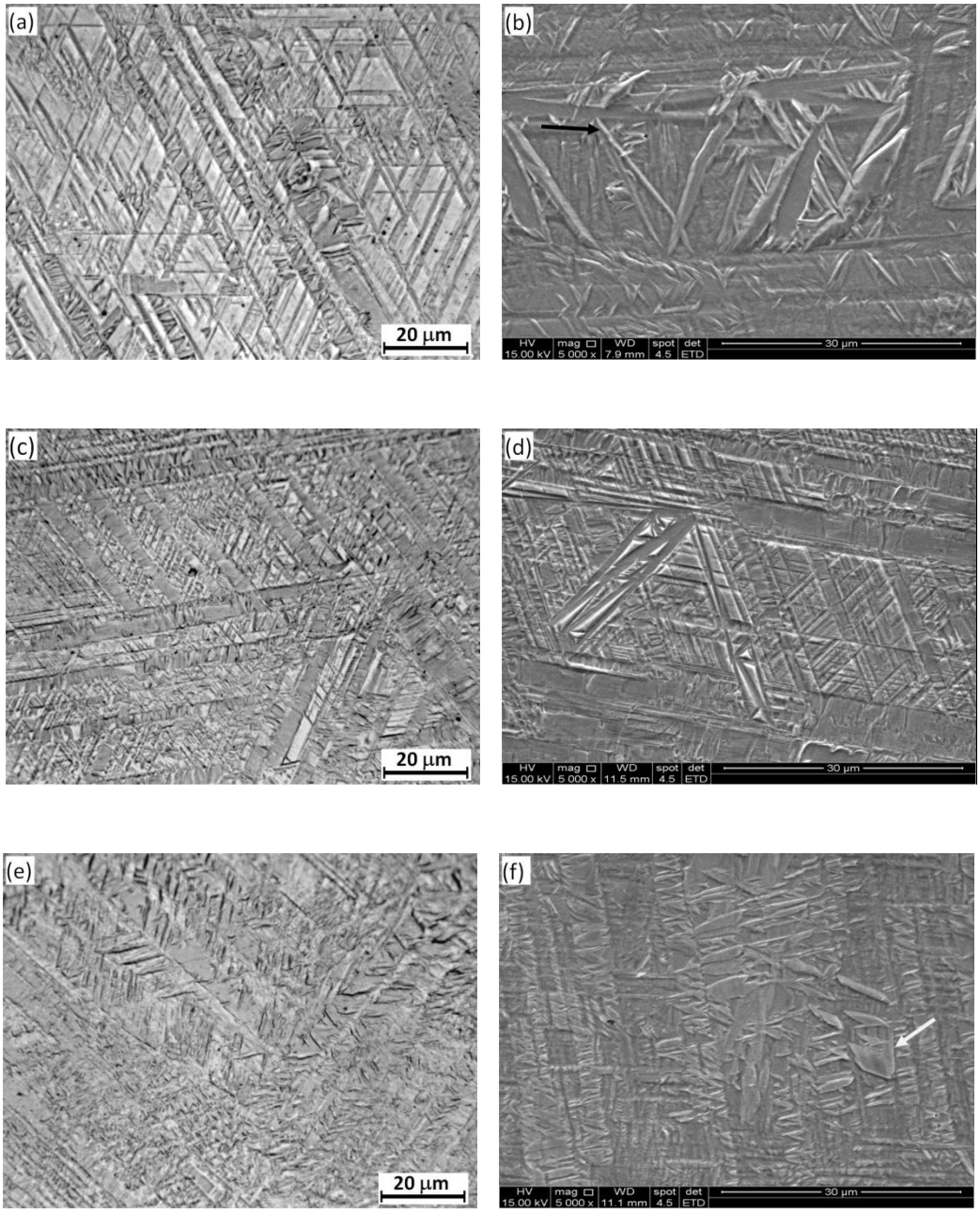


Figure 3.4. Optical (left) and scanning electron (right) micrographs of the samples (a, b) furnace cooled, (c, d) air cooled, and (e, f) water quenched. Samples were etched with 4% Nital.

Similarly, the growth of packages is hindered by other units. The original austenitic grain is divided in this way (Fig. 3.5 (a–c)). The examination of the microstructure at higher magnifications allows us to see that α′ martensite forms in the ε martensite plates, as shown by the SEM images in Figures 3.3 and 3.4. Furthermore, the size of α′ martensite plates varies significantly, which characterizes the process of nucleation and

growth during the cooling procedure. This phenomenon was also observed by Lu *et al.*[17] in 0.0045C–18Mn alloy. The authors[17] associateted two morphologies (lenticular and chunky) to the α′ martensite. In the current study, α' martensite of the same morphologies were observed, as indicated by arrows in Figures 3.4 (b) and (f), respectively. The latter occurs when the martensite assumes the shape of a grain. This morphology results from a coalescence process and is possible because of the duration of the cooling process.

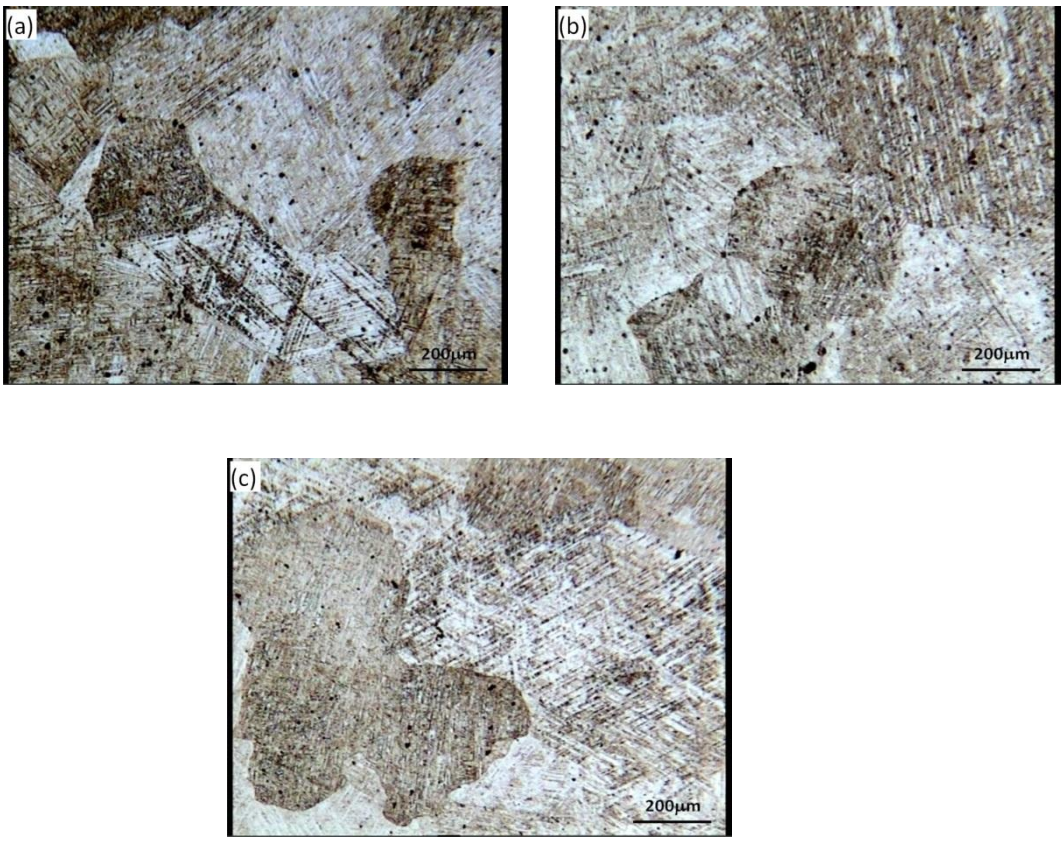


Figure 3.5. Optical micrographs of the samples (a) furnace cooled, (b) air cooled, and (c) water quenched. Samples were etched with 4% Nital.

On the other hand, there are regions where the formation of α′ martensite is minimal and where ε martensite predominates, as shown in Figure 3.4 (d). The background regions in the micrographs correspond to the untransformed austenite. Considering this result, we can say that α′ martensite will nucleate on the γ/ε interface and grow into ε martensite plates through intragranular nucleation, as observed in Figures 3.4a and b.

Sahu *et al.*[13] analyzed the thermal stability of the as-cast homogenized austenitic steel with a basic composition of Fe–26Mn–0.14C using the Rietveld XRD pattern-fitting technique. The decomposition of austenite was observed to be very sensitive to the cooling rate. A very high proportion (49–70%) of ε martensite was found in differently cooled specimens, as well as in the as-cast specimen. The same distribution of ε martensite volume fraction was found in the present study, as seen in Table III.3. According to Sahu *et al.*[13], the significant variation in the extent of the $\gamma \rightarrow \varepsilon \rightarrow \alpha'$ transformation resulted from the athermal and isothermal martensites formed during cooling and the initial grain size of the austenite. Their results are in good agreement with those of the present study, in which a volume fraction of ~80% martensite was attained, despite the significant difference in steel chemical composition.

*Hot rolled structure*

Figure 3.6 shows the optical and scanning electron micrographs of the hot rolled sample. In the present work, the steel was cooled in air after hot rolling. Large parallel laths crossing the micrograph correspond to ε martensite, whereas α′ martensite is formed within the laths at 60° tilt angles (Fig. 3.6 (b)). Similar to the heat-treated samples, size differences between the α′ martensite grains are noted. The grain-boundary structures created during hot rolling provide sites for martensite nucleation. The martensite also nucleates on the stacking faults[15]. The driving force for the $\gamma \rightarrow \varepsilon$ martensite transformation remarkably increases when the steel is heated at high temperature owing to the dissolution of dislocation tangles and networks, which arises because of prior hot rolling[8]. In addition to the clean microstructure, there is grain growth with an associated reduction in the number of grain boundaries, which hinders the development of martensite. However, the austenitic grain refinement imposed by hot rolling led to a lower volume fraction of ε and α′ martensite.

In the case of large austenitic grain sizes, branching of ε martensite plates will form, allowing the continuity of the $\gamma \rightarrow \varepsilon$ transformation[11]. For fine austenitic grains, i.e., after hot rolling, the martensite plate reaches the opposite grain boundary without ε

ramification. The process is interrupted, resulting in a greater volume fraction of austenite.

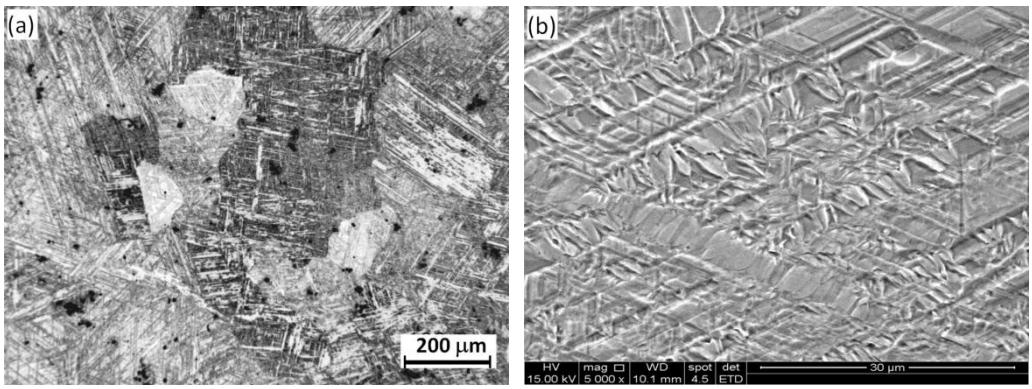


Figure 3.6. (a) Optical and (b) scanning electron micrographs of hot rolled sample. Sample was etched with 4% Nital.

Austenite grain size strongly influences the martensite formation start temperature ($M_s$). The increase in the volume fraction of α′ martensite with increase in the austenitic grain size is associated with a higher $M_s$, as well as with the greater area available for transformation of austenite into martensite. SFE decreases with increasing size of the austenite grain [27,28]. In steels with low SFE, a perfect dislocation in the fcc array can easily be divided into two partial dislocations, thus forming a stacking fault. Four or five layers of stacking faults are considered to be a potential nucleus for α′ martensite[16]. Thus, the higher the austenitic grain size, the greater the probability of finding nucleation sites for α′ martensite, formed by superimposing stacking faults, leading to a high $M_s$ temperature[15,29,30], and consequently, more time for transformation. All these conditions contributed to a large volume fraction of martensite formed in the steel under study, even in the absence of applied external stress and being submitted to slow cooling.

Dini *et al.*[12] studied the martensite formation in a high-Mn TWIP steel. Their quantitative microstructural characterization of steel by X-ray pattern-fitting by the Rietveld method indicated that the volume fraction of α′ martensite increased with increasing austenite grain size. This condition is in accordance with the present results, in which large austenite grain size led to a greater volume fraction of martensite.

Hamada *et al.*[14] worked on a high-Mn (Fe–26Mn–0.14C) austenitic steel hot compressed at 900, 1000, and 1100 °C with a strain rate of 5 $s^{-1}$ followed by air cooling (AC) or water quenching (WQ). The occurrence of dynamic recrystallization (DRX) produced a fine grain size (~10 μm), which was found to prevent α′ and ε martensite transformation upon cooling. In the current experiment, a coarse grain size (40 μm) allowed the transformation to proceed until reaching an ε martensite volume fraction of 17%. The grain boundaries, twins, and stacking faults enhance or suppress the phase transformation[29,30], depending on the size of the grains. For the hot rolled samples, the grain size was reduced to ~100 μm (Fig. 3.6 (a)), well above the critical size (10 μm[14]), thereby allowing the formation of up to 58% volume fraction of α′ and ε martensite (Table III.3).

In the industrial processing of this steel grade, the athermal formation of martensite has to be considered in order to obtain an adequate volume fraction of austenite at room temperature, thus making it possible to take advantage of the steel work-hardening and high-strength behavior. An alternative is to produce a very fine grain after cold rolling and then anneal it in order to stabilize the austenite.

### 3.4. Conclusions

- Both ε and α′ martensite formed in the present steel after being subjected to different cooling rates, mainly in an athermal mode, are assisted by some strain resulting from solidification or thermal contraction.
- In the as-cast sample, despite the slow cooling, it was still possible to produce residual stress owing to contraction during the solidification of the alloy. These stresses helped to increase the formation of a larger volume fraction of α′ martensite. The same reasoning applied to the sample cooled in water. In this case, there were stresses owing to thermal contraction and phase transformation. For the sample cooled in the furnace, the longer stay at high temperatures allowed to release the stress, resulting in a lower volume fraction of α′ martensite, a greater volume fraction of ε martensite, and stabilization of the austenite. The air cooled sample resulted in a larger volume fraction of ε

martensite, implying that the phase-transformation kinetics are favored by a longer cooling time in relation to the cooling carried out in water.

- When steel is hot rolled, its microstructure gets refined, resulting in a smaller grain size. This leads to a great volume fraction of the stabilized austenite and ε martensite, and therefore a lower α′ martensite volume fraction.
- Therefore, we can conclude that the α′ martensite results from ε transformation through the mechanism $\gamma \rightarrow \varepsilon \rightarrow \alpha'$.

**Acknowledgments**

The author thank the FAPEMIG, process number TEC PPM-00373/11, CNPq, process number 471128/2011-2, and CAPES (SSFD scholarship) for the financial support to carry out this research.

**References**

1. KIM, Y. G., KIM, T. W., HAN, J. K., CHANG, R. W. Development of new austenitic Fe-Mn-Al-C steels for automotive applications, *Key Engineering Materials*, v. 84-85, p. 461-472, 1993.
2. GRASSEL O., KRUGER, L., FROMMEYER, G., MEYER, L. W. High strength Fe-Mn-(Al,Si) TRIP/TWIP steels development-properties-application, *International Journal of Plastics*, v.16, p. 1391-1409, 2000.
3. FROMMEYER, G., BRÜX, U., NEUMANN, P. Supra-ductile and high-strength manganese-TRIP/TWIP steels for high energy absorption purposes, ISIJ Internatoinal, v. 43, p. 438–446, 2003.
4. SCOTT, C., ALLAIN, S., FARAL, M., GUELTON, N. The development of a new Fe-Mn-C austenitic steel for automotive applications, *La Revue de Métallurgie*, v. 6, p. 293-302, 2006.
5. DECOOMAN, B. C., KWON, O., CHIN, K-G. State-of-the-knowledge on TWIP steel. Materials Science and Technology, v. 28, p. 513-527, 2012.
6. SHUMANN, H. Die martensitischen umwandlungen in kohlenstoffarmen mangastählen, *Archiv für das Eisenhüttenwersen*, v.8, p. 647-654, 1967.

7. SATO, K., ICHINOSE, M., HIROTSU, Y., INOUE, Y. Effects of deformation induced phase transformation and twinning on the mechanical properties of austenitic Fe-Mn-AI alloys, *ISIJ Inteernational*, v. 29, p. 868-877,1989.
8. JANG, W.Y., GU, Q., VAN HUMBEEK, J., DELAY, I. Microscopic observation of γ-phase and ε and α'-martensite in Fe-Mn-Si-based shape memory alloys, *Materials Characterization*, v.34, p. 67-72, 1995.
9. BRACKE, L., KESTENS, L., PENNING, J. Influence of α'- martensite in an austenitic Fe-Mn-C-N alloy, *Scripta Materiallia*, v. 57, p. 385-388, 2007.
10. LU, Y., HUTCHINSON, B., MOLODOV, D. A., GOTTSTEIN, G. Effect of deformation and annealing on the formation and reversion of ε-martensite in an Fe–Mn–C alloy. *Acta Materiallia*, v. 58, p. 3079–3090, 2010.
11. TAKAKI, S., NAKATSU, H., TOKUNAGA, Y. Effects of austenite grain size on ε martensitic transformation in Fe-15mass%Mn alloy. *Materials Transactions, JIM*, v.34, p. 489-495, 1993.
12. DINI, G., NAJAFIZADEH, A., MONIR-VAGHEFI, S. M., UEJI, R. Grain size effect on the martensite formation in a high-manganese TWIP steel by the Rietveld method, *Materials Science and Technology*, v. 26, p. 181-186, 2010.
13. SAHU, P., HAMADA, A.S., GHOSH, R.N., KARJALAINEN, L.P. X-ray diffraction study on cooling-rate-induced $\gamma_{fcc} \rightarrow \varepsilon_{hcp}$ martensitic transformation in cast-homogenized Fe-26Mn-0.14C austenitic steel, *Metallurgical and Materials Transactions A*, v. 38, p. 1991-2000, 2007.
14. HAMADA, A.S., SAHU, P., CHOWDHURY S. G., KARJALAINEN, L.P., LEVOSKA, J., OITTINEN, T. Kinetics of the α' martensitic transformation in fine-grained Fe-26Mn-0.14C austenitic steel, *Metallurgical and Materials Transactions A*, v. 39, p. 462-465, 2008.
15. SAHU, P., HAMADA, A. S., CHOWDHURY, S. G., KARJALAINEN, L. P. Structure and microstructure evolution during martensitic transformation in wrought Fe–26Mn–0.14C austenitic steel: an effect of cooling rate, *Journal of Applied Crystallography*, v. 40, p. 354–361, 2007.
16. LEE, Y-K., CHOI, C-S. Driving force for $\gamma \rightarrow \varepsilon$ martensitic transformation and stacking fault energy of γ in Fe-Mn binary system, *Metallurgical and Materials Transactions A*, v. 31, p. 355-360, 2001.

17. LU, F., YANG, P., MENG, L., CUI, F., DING, H. Influences of thermal martensites and grain orientations on strain-induced martensites in high manganese TRIP/TWIP steels, *Journal of Materials Science and Technology*, v. 27, p. 257-265, 2011.
18. DUMAY, A., CHATEAU, J.-P., ALLAIN, S., MIGOT, S., BOUAZIZ, O. Influence of addition elements on the stacking-fault energy and mechanical properties of an austenitic Fe-Mn-C steel, *Materials Science and Engineering A*, v. 483-484, p. 184-187, 2008.
19. MARTIN, S., ULLRICH, C., ŠIMEK, D., MARTIN, U., RAFAJA, D. Stacking fault model of ε-martensite and its DIFFaX implementation, *Journal of Applied Crystallography*, v. 44, p. 779–787, 2011.
20. VERBEKEN, K., VAN CAENEGEM, N., RAABE, D. Identification of ε martensite in a Fe-based shape memory alloy by means of EBSD, *Micron*, v. 40, p. 151–156, 2009.
21. DING, H., TANG, Z.-Y., LI, W., WANG, M., SONG, D. Microstructures and mechanical properties of Fe-Mn-(Al-Si) TRIP/TWIP Steels, *The Journal of Iron and Steel Research*, v.13, p. 66-70, 2006.
22. K. SUGIMOTO, USUI, N., KOBAYASHI, M., HASHIMOTO, S. Effects of volume fraction and stability of retained austenite on ductility of TRIP-aided dual-phase steels, *ISIJ International*, v. 32, p. 1311-1318, 1992.
23. OLSON, G. B., COHEN, M. A general mechanism of martensitic nucleation: Part I. general concepts and the FCC→HCP transformation, *Metallurgical Transactions A*, v. 7, p. 1897–1904, 1976.
24. YANG, H.-S., JANG, J. H., BHADESHIA, H. K. D. H., SUH, D.W. Critical assessment: Martensite-start temperature for the γ → ε transformation, *CALPHAD: Computer Coupling of Phase Diagrams and Thermochemistry*, v. 36, p. 16–22, 2012.
25. TSUZAKI, K., FUKASAKU, S., TOMOTA, Y., MAKI, T. Effect of prior Deformation of Austenite on the γ→ε martensitic Transformation in Fe-Mn Alloys, *Materials Transactions, JIM*, v. 32, p. 222-228, 1991.

26. SUH, D-W., PARK. S-J., LEE, C-H., KIM, S-J. Microstructure and mechanical behaviors of 0.1C-13Mn metastable austenitic steel, *Metallurgical Transactions A*, v. 40, p. 264-267, 2009.
27. NARAGHI, R., HEDSTRÖM, P., BORGENSTAM, A. Spontaneous and deformation-induced martensite in austenitic stainless steels with different stability, *Steel Research International*, v. 82, p. 337–345, 2011.
28. JUN, J-H., CHOI, C-S. Variation of stacking fault energy with austenitic grain size and its affect on the $M_s$ temperature of $\gamma \rightarrow \varepsilon$ martensitic transformation in Fe-Mn alloy, *Materials Science and Engineering A*, v. 257, p. 353-356, 1998.
29. GÜLER, E., KIRINDI, T., AKTAS, H. Comparison of thermally induced and deformation induced martensite in Fe–29%Ni–2%Mn alloy, *Journal of Alloys and Compounds*, v. 440, p. 168–172, 2007.
30. LIANG, X., WANG, X., ZURO,B H.S. Microstructural characterization of transformable Fe-Mn alloys at different length scales, *Materials Characterization*, v. 60, p. 1224-1231, 2009.

## CHAPTER 4. Microstructural characterization and mechanical behavior of 17%Mn steel with low C


### Abstract

Steels containing high Mn, Si and Al levels have great plasticity when deformed due to TWIP or TRIP effects. Microstructural evolution and its influence on the mechanical behavior were evaluated after warm rolling at 700ºC, cold rolling, with reductions from 4 to 81%, and annealing at 700 and 800°C. The stacking fault energy was estimated at 14.5 mJ/m$^2$, which indicates the possibility of martensitic transformation. Martensite and twinned austenite were verified by optical, SEM micrographs and EBSD. Austenite, $\varepsilon$ and $\alpha$' martensites were confirmed by XRD and dilatometry. Increasing cold reduction provides an $\alpha$' martensite amount development with $\varepsilon$ martensite decreasing. The phase volume fraction, by integrating area peak method, showed that the sample annealed after the highest reduction has no $\alpha$' martensite, indicating that it was more recrystallized. Vickers microhardness values increased with higher cold rolling reduction. However, the microhardness values decreased after annealing and, in general, there is an increasing as function of greater cold reduction.



**Keywords:** Manganese, warm rolling, cold rolling, recrystallization, EBSD examination.


### 4.1. Introduction

Steels containing high Mn, Si and Al contents have high mechanical strength and plasticity due to deformation by mechanical twinning, known as TWIP effect (Twinning Induced Plasticity), or by martensitic transformation, called TRIP effect (Transformation Induced Plasticity)[(1)].

An important parameter that determines the deformation mechanism is the stacking fault energy (SFE), as already cited in Chapter 2. According to Dumay *et al.*[(2)], for SFE values greater than 18 mJ/m$^2$ TWIP effect tends to occur, while for lower values TRIP

effect is predominant and the α' martensite forms for SFE smaller than 12 $mJ/m^2$, and as a consequence the steel ductility reduces[3]. Furthermore, SFE is chemical composition and temperature dependent. It is known that the SFE in Fe-Mn-C alloys is relatively low and for alloys with Mn content less than 15%, TRIP effect dominates, while for Mn content higher than 25% TWIP, effect is dominant. On the other hand, alloys with Mn content between 15% and 25%, TRIP and TWIP effects can coexist [4].

Understanding the deformation mechanisms which act in these alloys when subjected to external loads is very important because they will determine the mechanical properties, such as mechanical strength, ductility and formability for industrial application.

This work aims to evaluate the microstructural evolution and its influence on the mechanical behavior of a 17%Mn steel after warm rolling, cold rolling with different reduction and annealing temperature. The processing applied here is part of a project aimed to produce ultrafine grained steel with TRIP effect.

**4.2. Material and methods**

The steel samples, which the chemical composition cited in Chapter 3, were homogenized at 1100 °C for 2 h and then cooled in air. Afterwards, the samples were reheated to 700°C for 30 min and then warm rolled to 56% thickness reduction.

After warm rolling, the samples were mechanically descaled and then cold rolled with 4, 35, 50 and 81% thickness reduction.

Finally, they were annealed at 700 and 800°C for 30 min, aiming to study the recrystallization evolution. After annealing soaking time the samples were quenched into water.

The microstructural evolution was studied after each cold reduction and annealing step. The microstructure was analyzed by optical and scanning electron microscopy (SEM).

The samples were conventionally ground, electrolytically polished in a solution containing 37 mL $H_3PO_4$, 153 mL $CH_3COOH$ and 10 mL $H_2O$, etched initially with nital 10% and later with Klemm I etchant[5]. Electron Backscatter Diffraction (EBSD) analysis was also carried out to study the microstructure. For this analysis the samples were mechanically polished up to 0.25 μm diamond paste and then with colloidal silica, 0.05 μm.

Dilatometer tests were performed aiming to identify possible reverse martensitic transformations into austenite. The tests were performed from room temperature to 1000°C with 1°C/s heating rate, followed by air cooling. The phase transformation temperatures were determined by the dilatometry curves obtained and its derivatives as a function of temperature.

X-ray diffraction (XRD) analyses were performed in order to identify the phases and to estimate their relative amounts by the integrating area peak method.

The mechanical behavior was evaluated by Vickers microhardness, using 2.91 N (300 g) load with 20 indentations for each sample.

### 4.3. Results and discussion

The value obtained of the stacking fault energy by Dumay *et al.*[2] model was 14.5 $mJ/m^2$ according to calculation in Chapter 3, which indicates the possible martensitic transformation as a possible deformation mechanism beyond the twinning.

Figure 4.1 shows the optical micrographs of the samples annealed at 700 and 800 ºC. Austenite grains with annealing twins and martensite were observed. Klemm I etchant, in principle, reveals austenite as yellow, brown or blue, α' martensite as dark brown and ε martensite as white, but there may be variations in their shades from sample to sample[5].

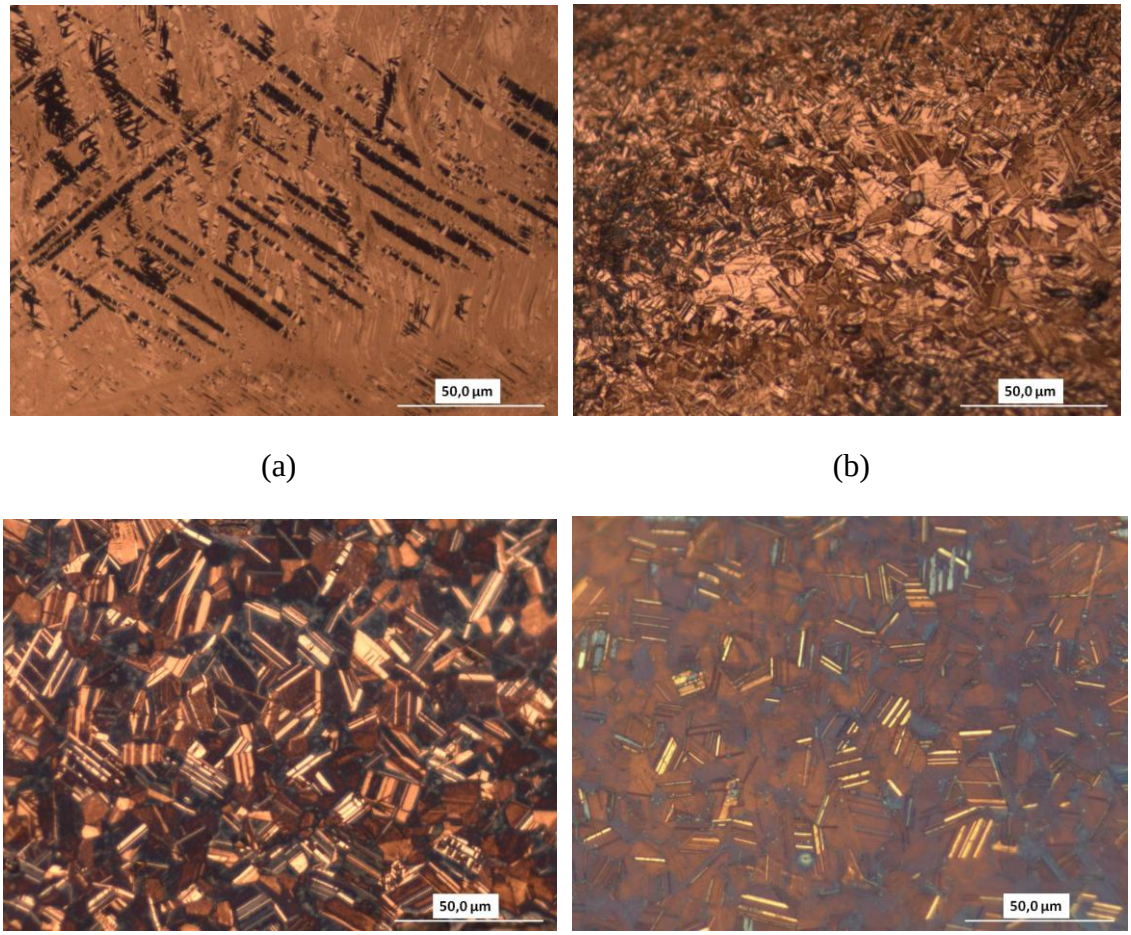


Figure 4.1. Samples annealed at 700ºC, after (a) 4% and (b) 35% cold reduction, and at 800ºC after (c) 50% and (d) 81% cold reduction. Optical micrographs.

Figure 4.2 shows SEM images obtained of the samples annealed at 800 °C after 35 and 50% cold reduction, which validate the three phases existence as well as the microstructural heterogeneities shown by optical microscopy. According to Ding *et al.*[4], the ε martensite nucleates through the stacking faults generated by partial dislocations or from the overlap of these faults, which are created at the active slip planes intersections or at grain boundaries and twins. Moreover, according to Liang[5], there is a difference in crystallographic orientation around 70° between an ε martensite plate and another one, as shown in Fig. 4.2 (a) and (c) by red arrows. The α' martensite is usually formed at the intersection between two ε martensite laths, nevertheless, other

slip planes can act as nucleation site for its formation[3-5], as shown in Figure 4.2 (b) and (c) by black arrows.

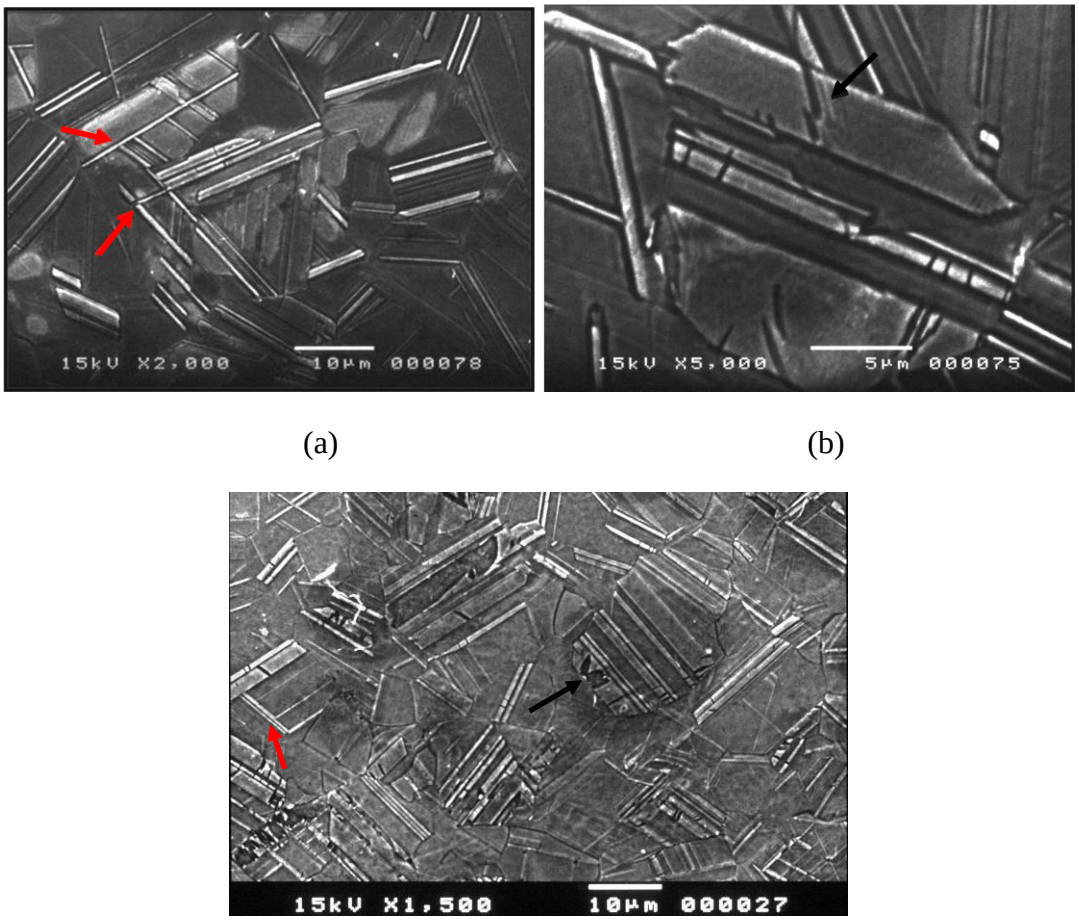


(a) (b)

(c)

Figure 4.2. Samples annealed at 800ºC after 35% (a,b) and after 50% cold reduction (c). SEM micrographs.

Figure 4.3 shows IPF (Inverse Pole Figure) and IQ (Image Quality) maps, respectively, for the samples warm rolled (Fig. 4.3 (a)), cold rolled with 35% reduction and annealed at 800ºC (Fig. 4.3 (b)) and cold rolled with 81% reduction and annealed at 800ºC (Fig. 4.3 (c)). Black arrow indicate α' martensite, while the red show ε martensite and the yellow indicate twins. It was noted in the warm rolled steel (Fig. 4.3 (a)) the presence of elongated austenite grains with twins, as well as evidence of ε martensite formation. In Figure 4.3 (b) there is a very complex microstructure with twinned austenitic grains, α' and ε martensites. Finally, the sample subjected to the greater cold reduction

and annealed at 800°C shows ultrafine twinned austenite grains (Fig. 4.3 (c)) due to the greater work-hardening during cold rolling. This high deformation induces many defects into the grains and makes it more difficult to index the Kikuchi pattern[6]. In addition, the area scanned is relatively small and is not representative to analyze texture.

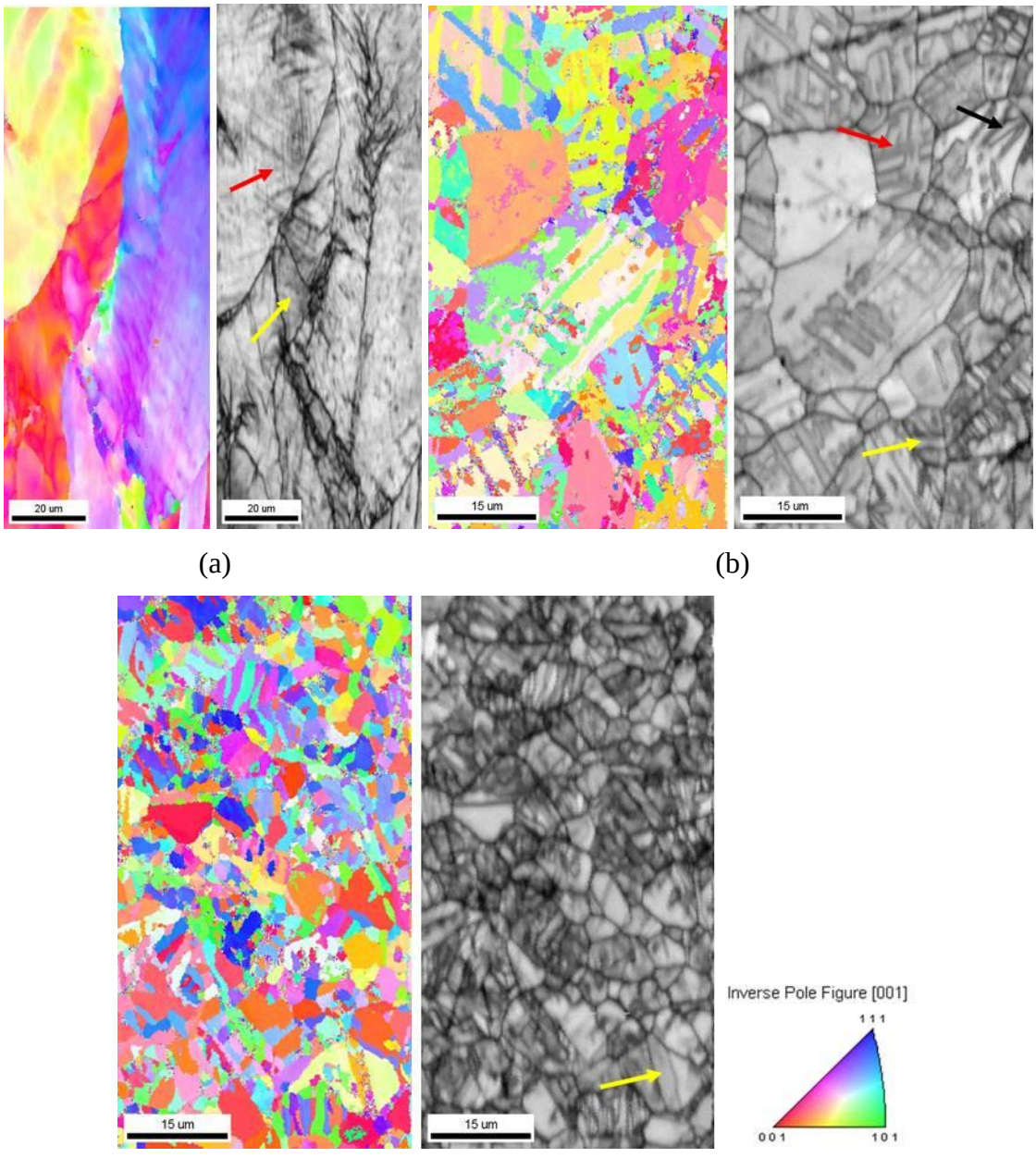


Figure 4.3. EBSD analysis: IPF (Inverse Pole Figure) and IQ (Image Quality) maps for the samples warm rolled (a), cold rolled with 35% reduction and annealed at 800ºC (b) and cold rolled with 81% reduction and annealed at 800ºC (c).

Figure 4.4 shows the dilatometry curves obtained by continuous heating and their derivatives. Figure 4.4 (a) and (d) show the phase transformation occurrence in the temperature ranging from 100°C to 250°C, which corresponds to the reverse austenite from ε martensite transformation. For the temperature ranging from 500 to 700°C, it can be observed the α' martensite reverse transformation in austenite for samples cold rolled to 35% (Fig. 4.4(b)) and 81% (Fig. 4.4(c)) while the ε martensite reverse transformation is difficultly noticeable. These observations demonstrate that the ε martensite occurs only for low deformation amount and for low stacking faults energy associated, and when the deformation increases, there is a tedency to α' martensite formation, which is consistent with the literature[4].

The inflections in dilatometry curves from cold rolled samples (Fig. 4.4 (b,c)) in the temperature ranging between 750ºC and 850ºC correspond to magnetic transformation, that occurs in ferromagnetic material (α' martensite) to paramagnetic (austenite). In pure iron this transition, known as Curie temperature, occurs at 770ºC[7].

According to Lu *et al.*[3], in an alloy containing 17%Mn after tensile test there was an increasing in α' martensite amount and a decreasing of ε martensite for higher deformation.

However, when an alloy containing 22%Mn was used, the same authors verified that when the deformation was increased, there was an increase in both martensites quantities. Therefore, as the chemical composition is similar to the first chemical composition presented by Lu *et al.*[3], it is possible to notice (Fig. 4.5) that the amount of α' martensite in the sample with 81% cold reduction was greater than in the one with 35% cold reduction.

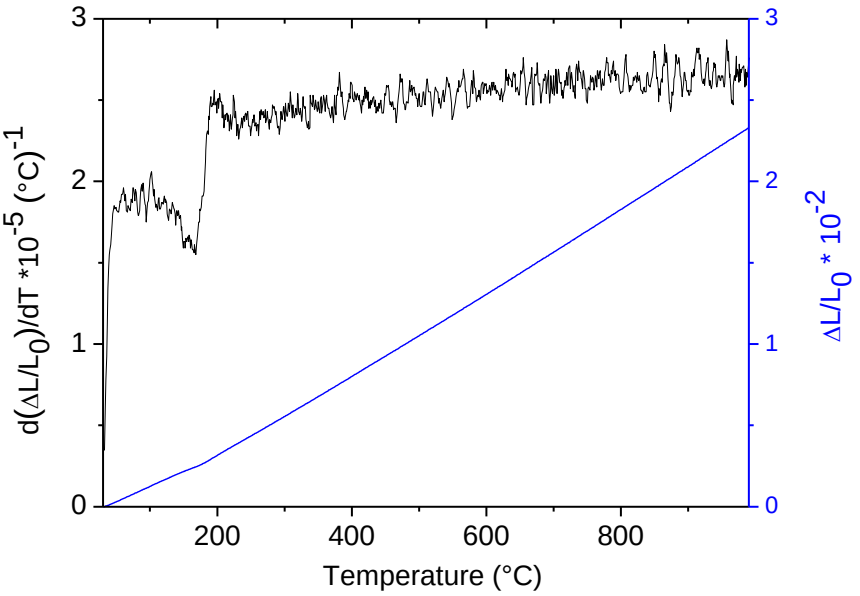


(a)

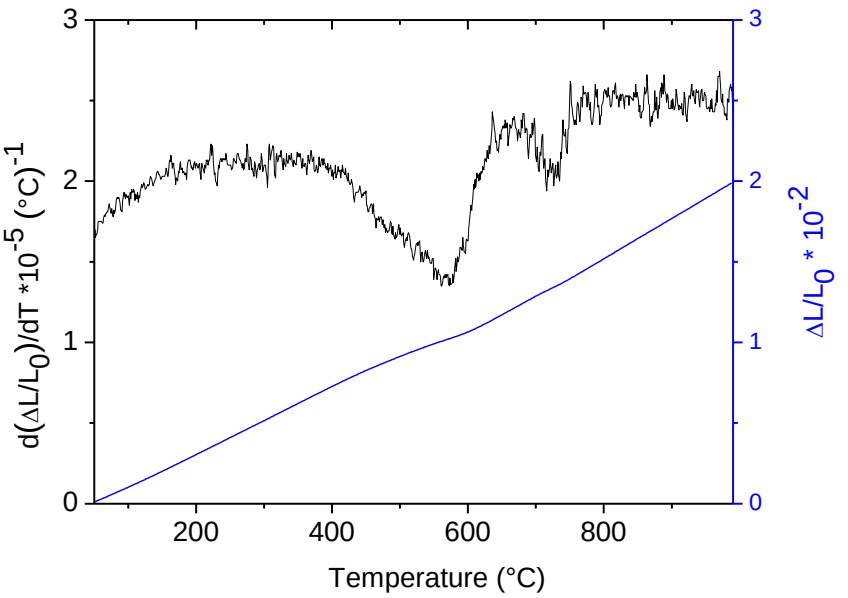


(b)

Figure 4.4. Dilatometric curves and its derivatives as temperature function for the samples: (a) warm rolled, (b) 35% cold rolling reduction, (c) 81% cold rolling reduction, (d) 81% of cold rolling reduction and annealed at 800°C for 300 min.

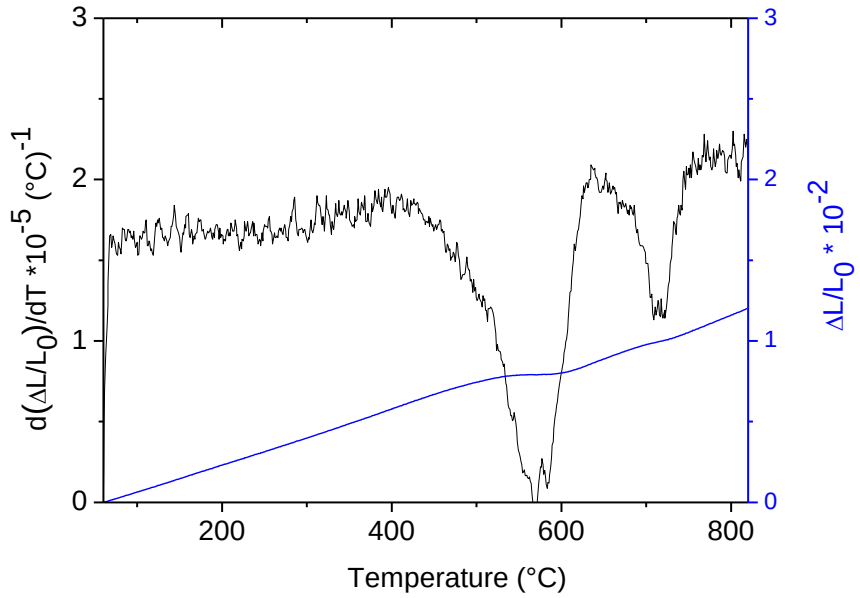


(c)

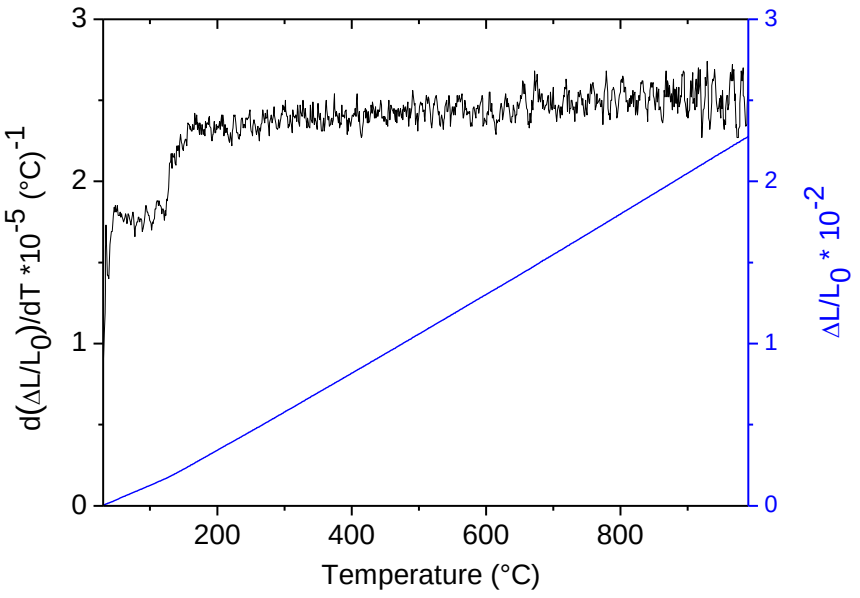


(d)

(cont.) Figure 4.4. Dilatometric curves and its derivatives as temperature function for the samples: (a) warm rolled, (b) 35% cold rolling reduction, (c) 81% cold rolling reduction, (d) 81% of cold rolling reduction and annealed at 800°C for 300 min.

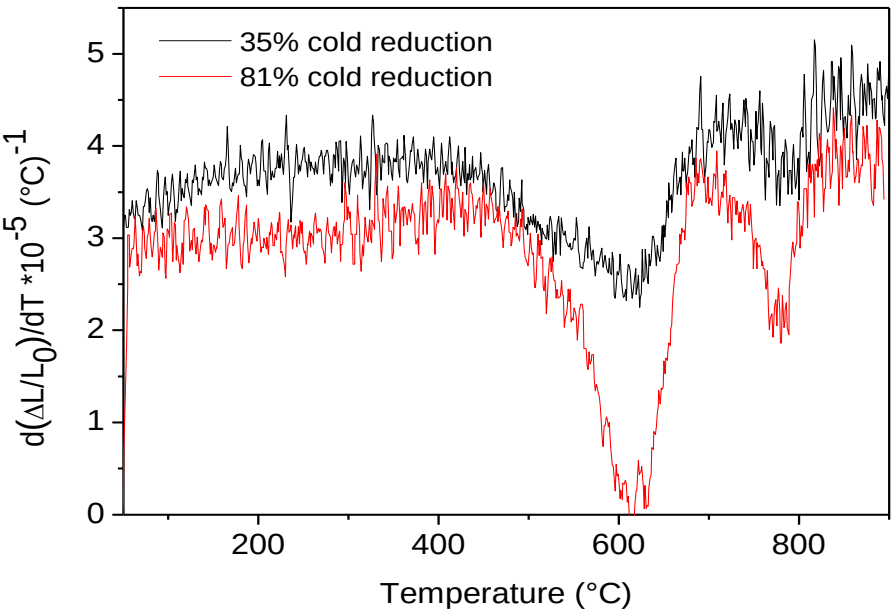


Figure 4.5. Comparison between the numerical derivatives as a function of relative dilatation for the samples with 35 and 81% cold reduction.

X-ray diffraction analysis of the samples annealed at 800°C showed austenite, ε and α' martensites phases presence (Fig. 4.6). Figure 4.7 exhibit the phase volume fraction under different cold reduction after annealing at 800ºC. It is perceived that for reductions up to 50% the volume fraction is practically constant, but for the 81% cold rolled sample the austenite relative amount increased, the ε martensite decreased and α' disappeared. It indicates the greater extension recrystallization under these deformation and annealing conditions.

The results revealed by dilatometric curve (Fig. 4.4 (d)), by optical microscopy (Fig. 4.1 (d)) and by EBSD analysis (Fig. 4.3(c)) for the sample annealed at 800°C after 81% cold reduction corroborates to the results obtained by X-ray diffraction (Fig. 4.6), evidencing the α' martensite absence in this processing condition.

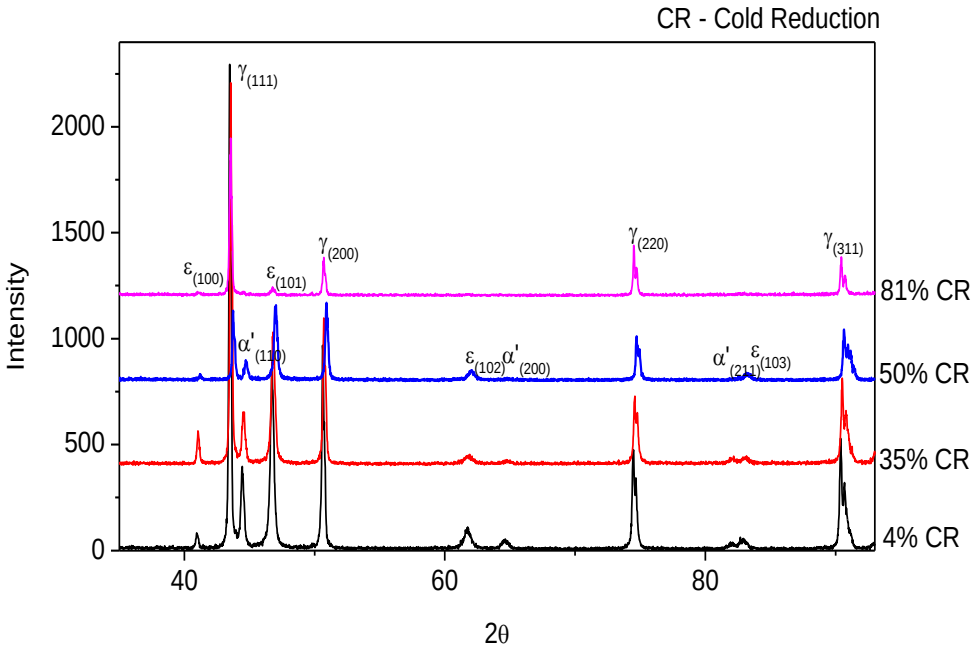


Figure 4.6. XRD patterns of the samples annealed at 800°C for 30 min after different cold reduction.

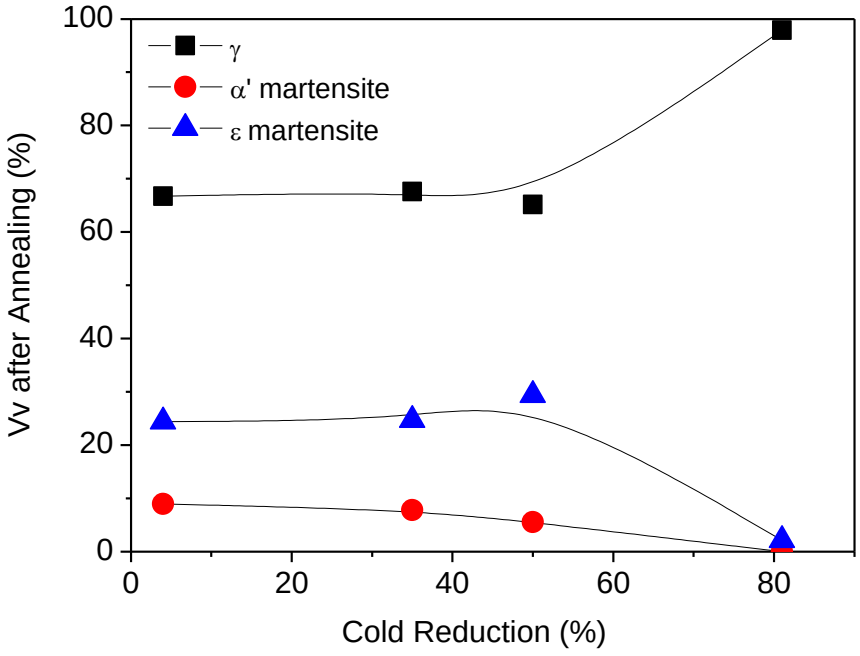


Figure 4.7. Phase volume fraction (Vv) after different cold reduction for the samples annealed at 800ºC.

Tavares *et al.*[8] analyzed a 17Mn-2Al steel and found that the cold rolled samples with 27.5 to 94.8% reduction and annealed at 800°C presented fully austenitic structure. However, these results[8] are not in agreement with the steel under study due to their different chemical composition. Besides Mn and Al, the steel of this work has considerably higher Si content, which enhances martensite formation, since this chemical element reduces the SFE[2]. Moreover, another factor that possibly led to final microstructure was the annealing time used, since the time cited in the literature[8] was twice that used in the present study.

It was confirmed by metallographic analysis, dilatometry and X-ray diffraction that there is $\alpha'$ martensite formation from $\varepsilon$ martensite for more severe deformation. Few references in the literature report the three phases ($\gamma$, $\alpha'$ and $\varepsilon$) existence for these steels through the techniques employed in this work, especially by dilatometry. Ding . *et al.*[4] verified by studying the mechanical behavior under tensile testing of a TRIP/TWIP steel containing 18.8%Mn that the transformation $\gamma \rightarrow \varepsilon \rightarrow \alpha'$ occurs as function of increasing strain, which corroborates to the results obtained in this work.

Figure 4.8 shows Vickers microhardness measurements of the samples cold rolled (a) and annealed at 700ºC (b) and 800ºC (c) under different deformation conditions. As expected, microhardness increases as a function of cold reduction increasing. This occurs due to deformation heterogeneities increase, such as dislocations, mechanical twins, besides the martensitic transformation. After the annealing the microhardness Vickers decreased in relation to that obtained on cold rolling condition, as expected. The sample annealed at 700ºC shows that the microhardness values increased with cold reduction amount, while for that annealed at 800ºC the microhardness values increases for 4% up to 35% reduction. Above this reduction, the microhardness value remained almost constant considering the standard deviation range presented here.

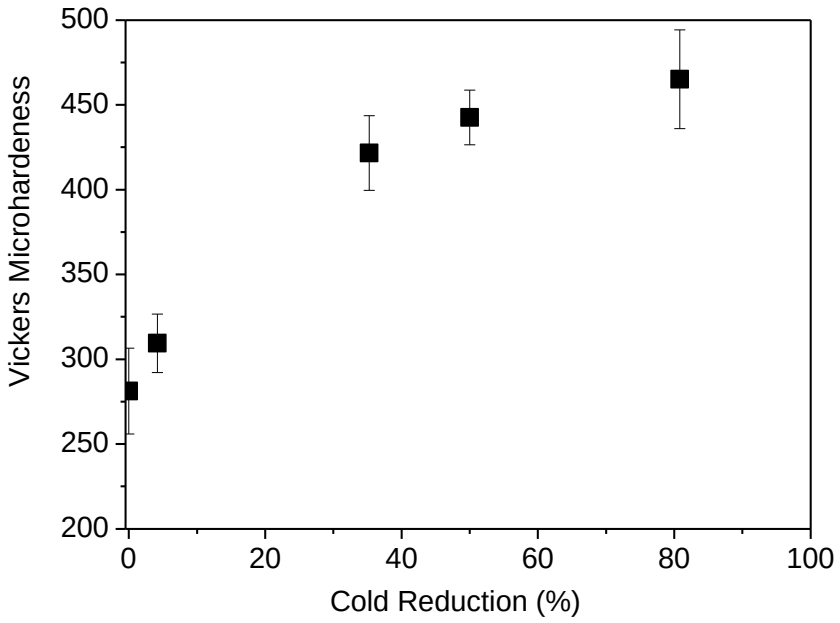


(a)

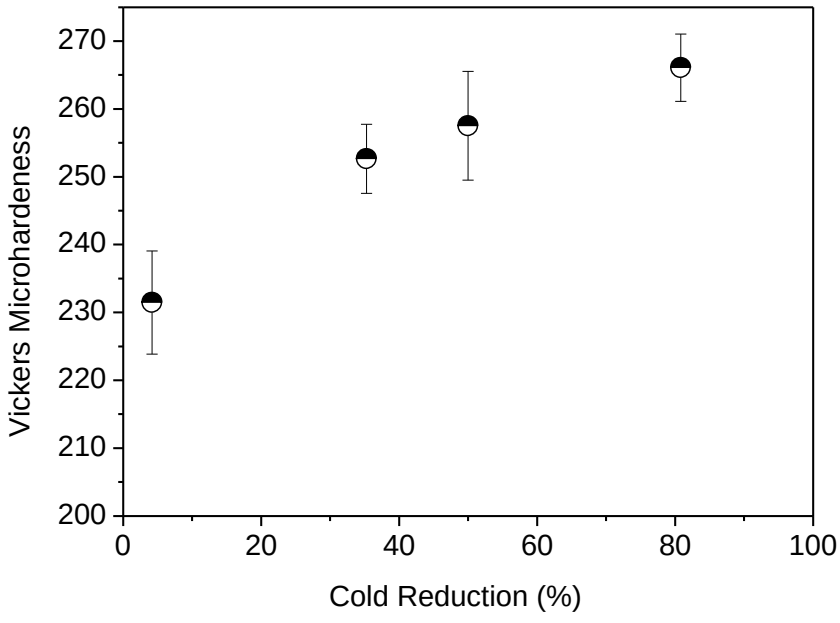


(b)

Figure 4.8. Vickers microhardness as a function of cold rolling reduction for the samples (a) cold rolled, (b) annealed at 700°C and (c) annealed at 800°C for 30 min.

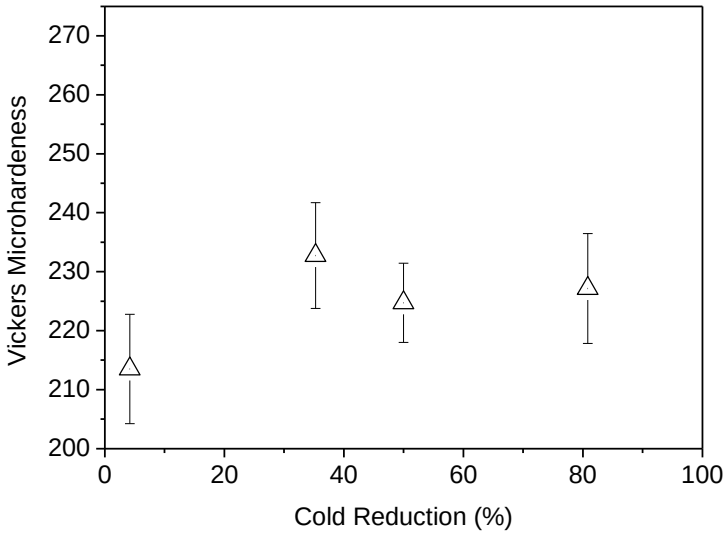


(c)

(cont.) Figure 4.8. Vickers microhardness as a function of cold rolling reduction for the samples (a) cold rolled, (b) annealed at 700°C and (c) annealed at 800°C for 30 min.

Although the cold rolled sample with 81% reduction has been subjected to a greater deformation and a higher recrystallized volume fraction, this sample obtained a microhardness value similar to samples not completely recrystallized, which contain ε and α' martensites. This happened due to a residual strain hardening and a more refined microstructure (Fig. 4.3).

### 4.4. Conclusions

From the results obtained in this work it can be concluded that:

- The cold rolled samples contain austenite, α' and ε martensite. However the ε martensite presence was hardly noticeable by dilatometry for higher deformation amount.

- After cold rolled, the α' martensite volume fraction, estimated by dilatometry, was higher for the 81% reduction sample when compared to that with 35% reduction.

- The microstructures of the samples annealed at 700 and 800°C showed austenite, ε and α' martensites, except for the 81% cold rolled sample and annealed at 800°C, indicating greater recrystallized volume fraction.

- The microhardness value increased as a function of increased cold rolling reduction. However, the samples cold rolled with 35, 50 and 81% thickness reduction and annealed at 800ºC showed similar microhardness values, since the sample with greater deformation amount provided a more refined microstructure in relation to the lower deformed one, which still contains ε and α' martensites in their microstructure.

**Acknowledgements**

The author acknowledges the financial support to carry out this research work by CNPq and CAPES (providing scholarship). SSFD also acknowledges the dilatometry analyses realized by SENAI/CETEF.

**References**

1. FROMMEYER G., BRÜX U., NEUMANN P. Supra-Ductile and High-Strength Manganese-TRIP/TWIP Steels for High Energy Absorption Purposes, *ISIJ International*, v.43, p. 438-446, 2003.
2. DUMAY A., CHATEAU J.P., ALLAIN S., MIGOT S., BOUAZIZ O. Influence of addition elements on the stacking-fault energy and mechanical properties of an austenitic Fe-Mn-C steel, *Materials Science and Engineering A*, v. 483-484A, p. 184-187, 2008.
3. LU F., YANG P., MENG L., CUI F., DING H. Influences of Thermal Martensites and Grain Orientations on Strain-induced Martensites in High

Manganese TRIP/TWIP Steels, *Journal of Materials Science & Technology*, v. 27, p. 257-265, 2011.

4. DING H., DING H., SONG D., TANG Z., YANG P. Strain hardening behavior of a TRIP/TWIP steel with 18.8%Mn, *Materials Science and Engineering A*, v. 528A, p.868-873, 2011.
5. LIANG X., Structure and Mechanical Properties of Fe-Mn Alloys, University of Science and Technology Beijing, China, p. 254, 2008.
6. VERBEKEN, K., CAENEGEM, N.V., RAABE, D. Identification of ε martensite in a Fe-based shape memory alloy by means of EBSD, *Micron*, v. 40, p. 151-156, 2009.
7. CULLITY B.D., GRAHAM C.D., Introduction to Magnetic Materials, 2nd ed., Willey, USA, 2009.
8. TAVARES S.S.M., LAFUENTE A., MIRAGLIA S., FRUCHART D. X-ray diffraction and magnetic analysis of deformation induced martensites in a Fe-17Mn-1.9Al-0.1C steel, *Journal of Materials Science & Technology*, v. 37, p.1645-1648, 2002.

## CHAPTER 5: Effect of cold rolling on martensite formation, recrystallization and mechanical behavior of 17Mn0.06C TRIP/TWIP steel

High Mn steels have great plasticity associated with high mechanical strength due to TWIP and/or TRIP effects. This work evaluated the microstructural evolution and its influence on the mechanical behavior of a steel containing 17%Mn and 0.06%C after hot rolling at 1100ºC, cold rolling with 45% and 90% of reduction and annealing at 700°C for different times. The microstructures were analyzed by optical and scanning electron microscopy. Volume fraction of γ, ε and α' martensites were measured by X-ray diffraction and EBSD technique. It was found that cold reduction increases α' martensite volume fraction. The relative phase amounts showed that the sample annealed for the longest time, 7200 s, still has ε and α' martensite. The yield and tensile strength for annealing condition reach 750 and 950 MPa, respectively, with total elongation of 48%, which confirms the high work hardening rate of the analyzed steel.

**Keywords:** Manganese steel, hot rolling, cold rolling, TWIP steel.

### 5.1. Introduction

Steels containing high levels of Mn, Si and Al, exhibit high plasticity when subjected to deformation due to mechanical twinning effect known as TWIP (Twinning Induced Plasticity), or martensitic transformation, called as TRIP effect (Transformation Induced Plasticity)[1-3]. TWIP/TRIP steels are a promising alternative to attend the demand for automotive components which requires materials with high strength, high formability, low density and good toughness. The capability to absorb impact of these steels is twice that found in conventional high-strength steels used for deep drawing[1,3]. These characteristics led the automotive industries to become interested in the application of this product in order to obtain fuel economy, passenger safety, weight reduction and reduced the greenhouse gas emission to the environment[4,5].

One of the key parameters that determine the mechanism of plastic deformation in these steels is the stacking fault energy , SFE [6-9] as cited in the Chapter 2. SFE controls the

deformation mechanism as TRIP or TWIP[10]. The morphology and the volume fraction of α' martensite is strongly influenced by the ε martensite presence, once α' martensite is formed from the ε martensite, which nucleates in stacking faults[11]. The SFE depends strongly on the chemical composition and deformation temperature. It is known that the SFE of Fe-Mn-C alloys is relatively low and for alloys with Mn content between 15% and 25% , both TRIP and TWIP effects coexist[3]. However, the addition of alloying elements such as Al and Ni increases the SFE and tend to inhibit martensitic transformation ($\gamma_{fcc} \rightarrow \varepsilon_{hc} \rightarrow \alpha'_{bcc}$), whereas Si decreases the SFE, favoring martensite formation[3,11-13].

Another parameter that controls the stability of the austenite is austenitic grain size, since the martensite formation is reduced by a high surface area per volume unit of grain boundaries[14]. On the other hand, increasing the austenite grain size increases the number of potential sites for nucleation of martensite, which is formed in overlapping stacking faults[11]. The austenitic microstructure remains relatively stable during plastic deformation[15]. As deformation proceeds, mechanical twins are formed inside the grains and planar dislocation structures. These twins act similarly to grain boundaries being barriers to dislocations slip, refining the microstructure and thus achieving high elongation values and high energy absorption capacity, despite the high strength[5,16,17].

During deformation, the high work hardening rate of high Mn steels contributes considerably to their fast recrystallization. The low SFE favors cross slip and the formation of subgrains due to deformation, which facilitate this process[16,18]. Many austenic steels such as austenitic stainless steels and high manganese steels have low to moderate SFE, however tend to form stacking faults and twins. These different defect networks affect the texture during cold rolling[19,20]. To achieve a 700 MPa yield strength and a 50% uniform elongation is required a preferentially oriented structure with fine grains obtained by rolling and recrystallization processes[16].

This study aimed to evaluate the effect of cold rolling on the formation of ε and α' martensite, as well as the recrystallization behavior of a 17%Mn and 0.06%C TRIP/TWIP steel annealed at 700°C with different times. During the processing steps

the ε martensite formation occurs, which then transforms into α'. This affects the mechanical properties of the alloy significantly. The chemical composition of the alloy used, particularly its low carbon content as well as its processing, has been little reported in the literature. However, the achieved results are promising for steel application in automotive industries.

### 5.2. Material and methods

The chemical composition of the steel in this study was shown in Chapter 3 (Table III.1). The steel was homogenized at 1100°C for 2h and then cooled in water. After homogenization, the samples were cut to hot rolling at 1070°C, in four equal reduction passes, leading to a 50% thickness reduction. The resulting thickness was 10.2 mm.

The material was cold rolled in 7 equal passes with a total 44% thickness reduction with 7 mm resulting thickness. Another sequence of 32 passes was applied to obtain 90% reduction with a final thickness of 1.05 mm. The steel was annealed at 700°C during 10, 60, 100, 200, 500, 700, 1000, 1800, 3600 and 7200 s and then cooled in water after soaking.

After annealing, the samples were conventionally prepared and polished up to 0.25 μm diamond paste. Subsequently, the automatic polishing was carried out with a solution of Struers OP-S during 90 min. The examined section corresponds to RD (rolling direction)-TD (transversal direction). The microstructure was characterized by optical microscopy and scanning electron microscopy (SEM) after etching with Nital 10% followed by Klemm I etchant. X-ray diffraction was performed at room temperature on a Philips diffractometer PW 1710. Quantification of austenite, ε and α' martensites was conducted by the method of integrating the area peaks. The integrated intensities were performed using a graphic software following the methodology described by Dafé *et al.*[16]. Electron backscatter diffraction (EBSD) was performed to quantify the microstructure and obtain microtexture. Tensile tests at room temperature with a $10^{-3}$ $s^{-1}$ strain rate and Vickers microhardness measurements with 2.9 N (300g) load were also

performed to determine the variations of recrystallized fraction according to the mechanical behavior.

## 5.3. Results and discussion

### *5.3.1. Microstructural characterization*

Figure 5.1 shows optical micrographs obtained for the samples annealed during 1800 s and 7200 s. It is observed the presence of austenitic grains having annealing twins and ε and α' martensites. The reactive Klemm I, as cited in the Chapter 4, colors the austenite as yellow, brown or blue, the α' martensite as dark brown and ε martensite as white[20].

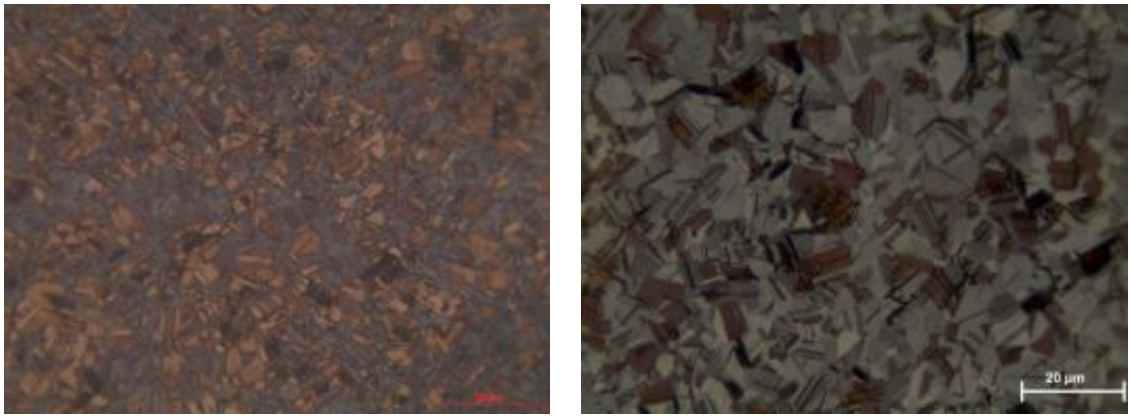


(a) (b)

Figure 5.1. Optical micrographs for the samples cold rolled with 44% thickness reduction and annealed during (a) 1800 s and (b) 7200 s.

Figure 5.2 shows the SEM micrographs for samples annealed during 60, 500 and 1800 s, which show the phases present as well as the heterogeneities on nucleation and grain growth. According to Ding *et al.*[19], ε martensite nucleates on stacks faults or twins and grain boundaries. Moreover, according to Liang *et al.*[20], there is a 70° misorientation between two ε martensite plates. On the other hand, α' martensite is usually formed at the intersections of two ε martensite laths, however, other slip planes can act as nucleation sites[11,14,17]. The ε martensite appears as clear bands (plates or laths) and α' as dark regions.

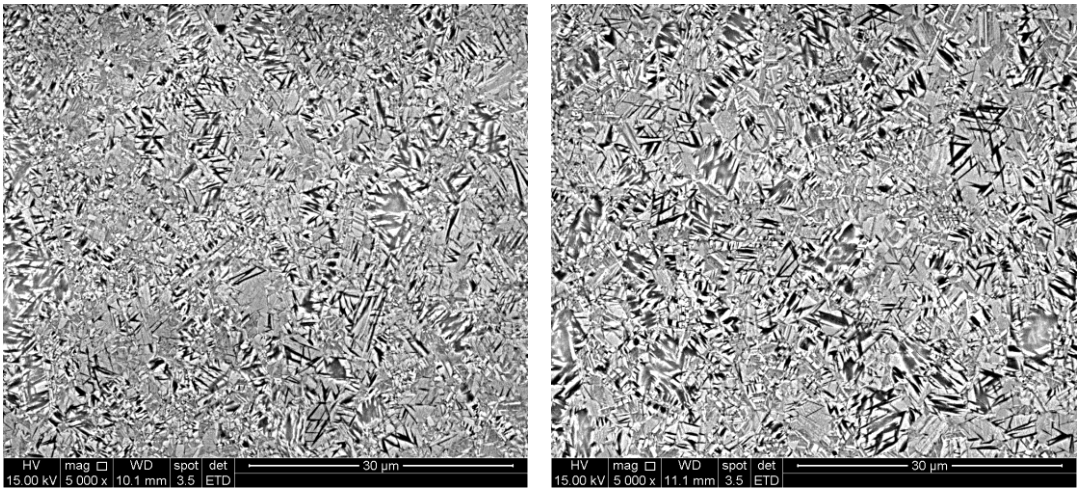


(a) (b)

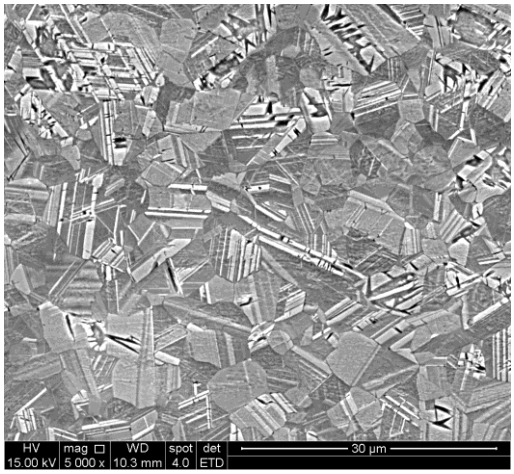


(c)

Figure 5.2. SEM micrographs for the samples cold rolled with 44% thickness reduction and annealed during (a) 60 s, (b) 500 s and (c) 1800 s.

Figure 5.3 shows the SEM micrographs of samples annealed during 100, 300 and 1000 s after cold rolling with 90% reduction in thickness. In Figure 5.3 (a) most of the microstructure is work hardened. Observation at high magnification in SEM has revealed the recrystallization beginning, polygonal regions as darker regions (Fig. 5.3 (a)). After annealing for 300 s the microstructure recrystallizes, forming nanograins (Fig. 5.3 (b)). In Figure 3 (c) it is more clearly observed the presence of ε martensite laths as bright regions and α' martensite needles as series of zig-zag or forming equilateral triangles (compare with Fig. 5.2 (c)) in a austenitic matrix.

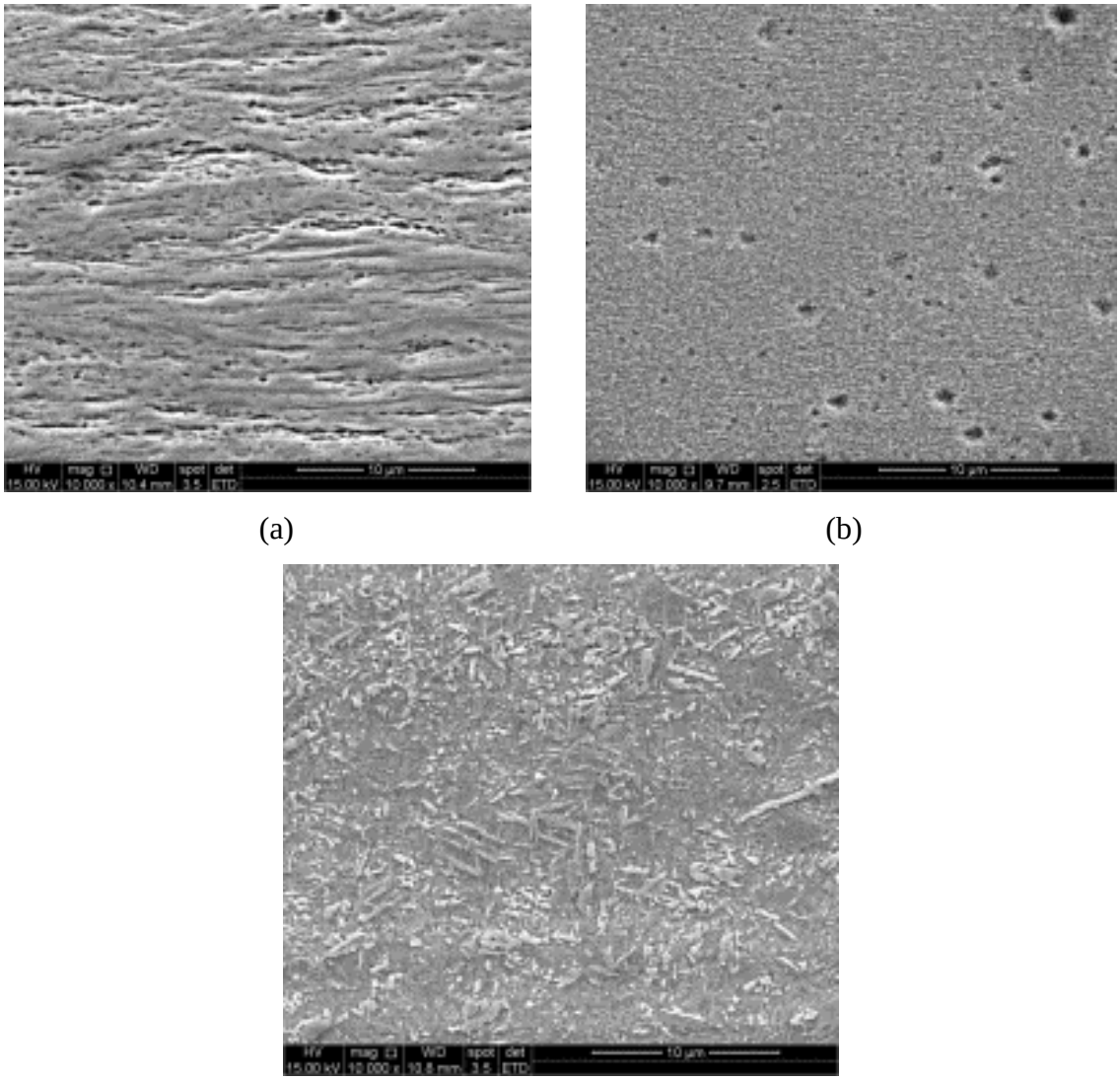

(a) (b)

(c)

Figure 5.3. SEM micrographs for the samples cold rolled with 90% thickness reduction and annealed during (a) 100 s, (b) 300 s and (c) 1000 s.

X-ray diffraction analysis confirmed the presence of austenite and ε and α' martensites (Fig. 5.4) in samples cold rolled with 44% thickness reduction and subsequently annealed during 60, 1800, and 7200 s at 700°C. By the same way Figure 5.5 shows these three phases for the sample 90% cold rolled and annealed at 700°C during 700 s while the sample cold rolleds show mostly α' martensite.

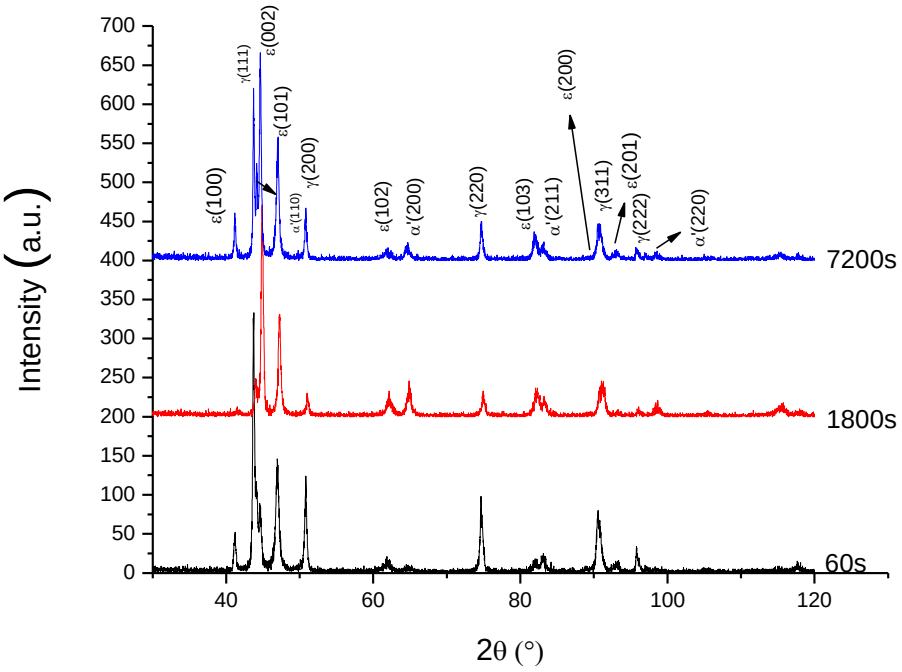


Figure 5.4. Diffractograms of samples cold rolled with 44% thickness reduction and annealed at 700°C during 60, 1800 and 7200 s.

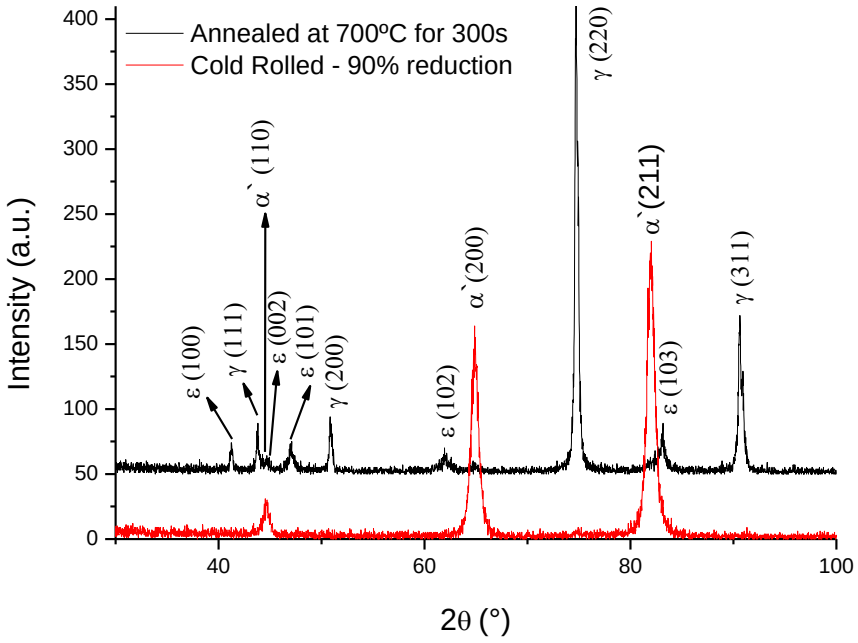


Figure 5.5. Diffractograms of samples cold rolled with 90% thickness reduction and annealed at 700°C during 300 s.

The amount of each phase for samples initially 44% cold rolled and then annealed at different times is plotted in Figure 5.6. Initially there is an increasing in austenite and a decrease in both ε and α' martensites fractions as function of the annealing time. In a second stage there is a reduction in the volume fraction of austenite and ε martensite with increasing annealing time. This shows that even then there is no formation of these martensites on quenching and only for longer times, which provided larger austenitic grain sizes and then the martensite formation during the subsequent cooling. The ε martensite amount is favored by higher austenitic grain size, as at 7200 s. Moreover, a reduction in the amount of α' martensite occurs. However, for longer annealing times as 7200 s, there is a significant amount of ε and/or α' martensites.

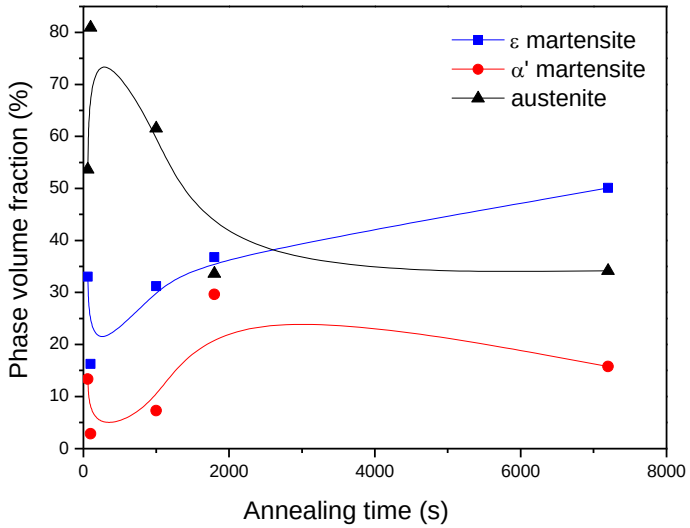


Figure 5.6. Relative amount of austenite, α' and ε martensites for samples initially 44% cold rolled and then annealed for different times.

Table V.1 presents the relative amount of phases for samples initially 90% cold rolled and annealed at 700°C during 300 s. It is noted that the sample just cold rolled is formed mostly by α' martensite from the high deformation imposed. On the other hand, after annealing the sample has a high amount of austenite, and a low fraction of α' and ε martensites which were also formed on quenching as described for samples 44% cold rolled and annealed during different times.

Table V.1 - Relative amount of austenite, α' and ε martensites for samples initially 90% cold rolled and annealed at 700°C during 300 s.

| Sample | Volume fraction (%) | | |
|---|---|---|---|
| | ε | α | γ |
| Cold rolled | - | 98.5 | 1.5 |
| Annealed at 700°C, 300s | 12.6 | 3.9 | 83.5 |

Measurement of grain size was performed using Image Pro Plus™ with images obtained by EBSD. The method used corresponds to that established in ASTM E112 standard. Figure 5.7 shows some images obtained by EBSD used in the measurements at different annealing times.

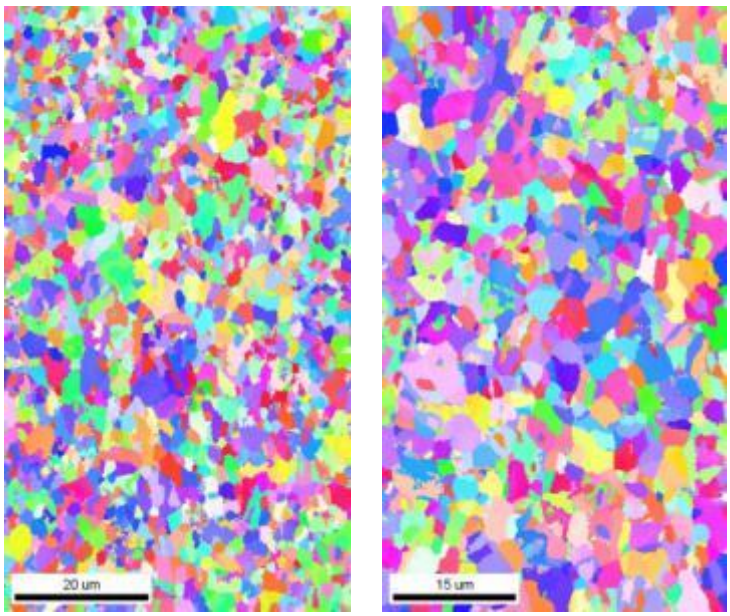


(a) (b)

Figure 5.7. EBSD-IPF maps for samples after 44% cold reduction annealed for: (a) 10 s, (b) 1800 s, (c) 7200 s, (d) Quality Index map and (e) misorientation degree map (for the last heat treatment). Low angle grain boundaries, (LAGB, $2° \leq \theta < 15°$) in red and green; high angle grain boundaries, (HAGB $\theta > 15°$) in blue.

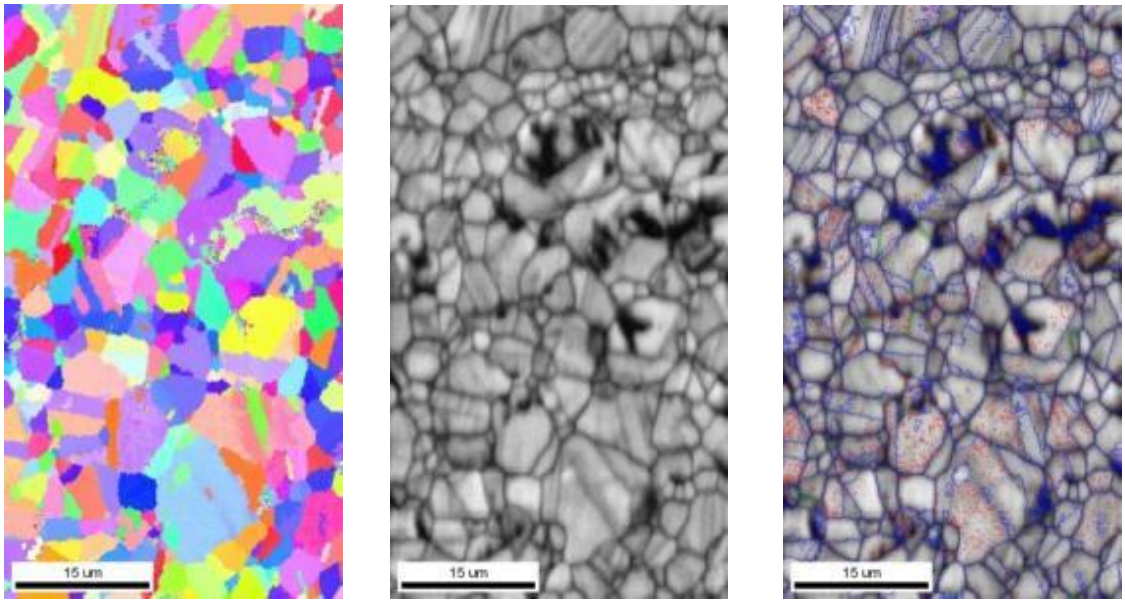


(c) (d) (e)

(cont.) Figure 5.7. EBSD-IPF maps for samples after 44% cold reduction annealed for: (a) 10 s, (b) 1800 s, (c) 7200 s, (d) Quality Index map and (e) misorientation degree map (for the last heat treatment). Low angle grain boundaries, (LAGB, $2° \leq \theta < 15°$) in red and green; high angle grain boundaries, (HAGB $\theta > 15°$) in blue.

The results of grain size quantitative analysis for the different samples are shown in Figure 5.8.

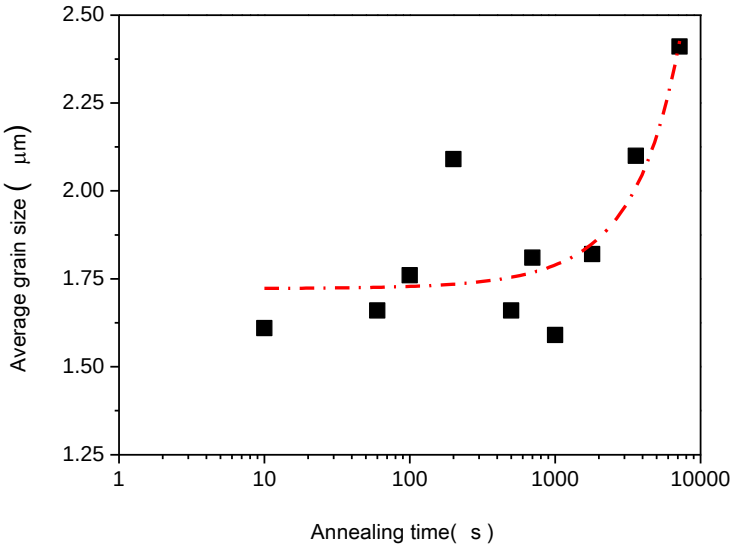


Figure 5.8. Average grain size of samples cold rolled with 44% thickness reduction and annealed during different times.

*5.3.2. Mechanical properties*

Figure 5.9 shows Vickers hardness results for samples 44% cold rolled and annealed from 10 to 7200 s. After heat treatments is noted a marked decrease in microhardness during the initial periods of isothermal annealing. Similar behavior was observed by Liu *et al.*[18] with an 24%Mn- 0.02%C alloy. The first plateau shown in Figure 5.9 refers to the steel recrystallization (hardness about 250 HV), while the second one corresponds to grain growth (hardness about 225 HV). During the annealing, dislocations in excess are eliminated[21] as well as the deformation microtwins[11]. In addition there is the occurrence of austenite reversion from martensite. These transformations reduces the hardness.

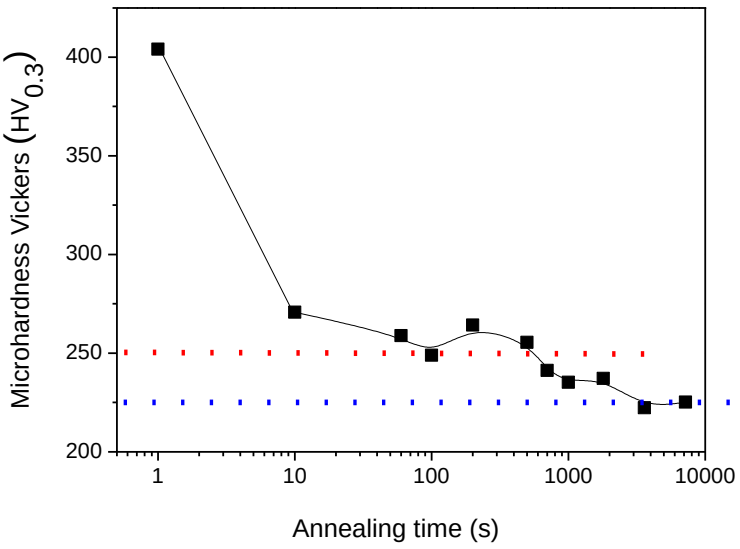


Figure 5.9. Microhardness Vickers as function of the annealing time for the sample innitially 44% cold rolled.

Figures 5.10 show the curves obtained by tensile test for samples hot rolled (Fig. 5.10 (a, b)) and 90% cold rolled (Fig. 5.10 (c)) as well as annealed during 300 s at 700°C (Fig. 5.10 (d, e)). In Figures 5.10 (b, e) are also shown the work hardening curves obtained from the respective tensile curves. The intersection between the true stress and work hardening rate curves gives the strain hardening exponent value, "n" according to the Considére criterion[22].

It was noted that even for an almost fully martensitic microstructure, for the sample 90% cold rolled (Fig. 5.10 (c)) there is a notary elongation. The yield strength and tensile strength reached 250 MPa and 800 MPa, respectively, with 40% total elongation for hot rolled steel (Fig. 5.10 (a)). On the other hand, the 90% cold rolled and annealed steel (Fig. 5.10 (d)) showed 750 MPa and 950 MPa to yield strength and tensile strength, respectively, with a high work hardening ability, "n" equal to 0.33. The total elongation for this last condition cited above was 48%. These values are considered to be high[9,19,22].

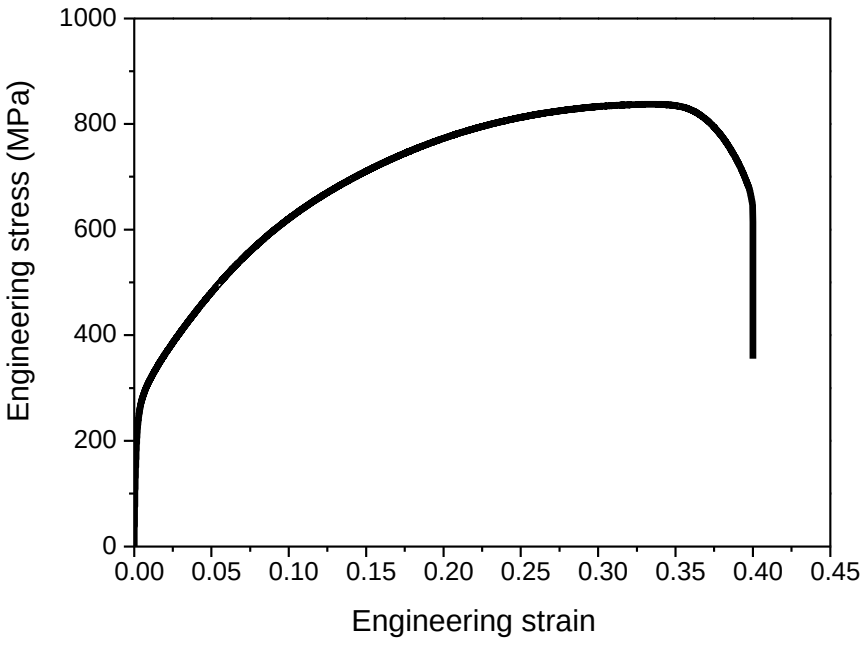


(a)

Figure 5.10. Engineering stress versus engineering strain and work hardening rate for the samples hot rolled (a, b), and also for the 90% cold rolled sample (c) as well as after annelling at 700 ºC during 300 s (d, e).

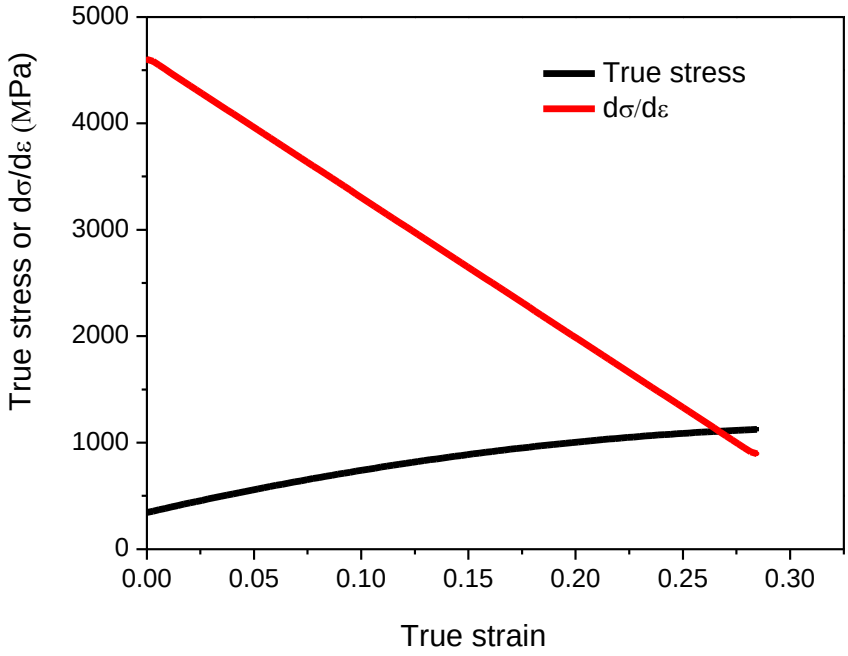


(b)

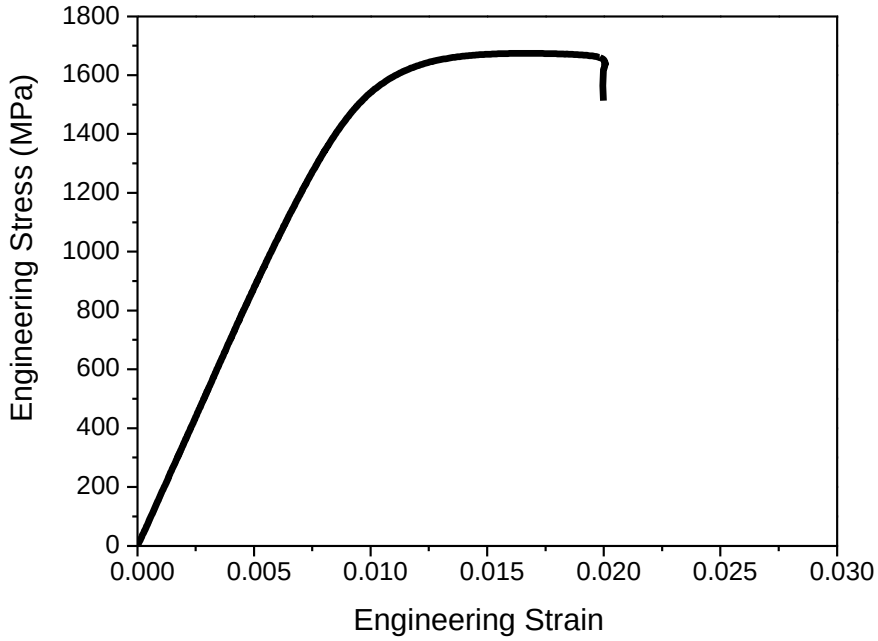


(c)

(cont.) Figure 5.10. Engineering stress versus engineering strain and work hardening rate for the samples hot rolled (a, b), and also for the 90% cold rolled sample (c) as well as after annelling at 700 ºC during 300 s (d, e).

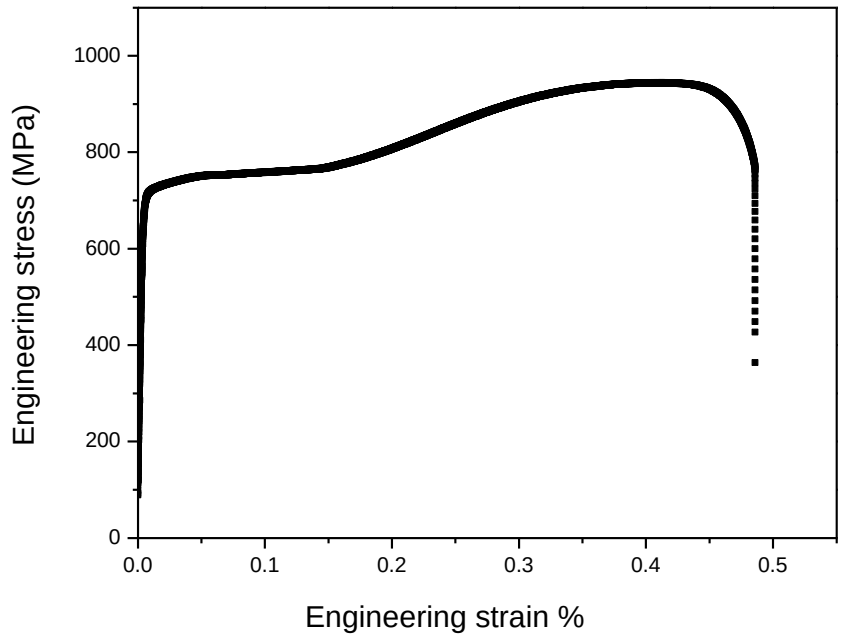


(d)

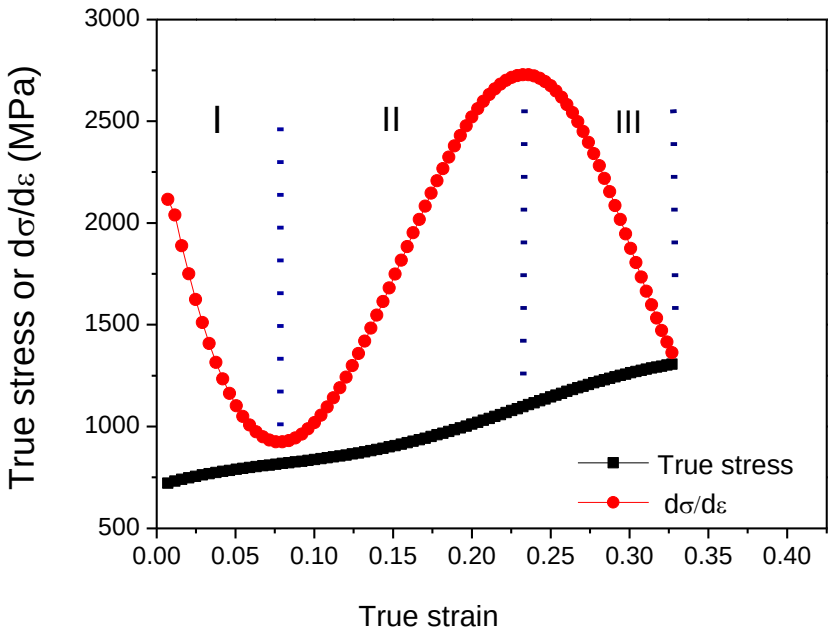


(e)

(cont.) Figure 5.10. Engineering stress versus engineering strain and work hardening rate for the samples hot rolled (a, b), and also for the 90% cold rolled sample (c) as well as after annelling at 700 ºC during 300 s (d, e).

Figure 5.10 (e) shows that strain hardening curve for the 90% cold rolled steel and annealed exhibits at least three stages as plastic deformation proceeds during the tensile test. Stage I corresponds to dislocation slip and the formation of deformation twins. Stage II corresponds to the formation of strain-induced martensite and, finally, at the stage III the three deformation mechanisms compete with each other until the sample ruptures. Similar behavior was also verified by Hao *et al.*[19]. In this case, the authors added a further stage, corresponding to elastic region in tensile test, dividing the work hardening rate curve in four stages. In this work the elastic region was deregarded, since there is no reason to discuss uniform deformation once the yielding has not started and the yield point was not reached yet. On the other hand, increasing the strain induces saturation on the formation of deformation twins. As shown in the literature, for a stainless austenitic stainless steel with 18%Mn-0.6%C the grain is subdivided gradually as the deformation microtwins are generated[9], leading to greater difficulty for nucleating and growing.

For a steel with 18%Mn-2.9%Al-2.9%Si and 0.04%C, Hao *et al.*[19] reported severe ε martensite formation in stage III, resulting in α' martensite formation directly from austenite. At this stage austenite is highly tensioned and this facilitates its transformation. The ε martensite formation with 0.1 true strain was also reported by Liang *et al.*[20] for a steel with 24%Mn-0.01%C and by Zhang *et al.*[13] with a 30%Mn-4%Si-2%Al steel, both to tensile tested at room temperature[20]. However no α' martensite formation was reported in both experiments.

## 5.4. Conclusions

- The steel after annealing for 7200 s still sowed ε and α' martensite but the microhardness test indicated recrystallized condition.
- The Vickers microhardness was higher for the cold rolled condition, due to hardening, besides a high α' martensite volume fraction. The microhardness decreased for recrystallized samples. However, this reduction was counterbalanced by the formation of athermal martensite during the cooling process. The recrystallized grain size follows an exponential behavior during its

growth. The final grain size is very small, about 3 μm, after annealing at 700°C during 7200 s.

- The yield strength and tensile strength in the hot rolled condition reached values near 250 MPa and 800 MPa, respectively, with the total elongation of 40%. The yield strength and tensile strength for 90% cold rolled and annealed sample reached values close to 750 MPa and 930 MPa, respectively, with 48% total elongation, confirming the high work hardening rate (n=0.33). The hardening ability is enhanced due to the TRIP effect resulting from strain-induced martensitic transformation.

**Acknowledgments**

The author thank FAPEMIG (process number TEC PPM-00373/11), CNPq (process number 471128/2011-2) and CAPES (scholarship of SSFD) for the financial support of this research.

**References**

1. KIM, Y. G., KIM, T. W., HAN, J. K., CHANG, R. W. Development of new austenitic Fe-Mn-Al-C steels for automotive applications, *Key Engineering Materials*, v. 84-85, p. 461-471, 1993.
2. GRASSEL, O., FROMMEYER, G., DERDER, C., HOFMANN, H. Phase Transformation and Mechanical Properties of Fe–Mn–Si–Al TRIP-steels, *Journal of Phyisique IV*, v. C5, p. 383–388, 1997.
3. FROMMEYER, G.; BRÜX, U.; NEUMANN, P. Supra-Ductile and High-Strength Manganese-TRIP/TWIP Steels for High Energy Absorption Purposes, *ISIJ International*, v. 43, n. 3, p. 438–446, 2003.
4. LI, D. Z., WEI, Y. H., XU, B. S., HOU, L. F., HAN, P. D. Development in fundamental research on TWIP steel used in automobile industry, *Ironmaking and Steelmaking*, v. 38, n.7, p. 540-545, 2011.
5. DE COOMAN, B. C., KWON, O., CHIN, K. G. State-of-the-knowledge on TWIP steel, *Materials Science and Technology*, v. 28, p. 513-527, 2012.

6. BOUAZIZ, O., ALLAIN, S., SCOTT, C. P., CUGY, P., BARBIER, D. High manganese austenitic twinning induced plasticity steels: A review of the microstructure properties relationships, *Current Opinion in Solid State and Materials Science*, v.15, p. 141-168, 2011.
7. LU, Y., MOLODOV, D. A., GOTTSTEIN, G. Recrystallization kinetics and microstructure evolution during annealing of a cold-rolled Fe–Mn–C alloy, *Acta Materialia*, v. 59, p. 3229–3243, 2011.
8. VERCAMMEN, S., BLANPAIN, B., DE COOMAN, B.C., WOLLANTS, P. Cold rolling behavior of an austenitic Fe–30Mn–3Al–3Si TWIP-steel: the importance of deformation twinning, *Acta Materialia*, v. 52, p. 2005–2012, 2004.
9. JIN, J. E.; LEE, Y. K. Strain hardening of a Fe-18Mn-0.6C-1.5Al TWIP steel, *Materials Science and Engineering A*, v. 527, p. 157–161, 2009.
10. DUMAY, A., CHATEAU, J. P., ALLAIN, S., MIGOT, S., BOUAZIZ, O. Influence of addition elements on the stacking-fault energy and mechanical properties of an austenitic Fe-Mn-C steel, *Materials Science and Engineering A*, v. 483-484, p. 184-187, 2008.
11. BRACKE, L., KESTENS, L., PENNING, J. Influence of α'- martensite in an austenitic Fe-Mn-C-N alloy, *Scripta Materialia*, v. 57, p. 385-388, 2007.
12. LU, F., YANG, P., MENG, L., CUI, F., DING, H. Influences of Thermal Martensites and Grain Orientations on Strain-induced Martensites in High Manganese TRIP/TWIP Steels, *Journal of Materials Science & Technology*, v. 27, n. 3, p. 257-265, 2011.
13. ZHANG, X., SAWAGUCHI, T., OGAWA, K., YIN, F., ZHAO, X. Deformation microstructure of TRIP/TWIP Steels at the early deformation stages, *ESOMAT 2009*, p. 1-8, 2009.
14. DINI, G., NAJAFIZADEH, A., MONIR-VAGHEFI, S. M., UEJI, R. Grain Size Effect on the Martensite Formation in a High-Manganese TWIP Steel by the Rietveld Method, *Journal of Materials Science & Technology*, v. 26, n. 2, p. 181-186, 2010.
15. SANTOS, D. B., SALEH, A. A., GAZDER, A., CARMAN, A., DUARTE, D. M., RIBEIRO, E. A. S., GONZALEZ, B. M., PERELOMA, E. V. Effect of Annealing on the Microstructure and Mechanical Properties of Cold Rolled Fe-24Mn-3Al-

2Si-1Ni-0.06C TWIP Steel, *Materials Science Engineering A*, v. 528, p. 3545-3555, 2011.

16. DAFÉ, S. S. F., MOREIRA, D. R., MATOSO, M. S., GONZALEZ, B. M., SANTOS, D. B. Martensite Formation and Recrystallization Behavior in 17Mn0.06C2Si3Al1Ni TRIP/TWIP Steel after Hot and Cold Rolling, *Materials Science Forum*, v. 753, p. 185-190, 2013.
17. RONG-GANG, X., REN-YU, F., QIAN, L., XI-CHENG, W., LIN, L. Tensile Properties of TWIP Steel at High Strain Rate, *Journal of Iron and Steel Research*, v. 16, n. 1, p. 81-86, 2009.
18. LIU, J. B., LIU, X. H., LIU, W., ZENGB, Y. W., SHU, K.Y. Microstructure and hardness evolution during isothermal process at 700ºC for Fe-24Mn-0.7Si-1.0Al-TWIP steel, *Materials Characterization*, v. 61, p. 1356-1358, 2010.
19. DING, H., DING, H., SONG, D., TANG, Z., YANG, P. Strain hardening behavior of a TRIP/TWIP steel with 18.8%Mn, *Materials Science and Engineering A*, v. 528, p. 868-873, 2011.
20. LIANG, X., McDERMID, J.R., BOUAZIZ, O., WANG, X., EMBURY, J.D., ZUROB, H.S. Microstructural evolution and strain hardening of Fe–24Mn and Fe–30Mn alloys during tensile deformation, *Acta Materialia*, v. 57, p. 3978–3988, 2009.
21. RIOS, P.R., JUNIOR, F. S., SANDIN, H. R.Z., PLAUT, R. L., PADILHA, A. F. Nucleation and Growth during Recrystallization, *Materials Research*, v. 8, n. 3, p. 225-238, 2005.
22. DIETER, G.E. Mechanical Metallurgy. McGraw-Hill Book Company, London, SI Metric Edition, 1988. Cap. 8, p. 275-324.

## CHAPTER 6. Study of α' Martensite reversion in austenite in a 17%Mn TRIP/TWIP steel with low C after different cold reduction and annealing

**Abstract:**

Steels which present strain-induced phase transformations and mechanical twinning are known to have extraordinary mechanical properties such as high strength and good ductility simultaneously. These mechanical properties make them attractive for automotive applications. The present work focuses on 17%Mn steel with low carbon content which presents both TRIP (Transformation Induced Plasticity) and TWIP (Twinning Induced Plasticity) effects during deformation. The steel was subjected to cold rolling with 60 and 90% reduction followed by annealing at different temperatures. It was used X-ray line profile analysis using the software Materials Analysis Using Diffraction (MAUD) based on Rietveld method, as well as Hardness Vickers and Transmission Electron Microscopy (TEM) analyses for the microstructural characterization. It was observed after annealing that hardness is not just influenced by the finer austenitic microstrusture formed in the deformed samples but it is also a consequence of the initial amount of α' martensite available for reversing. The reversion is more effective and faster at higher temperatures when there is greater stored energy from deformation process. The MAUD and TEM analyses also confirmed that the α' martensite to austenite reversion occurs via shearing together with diffusion mechanism.

**Keywords:** High manganese steel, cold rolling, annealing, austenite reversion, X-ray line profile analysis

### 6.1. Introduction

High strength and good ductility combination is the main objective of structural materials design for automotive industries. The reduction of vehicle mass, the lowering of pollutant gas emissions and the improvement of passenger safety, trough large energy absorption capability for vehicle crashworthiness, require this characteristic. Based on

these industrial requirements researches have been developed on new strain-hardening mechanisms which increase the strength of steel without loss of ductility. In this context steels with high manganese content as TRIP (Transformation Induced Plasticity) and TWIP (Twinning Induced Plasticity) have emerged[1].

The twinning and martensite formation can accompany plastic deformation during the deformation process in TRIP or TWIP steels and it determines how stable austenite will be. According to the chemical composition of these steels, temperature and amount of stress applied the martensitic transformation can occur[2-7].

The stacking fault energy (SFE) is an important parameter that determines the deformation mechanism. Chemical composition and temperature have strong influence on SFE. It is known that for Fe-Mn-C alloys containing less than 15%Mn the TRIP effect dominates, while for contents above 25% the TWIP effect is dominant. However, as cited in Chapter 4, for alloys with Mn content between 15% and 25%, the TRIP and TWIP effects coexist[8].

Depending on temperature the α' martensite, formed by deformation or cooling, can be metastable and its reversion to austenite can occur in two forms, called athermal shear mechanism and isothermal diffusion mechanism[9, 10]. The literature has shown that a reversion of the martensite in austenitic stainless steels occurs at temperatures lower than the recrystallization. In the case of reversion of α' martensite it is complete at about 750°C[10,11].

The analysis of X-ray diffraction patterns through the Rietveld method has been widely used for microstructure interpretation of various austenitic steels subjected to plastic deformation, among other metals and alloys[12-14]. This work characterizes by X-ray, hardness Vickers and transmission electron microscopy (TEM) analysis, the microstructure of a 17%Mn and low carbon content steel, subjected to cold rolling with 60 and 90% reduction followed by annealing at different temperatures. The X-ray patterns were analyzed using the software Materials Analysis Using Diffraction (MAUD)[15] based on Rietveld method[16]. This analysis aimed to investigate the relative

amount of the phases and microstructural parameters information such as lattice parameter, crystallite size, residual microstrain and dislocations density.

## 6.2. Material and methods

### *6.2.1. Material*

Samples of a 17%Mn and low carbon content steel were homogenized at 1100°C and hot rolled to 52% reduction in thickness. The samples were then cold rolled to 60 and 90% thickness reductions. Samples were cut from the cold rolled sheet with 10 mm wide and 15 mm long, with the thicknesses of 13 mm and 1 mm for the samples obtained after 60 and 90% cold reduction, respectively. Afterwards annealing was performed at temperatures of 500, 600, 625, 650, 675 and 700°C with 5 min soaking followed by cooling in water.

### *6.2.2. Hardness Vickers measurements*

The mechanical behaviour of the steel were assessed for all cold rolled and annealed samples by Vickers hardness measurement, using 10 kg load. A durometer Indentec was used. The samples were ground up to 1200 mesh. The softened fraction was calculated according to Equation (6.1):

$$\%Soft = \frac{HV_X - HV_{CR}}{HV_S - HV_{CR}} \times 100 \qquad (6.1),$$

where $HV_X$ is the hardness of the annealed sample, $HV_{CR}$ is the hardness of cold rolled sample and $HV_S$ is the hardness for the completely austenitic sample.

### *6.2.3. X-ray diffraction analysis*

The cold rolled and annealed at 625, 650, 675, 700°C samples were initially prepared by conventional metallographic technique for X-ray analysis. Subsequently, the samples

were subjected to electrolytic polishing. It was used a Struers Lectropol-5 at 50 V, 1.2 A, temperature of 17°C, flow rate equals 13, polishing time 90 s for a 1 $cm^2$ polished area. The electropolishing solution containing 40 mL of perchloric acid, 330 mL methanol and 330 mL of butoxyethanol was used. The polished surface corresponds to section RD (rolling direction) versus TD (transverse direction).

Analyses of X-ray diffraction on polished section were performed in a PANalytical X'Pert Pro Multipurpose Diffractometer. It was used a copper tube which provides Cu K $\alpha$ radiation ($\lambda$ = 0.154 nm) and a Ni-monochroator. Scans were performed at room temperature, 45 mA and 40 kV with 2$\theta$ ranging from 27 to 155° in the continuous scan mode with a 0.01° interval between each acquisition and 0.1 s per step.

Microstructural characterization was made from the X-ray patterns using the software Materials Analysis Using Diffraction (MAUD)[15] based on Rietveld method[16]. This software was developed to evaluate the material microstructure including its possible crystalline defect and preferred orientations[14]. MAUD has been used to characterize microstructural parameters of various materials such as lattice parameter, volume fraction of phases, crystallite size and residual microstrain. However, it is important to note that the software does not provide the standard deviation for these parameters, specially for anisotropic samples.[12,14-17,19,20].

Instrumental parameters such as correction 2$\theta$, peak asymmetry and peak-broadening parametters (U, V and W) of a standard Si sample were used as refinement parameters in the software following the Lutterotti *et al.* procedure[15]. The crystallite size (D) and microstrain $\langle \varepsilon^2 \rangle^{1/2}$ were obtained from a size-strain analysis by Popa model[18].

The microstrain and crystallite size are closely related to the width of diffraction peak. The microstrain is related to changes in lattice parameter and influences the crystallite size. When a material has nanometer particles it is possible to occur diffracted intensities in 2$\theta$ values slightly higher or lower than the ideal Brag angle, thus broadening the peaks. This is due to the lower number of planes which diffract the X-rays, allowing diffraction for wavelengths slightly higher and lower than the real one,

"λ". For this reason the average crystallite size is calculated, which is a function of: form factor, "K"; wavelength "λ"; full-width at half maximum (FWHM), "B", which is measured in radians at the intensity equal to half the maximum intensity; full-width at half maximum (FWHM) for a standard sample, "V", which does not present peak broadening[21].

$$\langle \varepsilon^2 \rangle^{1/2} = \frac{K\lambda}{(B - V)\cos\theta} \tag{6.2}$$

The Moment Pole Stress model[22] implemented in MAUD was also used to fit the variations of peak positions with azimuth once this samples were submitted to high reductions in cold rolling. Elastic constants for austenite[23] and α' martensite[24] were used in this model.

The average values of dislocation density "ρ" of the samples which were subjected to different cold reductions and annealing was also determined following the procedure of Williamnson and Smallman[25]. The value of "ρ" was calculated by Equation (6.3):

$$\rho = \frac{3\sqrt{2\pi}\langle \varepsilon^2 \rangle^{1/2}}{Db} \tag{6.3},$$

where "$\langle \varepsilon^2 \rangle^{1/2}$" is the microstrain, "D" is the crystallite size and "b" is the Burgers vector, as shown:

$$b = \frac{a}{2}\sqrt{h^2 + k^2 + l^2} \tag{6.4}.$$

Here "a" is the lattice parameter and "h, k, l" are the Müller indices for the most compact plane. It was assumed that $b = \frac{a\sqrt{2}}{2}$ for austenite, fcc (110), and $b = \frac{a\sqrt{3}}{2}$ for α' martensite, assuming it as bcc structure (111).

The volume fraction of each phase was also estimated in MAUD by evaluating the weight fraction[26] and the density of each phase[27].

*6.2.4. Transmission Electron Microscopy analysis*

Microstructural characterization was also carried by TEM in the samples that were just cold rolled with 60% thickness reduction and 625°C annealed condition. It was used a JEOL JEM-2010 microscopy. The samples were prepared by punching out 3 mm discs and mechanical to 1 mm by grinding with a 1200 mesh paper. After that the samples were electropolished using an electrolyte containing 95% methanol and 5% percloric acid to obtain thinning necessary for electron transparency. It was carried out in a Struers TenuPol at -30°C, 30 V and 150 mA.

## 6.3. Results and discussion

The results obtained by the Vickers hardness measurements are presented below (Fig. 6.1). According to Figure 6.1(a) it can be seen that from 600°C annealing temperature there is a strong reduction in hardness values and that similar hardness values occurs for the two cold rolling conditions, even for the highest values temperature regardless of the amount of cold reduction. This fact is due to the reversion of $\alpha$' martensite, generated by cold deformation, in austenite. Despite it was expected to obtain a refined microstructure for the samples with 90% reduction after annealing, due to the greater amount of crystal defects generated from deformation, it is not observe higher hardness values above 625°C when compared to the 60% reduction samples. This can be associated to the higher $\alpha$' martensite amount reversing in austenite in this condition when compared to 60% cold reduction at the same temperature. These affirmations will be further supported in this work by X-ray diffraction analysis. In addition, according to Figure 6.1 (b), we observe that the 650°C samples provide approximately 50% of the softened microstructure for both conditions of cold rolling.

The accuracy of the results obtained by Rietveld analysis using the MAUD is indicated by the quality factors values of refinement, such as GOF (goodness of fit), $R_w$ (weighed residual error) and $R_{exp}$ (expected error). The GOF is obtained dividing $R_w$ by $R_{exp}$. Note that the GOF values are close to one and that the other parameters show low values, as presented in Table VI.1.

Table VI.2 shows the lattice parameters obtained for austenite and α' martensite for each condition of cold rolling and annealing. Note that there were no significant changes in these values for each phase as a function of cold reduction or annealing temperature as expected.

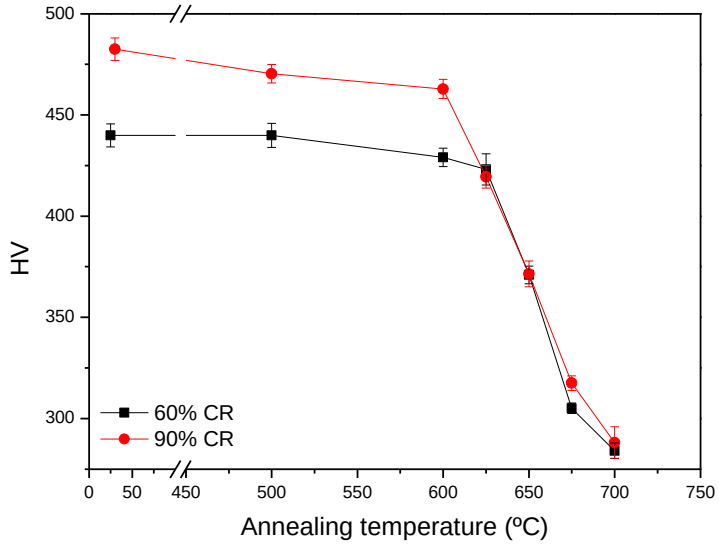


(a)

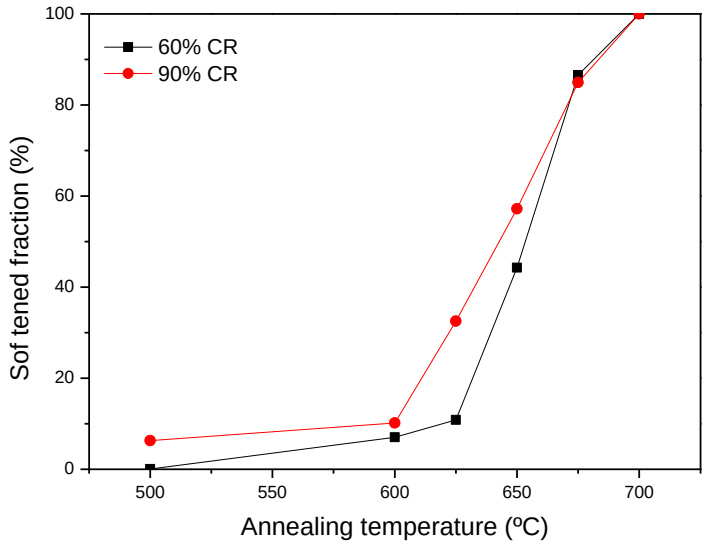


(b)

Figure 6.1. (a) Hardness Vickers and softening curve (b) for 60 and 90% cold rolling reductions as a function of annealing temperature.

Table VI.1. Refinement parameters obtained by Rietveld refinement using MAUD.

| Cold rolling reduction (%) | Annealing temperature (°C) | GOF | $R_w$ (%) | $R_{exp}$ (%) |
|---|---|---|---|---|
| 60 | - | 1.12 | 14.4 | 12.8 |
| | 625 | 1.27 | 18.0 | 14.2 |
| | 650 | 1.25 | 16.7 | 13.4 |
| | 675 | 1.15 | 16.4 | 14.2 |
| | 700 | 1.19 | 17.2 | 14.4 |
| 90 | - | 1.24 | 15.0 | 12.1 |
| | 625 | 1.26 | 17.0 | 13.5 |
| | 650 | 1.21 | 16.3 | 13.5 |
| | 675 | 1.16 | 16.1 | 13.9 |
| | 700 | 1.19 | 16.6 | 14.0 |

Table VI.2. Lattice parameters of the austenite and α' martensite for each cold rolling and annealing condition.

| Cold rolling reduction (%) | Annealing temperature (°C) | Lattice parameter for austenite (Å) | Lattice parameter for α-Martensite (Å) |
|---|---|---|---|
| 60 | - | 3.6022 | 2.8823 |
| | 625 | 3.6022 | 2.8761 |
| | 650 | 3.6009 | 2.8765 |
| | 675 | 3.6009 | - |
| | 700 | 3.6006 | - |
| 90 | - | - | 2.8871 |
| | 625 | 3.6009 | 2.8760 |
| | 650 | 3.6005 | 2.8800 |
| | 675 | 3.5999 | - |
| | 700 | 3.6000 | - |

Figure 6.2 (a,b) shows the diffraction pattern obtained for the cold rolled samples with 60 and 90% reduction and annealed. All the Bragg reflections presented in the X-ray spectra were indexed. In accordance with the Rietveld refinement it was observed that the amount of austenite increases at the expense of α' martensite as the annealing temperature increases. At 675°C all α' martensite from deformation have reversed completely in austenite for both cold rolling conditions, as shown in Figure 6.3. However, it is noted that at both 625°C and 650°C temperatures the reversed austenite amount is higher for the samples which were subjected to 90% cold reduction. This indicates that the reversion occurs more rapidly for samples that have greater energy stored in the deformation, which acts as the driving force for the reverse transformation from α' martensite into austenite via diffusion process as nucleation and growth. High reductions in cold deformation provide higher crystalline defects density. Thus, the highly deformed martensite will provide intense generation of sites for austenite nucleation and will favor the formation of an austenitic structure with finer grains after annealing. However, according to the literature[9,28,29], the reduction amount in cold rolling has no influence on the α' martensite reversion to austenite if it occurs by shear mechanism.

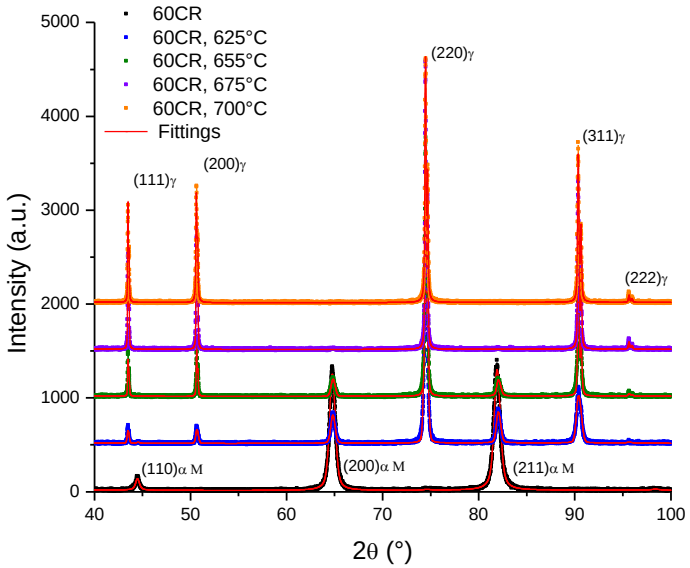


(a)

Figure 6.2. X-ray diffraction patterns obtained and their MAUD fittings for samples cold rolled to 60 (a) and 90% (b) cold reduction and annealed at different temperatures.

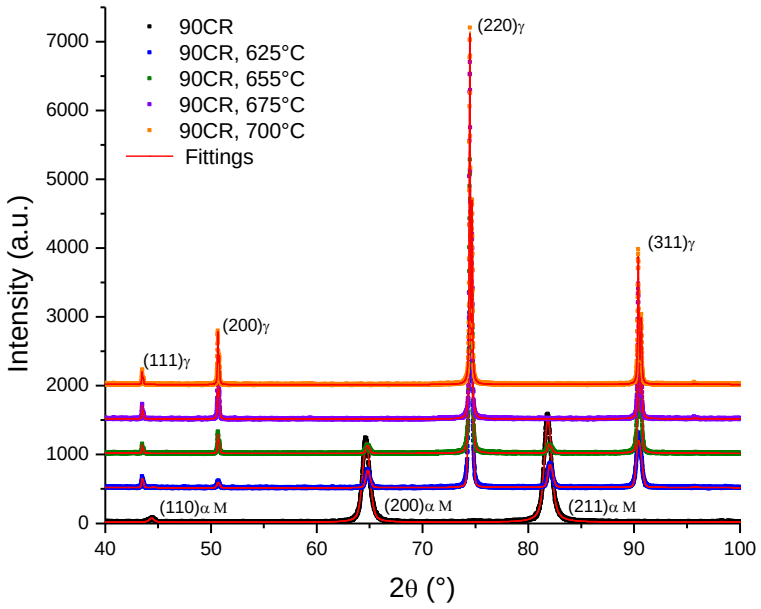


(b)

(cont.) Figure 6.2. X-ray diffraction patterns obtained and their MAUD fittings for samples cold rolled to 60 (a) and 90% (b) cold reduction and annealed at different temperatures.

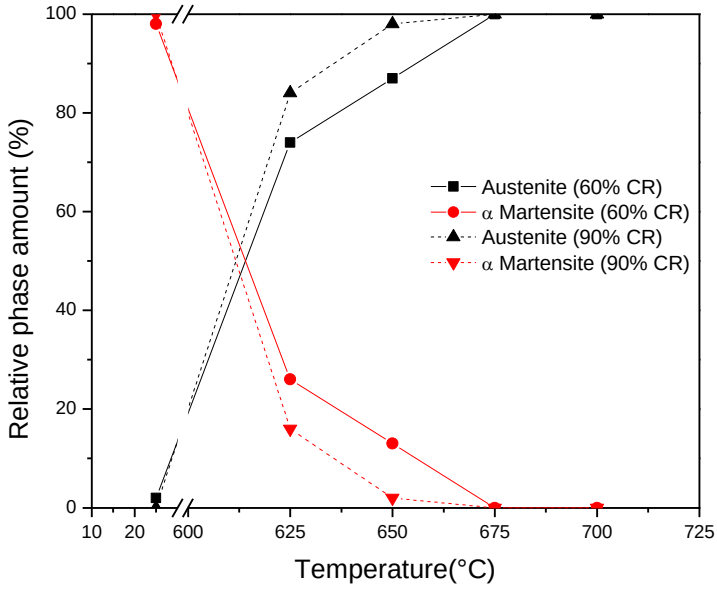


Figure 6.3. Relative amount of phases for samples cold rolled with 60 and 90% reduction and annealed at different temperatures.

The crystallite size was estimated for the two phases present in each thermomechanical processing condition. It is observed in Figures 6.4(a,b) that the α' martensite crystallite sizes are anisotropic and that they are smaller when compared to austenite. In addition they increase as the annealing continues. Despite this value initially be lower for the sample that was more deformed, there are no significant differences when comparing the two cold rolling conditions in each annealing temperature.

Likewise, it was noted through Figures 6.4(c,d) that the crystallite size for austenite clearly shows anisotropic values along different [*hkl*] directions. Note that there is no austenite in the sample just 90% cold rolled (Fig. 6.4 (d)). The crystallite size of austenite increases as the annealing temperature arises, as expected, for both cold rolling reductions. It is also noted that the crystallite size is slightly higher for samples which were initially cold rolled to 60% thickness reduction. As previously mentioned, the α' martensite subjected to a more intense deformation provides a finer austenitic structure after annealing, since the nucleation rate is higher, thus justifying this difference in crystallite size values between the two cold reductions. Furthermore, the initial amount of α' martensite amount that will reverse to austenite, either by diffusion or shear, is lower for the samples submitted to 60% cold reduction compared to 90% samples as previously indicated by the Vickers hardness measurements (Fig. 6.1(a,b)).

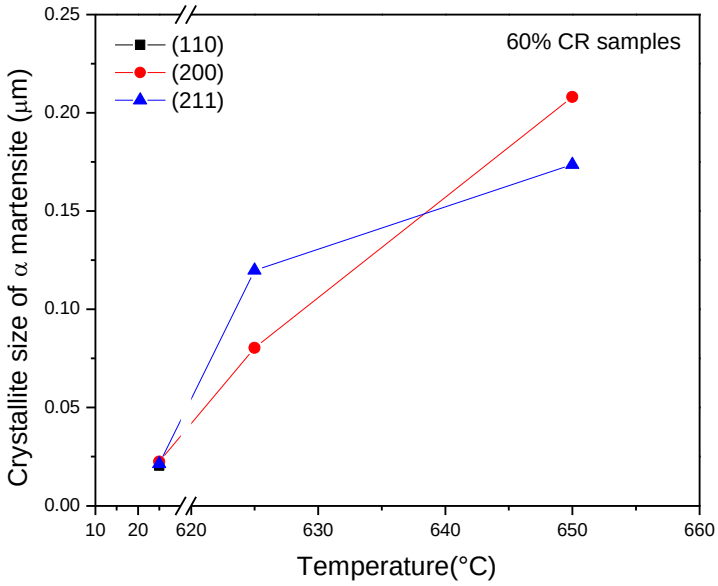


(a)

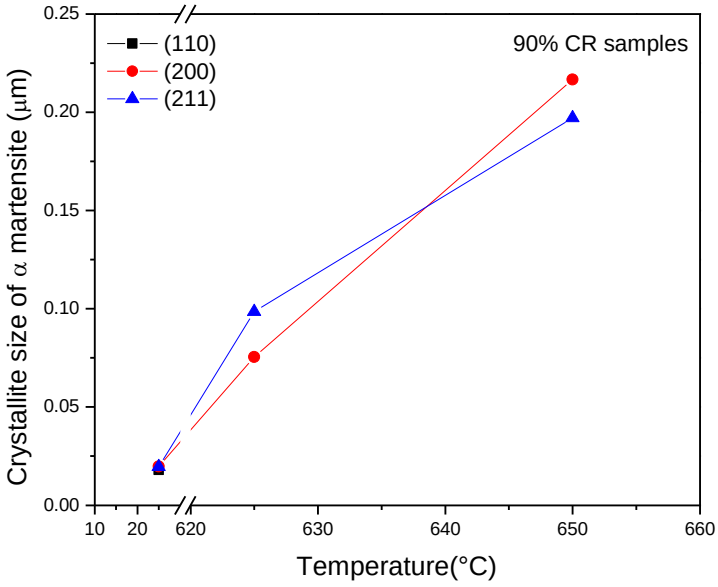


(b)

Figure 6.4. Crystallite size for: α' martensite as function of annealing temperatures for the samples initially cold rolled with 60 (a) and 90% (b) thickness reduction; austenite as function of annealing temperatures for the samples initially cold rolled with 60 (c) and 90% (d) thickness reduction.

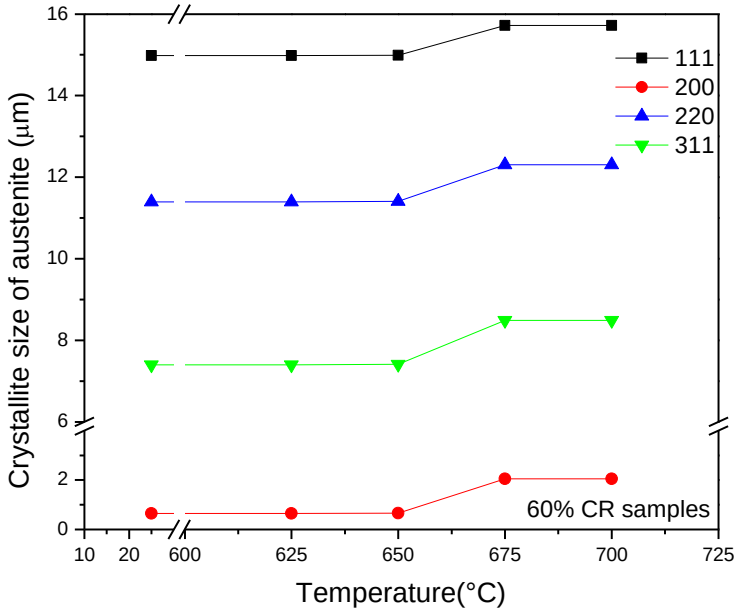


(c)

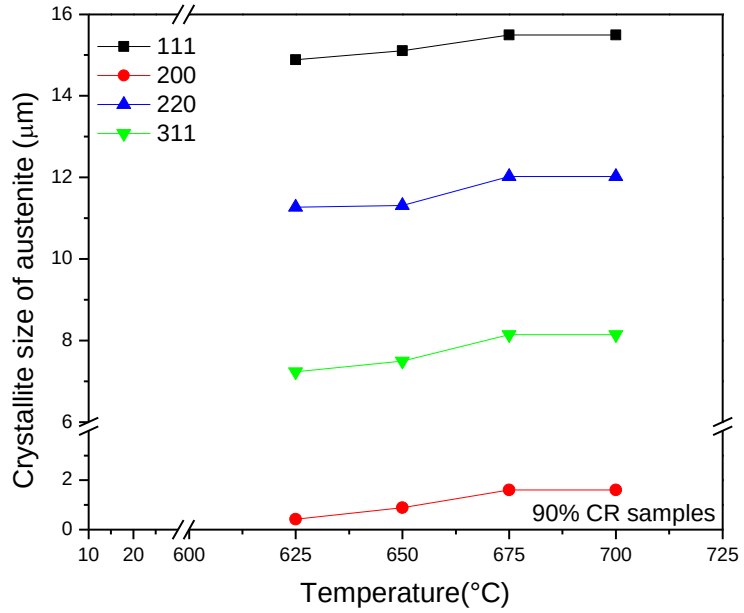


(d)

(cont.) Figure 6.4. Crystallite size for: α' martensite as function of annealing temperatures for the samples initially cold rolled with 60 (a) and 90% (b) thickness reduction; austenite as function of annealing temperatures for the samples initially cold rolled with 60 (c) and 90% (d) thickness reduction.

The microstrain values for α' martensite obtained by MAUD fitting for 60 and 90% cold rolled and annealed samples are shown in Figures 6.5(a,b). It was found that these values decrease as the annealing proceeds for both conditions of cold rolling, as expected. However this decrease is more pronounced for 90% reduction, once these samples have greater driving force for austenite reversion by diffusion.

Figures 6.5(c,d) show the microstrain obtained for austenite. Note that there is no austenite in the sample just 90% cold rolled (Fig. 6.5 (d)). It was shown that these values decrease as the annealing temperature increases also. However, it is noted that the microstrain is still relatively high for this new austenite formed. This shows that the austenite formed is not completely free of microstructural defects and deformation, which indicates the presence of the shear as reversion mechanism beyond the diffusion process. This fact is in agreement with previous studies presented for austenitic stainless alloys[9,28,29].

The dislocation densities present in the α' martensite, calculated based on crystallite size and microstrain data obtained by MAUD fitting, are presented in Figures 6.6(a,b). These values are clearly greater the higher is the reduction imposed by cold rolling. In addition, they are higher for samples initially more deformed and annealed. As expected these values also decrease due to the increase of the annealing temperature for both cold rolling conditions. However, the dislocation density is significantly lower for samples which were cold rolled with 90% reduction and then annealed at 625 and 650°C compared to those that were reduced by 60% and were annealed at the same temperatures. This also indicates that greater stored energy due to the higher deformation amount acts as the driving force for α' martensite reversion in austenite by diffusion[28].

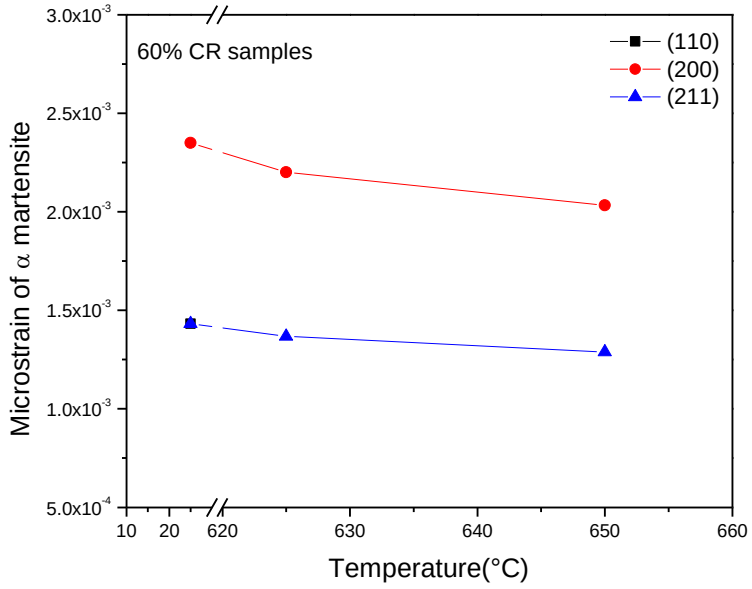


(a)

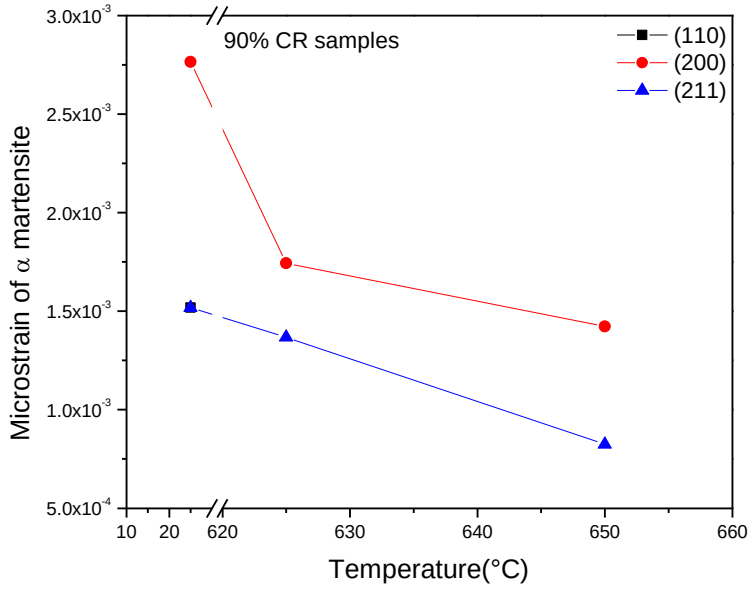


(b)

Figure 6.4. Crystallite size for: α' martensite as function of annealing temperatures for the samples initially cold rolled with 60 (a) and 90% (b) thickness reduction; austenite as function of annealing temperatures for the samples initially cold rolled with 60 (c) and 90% (d) thickness reduction.

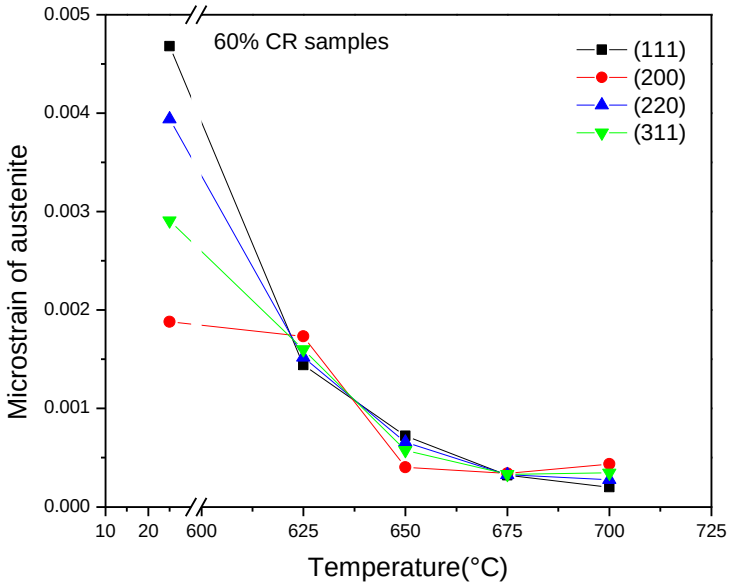


(c)

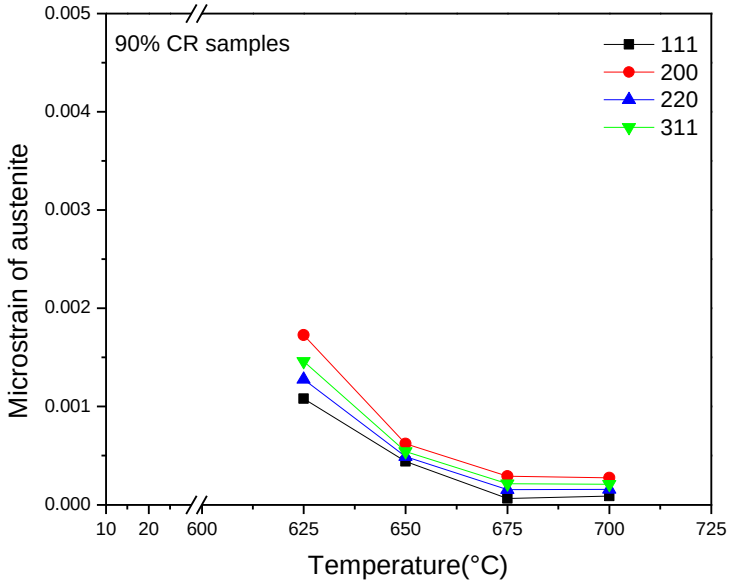


(d)

(cont.) Figure 6.5. Microstrain values for: α' martensite as a function of annealing temperature for samples initially cold rolled to 60 (a) and 90% (b) thickness reduction; austenite as a function of annealing temperature for samples initially cold rolled to 60 (c) and 90% (d) thickness reduction.

The dislocation density in austenite is presented in (Fig. 6.6(c,d)). Note that there is no austenite in the sample just 90% cold rolled (Fig. 6.6 (d)). Once the annealing temperature increases the dislocation density decreases as expected, because of the movement of high angle grain boundaries (HAGB) during the grain growth of austenite[7,28]. Furthermore, when annealing is performed it is noted that up to a temperature of 650°C the dislocation density at this stage is greater to the 90% cold rolled samples. Above this temperature they are lower when compared to samples which were cold rolled with 60% thickness reduction. This means that the structure recovery process is more effective and faster at higher temperatures when it has greater energy stored in the deformation process. This result is in agreement with the previous softening curve obtained by hardness Vickers analysis showed in Figure 6.1(b). These austenite density of dislocations values after annealing for both cold rolling conditions are reasonable compared to a full annealed austenitic stainless steel[30] which shows a magnitude of ~$10^{11}$ $m^{-2}$. The results presented here for austenite in the TRIP/TWIP steel are higher (~$10^{12}m^{-2}$) compared to the alloy mentioned before. However, the austenite in this TRIP/TWIP steel comes from reversion and one of these mechanisms is shearing which does not produce a microstructure free of defects according to the literature[28]. This result corroborates the previous microstrain analysis in austenite after annealing (Fig. 6.5(c,d)) and reaffirm the great importance of reversion by shearing in this work.

It was also possible to identify the presence of shearing as well as diffusion as reversion mechanism from α' martensite to austenite through the different austenite morphologies detected by TEM. Figure 6.7 shows α' martensite laths containing high dislocation density (a) in a 60% cold rolled sample and the austenite formed during the annealing at 625°C after the same reduction (Fig. 6.7(b,c)). It is noted that the austenite showed in Figure 6.7 (b) is practically clear of defects as dislocations which suggest diffusion as a reversion mechanism. However, the austenite showed in Figure 6.7(c) has clearly a higher dislocation density according to the contrast observed as well as the presence of twins. Therefore, this is an indication that the shearing acted as reversion mechanism in those grains. These results corroborates the previous statements about the existence of both mechanisms in this TRIP/TWIP steel and it is in accordance to literature[28] which suggest the existence of the same mechanisms in a stainless austenitic steel.

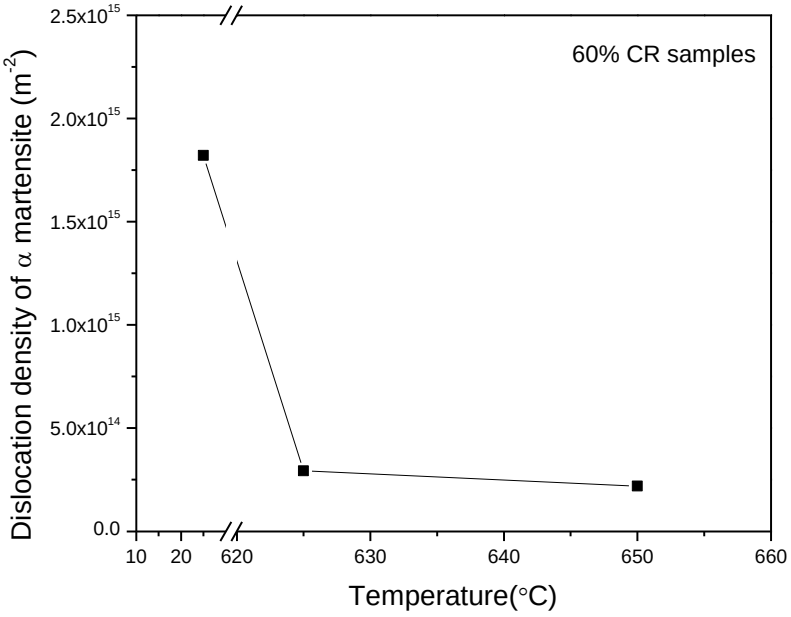


(a)

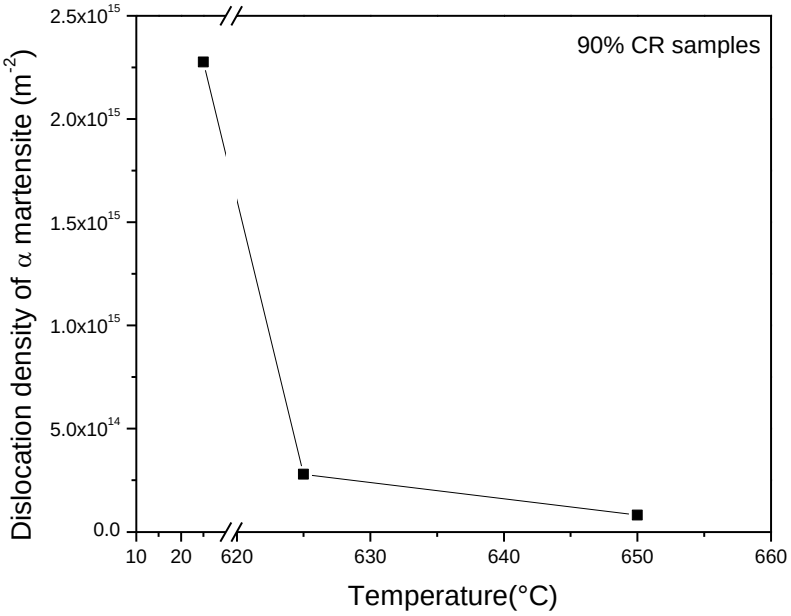


(b)

Figure 6.6. Dislocation density in: α' martensite as a function of annealing temperature for samples initially cold rolled to 60 (a) and 90% (b) thickness reduction; austenite as a function of annealing temperature for samples initially cold rolled to 60 (c) and 90% (d) thickness reduction.

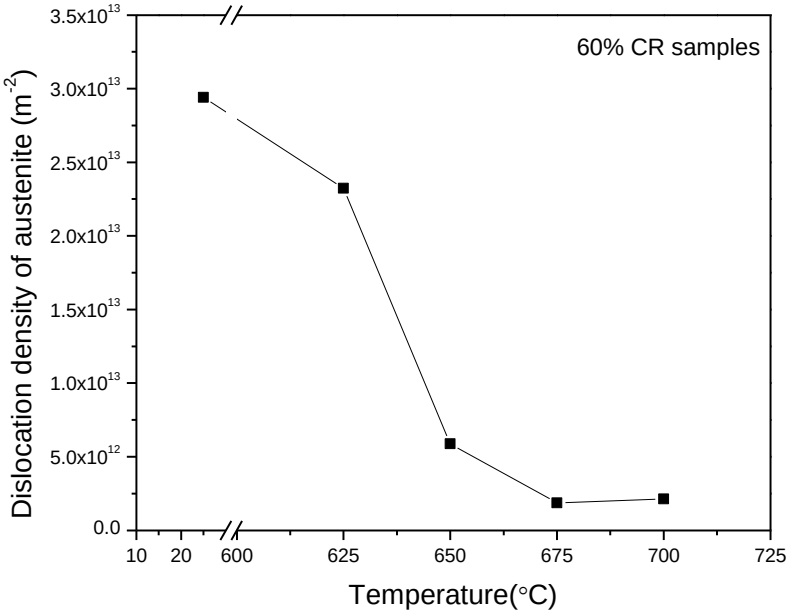


(c)

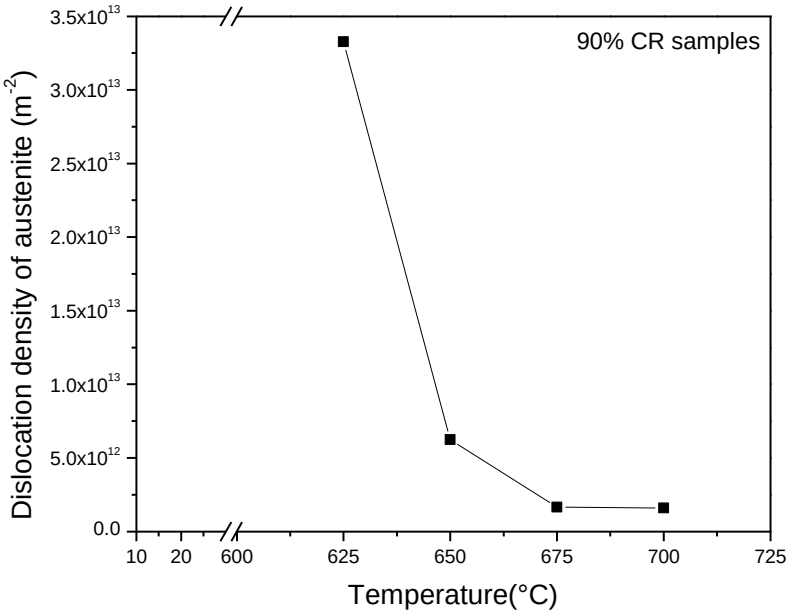


(d)

(cont.) Figure 6.6. Dislocation density in: α' martensite as a function of annealing temperature for samples initially cold rolled to 60 (a) and 90% (b) thickness reduction; austenite as a function of annealing temperature for samples initially cold rolled to 60 (c) and 90% (d) thickness reduction.

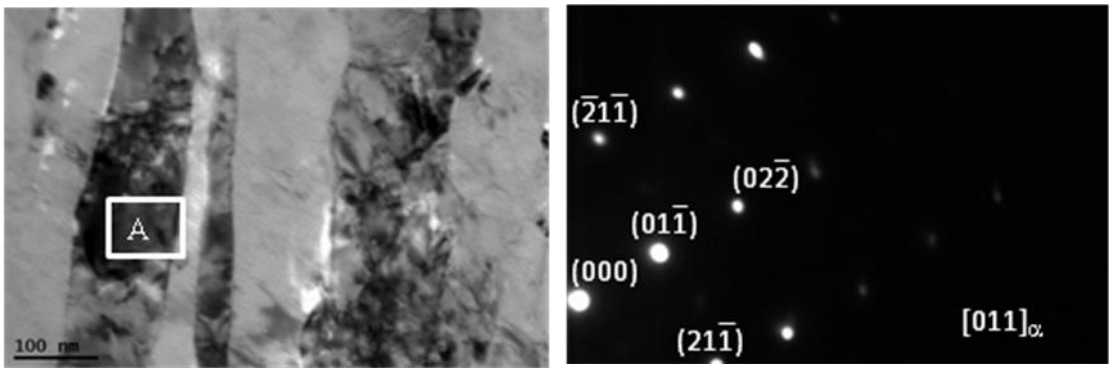


(a)

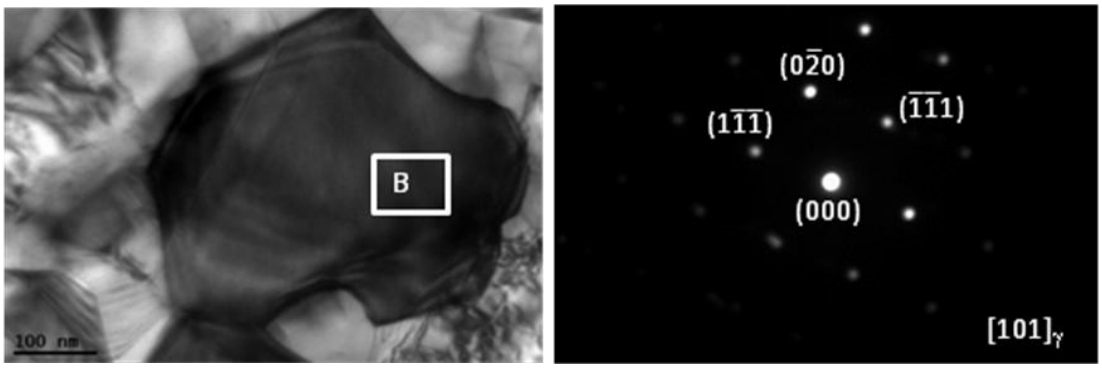


(b)

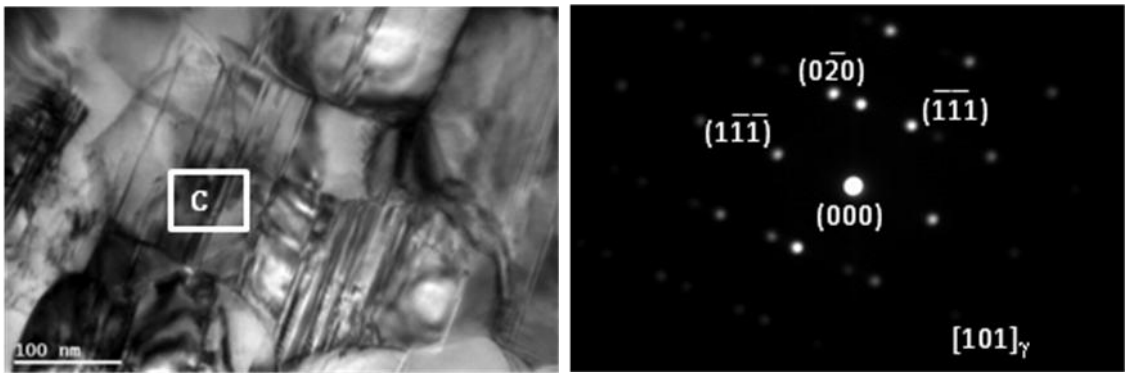


(c)

Figure 6.7. Bright field TEM micrographs with their corresponding diffraction pattern of: (a) α' martensite in 60% cold rolled; 60% cold rolled and 625°C annealed sample showing low (b) and high (c) density of dislocations in austenite.

## 6.4. Conclusions

- The hardness Vickers values and the crystallite size analysis by MAUD have shown that although the larger deformation (90%) can produces a finer

austenitic microstructure, the amount of α' martensite is higher initially for this condition, causing faster reversion to austenite and explaining the similar values of hardness compared to annealed samples after 60% deformation.

- The microstrain results from MAUD indicated that α' martensite to austenite reversion occurs by shearing together with diffusion mechanism.
- The calculation of dislocation density from MAUD results of crystallite size and microstrain indicates that austenite reversion is more effective and faster at higher temperatures when it has greater stored energy from deformation process.
- It was shown from dislocation density based on MAUD results and by TEM images that dislocation density is still high, even for samples after annealing, proven that the presence of the shear reversion mechanism of austenite is noteworthy.

**Acknowledgements**

Sara S. F. de Dafé acknowledges the scholarship provided by CAPES Foundation, Ministry of Education of Brazil, process number 0804-12-6 and the University of Wollongong, Australia for providing the laboratorial support.

**References**

1. DE COOMAN, B. C., CHIN, G. K., KIM, J. K. High Mn TWIP steels for automotive applications, *New Applications in Trends and Developments in Automotive Engineering*, ed. by I. Lipovic, Intech Publishers, Austria, p. 101-128, 2011.
2. LU Y., HUTCHINSON, B., MOLODOV, D. A., GOTTSTEIN, G. Effect of deformation and annealing on the formation and reversion of ε-martensite in an Fe–Mn–C alloy, *Acta Materialia*, v. 58, p. 3079-3090, 2010.
3. TAKAKI, S., NAKATSU, H., TOKUNAGA, Y. Effects of austenite grain size on ε martensitic transformation in Fe-15mass%Mn alloy, *Materials Transactions JIM*, v. 34, p.489-495, 1993.

4. DINI, G., NAJAFIZADEH, A., MONIR-VAGHEFI, S.M., UEJI, R. Grain size effect on the martensite formation in a high-manganese TWIP steel by the Rietveld method, *Materials Science and Technology*, v. 26, p. 181-186, 2010.
5. SAHU, P., HAMADA, A.S., GHOSH, R.N., KARJALAINEN, V. X-ray diffraction study on cooling-rate-induced $\gamma_{fcc} \rightarrow \varepsilon_{hcp}$ martensitic transformation in cast-homogenized Fe-26Mn-0.14C austenitic steel, *Metallurgical Materials Transactions A*, v. 38A, p. 2007-1991, 2000.
6. HAMADA, A.S., SAHU, P., CHOWDHURY, S. G., KARJALAINEN, L.P., LEVOSKA , J., OITTINEN, T. Kinetics of the α' martensitic transformation in fine-grained Fe-26Mn-0.14C austenitic steel, *Metallurgical Materials Transactions A*, v. 39A, p. 462-465, 2008.
7. SAHU, P., HAMADA, A. S., CHOWDHURY, S. G., KARJALAINEN, L. P. Structure and microstructure evolution during martensitic transformation in wrought Fe–26Mn–0.14C austenitic steel: an effect of cooling rate, *Journal of Applied Crystallography*, v. 40, p. 354-361, 2007.
8. DING, H.; DING, H.; SONG, D.; TANG, Z.; YANG, P. Strain hardening behavior of a TRIP/TWIP steel with 18.8%Mn, *Materials Science and Engineering A*, v. 528, p. 868-873, 2011.
9. TOMIMURA, K., TAKAKI, S., TOKUNAGA, Y. Reversion mechanism from deformation induced martensite to austenite in metastable austenitic stainless steels, *ISIJ International*, v. 31, p. 1431–1437, 1991.
10. MIRZADEH, H.; NAJAFIZADEH, A. Modeling the reversion of martensite in the cold worked AISI 304 stainless steel by artificial neural networks, *Materials and Design*, v. 30, p. 570–573, 2009.
11. PADILHA, A. F.; PLAUT, R. L.; RIOS, P. R. Annealing of cold-worked austenitic stainless steels, *ISIJ International*, v. 43, p. 135-143, 2003.
12. PAL, H.; CHANDA, A.; DE, M. Characterisation of microstructure of isothermal martensite in Fe-23Ni-3.8Mn by Rietveld Method, *Journal of Alloys and Compounds*, v. 278, p. 209-215, 1998.
13. SAHU, P.; HAMADA, A. S.; SAHU, T.; PUUSTINEN, T.; OITTINEN, T.; KARJALAINEN, L. P. Martensitic transformation during cold rolling deformation

of an austenitic Fe-26Mn-0.14C alloy, *Metallurgical and Materials Transactions A*, v. 43, p. 47-55, 2011.

14. CHANDA, A.; DE, M. X-ray characterization of the microstructure of α-CuTi alloys by Rietveld's Method, *Journal of Alloys and Compounds*, v. 313, p. 104-114, 2000.
15. L. LUTTEROTTI, MAUD, Ver. 2.14, www.ing.unitn.it/~maud/.
16. RIETVELD, H. M. A Profile Refinement Method for Nuclear and Magnetic Structures, *Journal of Applied Crystallography*, v. 2, p. 65-71, 1969.
17. SAHU, P.; DE, M.; KAJIWARA, S. Microstructural characterization of Fe-Mn-C martensites athermally transformed at low temperature by Rietveld method, *Materials Science and Engineering A*, v. 333, p. 10-23, 2002.
18. POPA, N. C. The (*hkl*) Dependence of Diffraction-Line Broadening Caused by Strain and Size for all Laue Groups in Rietveld Refinement, *Journal of Applied Crystallography*, v. 31, p. 176-180, 1998.
19. SMALLMAN, R. E.; WESTMACOTT, K. H. Stacking faults in face-centred cubic metals and alloys, *Philosophical Magazine*, v. 2, n. 17, p 669–683, 1957.
20. DINI, G.; UEJI, R.; NAJAFIZADEH, A.; MONIR-VAGHEFI, S. M. Flow stress analysis of TWIP steel via the XRD measurement of dislocation density, *Materials Science and Engineering A*, v. 527, p. 2759-2763, 2010.
21. CULLITY, B. D., STOCK, S. R. Elements of X-ray diffraction. New Jersey: Prentice Hall, 2001.
22. MATTHIES, S., PRIESMEYERA, H. G., DAYMOND, M. R. On the diffractive determination of single-crystal elastic constants using polycrystalline samples, *Journal of Applied Crystallography*, v. 34, p. 585-601, 2001.
23. REID, C. N. Deformation geometry for materials scientists. Pergamon Press; 1st edition, 211 p., 1973.
24. KIM, S. A., JOHNSON, W. L. Elastic constants and internal friction of martensitic steel, ferritic-pearlitic steel, and α-iron, *Materials Science and Engineering A*, v. 452–453, p. 633-639, 2007.
25. WILLIAMSON, G. K., SMALLMAN R. E. Dislocation densities in some annealed and cold-worked metals from measurements on the X-ray Debye-Scherrer spectrum, *Philosophical Magazine*, v. 1, Issue 1, 1956.

26. HILL, R. J., HOWARD, C. J. Quantitative phase analysis from neutron powder diffraction data using the Rietveld method, *Journal of Applied Crystallography*, v. 20, p. 467-474, 1987.
27. BISH, D. L., HOWARD, S. A. Quantitative phase analysis using the Rietveld method, *Journal of Applied Crystallography*, v. 21, p. 86-91, 1988.
28. KNUTSSON, A., HEDSTRÖM P., ODÉN, M. Reverse martensitic transformation and resulting microstructure in a cold rolled metastable austenitic stainless steel, *Steel Research International*, v. 79, n. 6, p. 433-439, 2008.
29. TOMIMURA, K., TAKAKI, S., TANIMOTO, S., TOKUNAGA, Y. Optimal chemical composition in Fe-Cr-Ni alloys for ultra grain refining by reversion from deformation induced martensite, *ISIJ International*, v. 31, n. 7, p. 721–727, 1991.
30. MURUGESAN, S., KUPPUSAMI, P., MOHANDAS, E., VIJAYALAKSHMI, M. X-ray diffraction Rietveld analysis of cold worked austenitic stainless steel, *Materials Letters*, v. 67, p. 173-176, 2012.

# CHAPTER 7: Investigation of microstructure and texture evolution by TEM and EBSB in a 17%Mn TRIP/TWIP steel with low C as function of cold reduction and annealing

**Abstract:**

High manganese steels exhibit good plasticity under deformation due to TWIP (Twinning Induced Plasticity) effect, or due to martensitic transformation, known as the TRIP (Transformation Induced plasticity) effect. In these alloys when the Mn content is between 15% and 25% both TRIP and TWIP effects act as deformation mechanisms. In the present study microstructural and texture evolution were evaluated by EBSD and TEM techniques in a 17%Mn and low carbon content steel, subjected to cold rolling with 60 and 90% thickness reduction followed by annealing at different temperatures. It was verified that the microstructure after austenite reversion is more refined for samples which were initially subjected to higher cold reduction. In addition, the nucleation and growing process are faster for the samples initially 90% cold rolled, due to the greater stored energy during deformation. The transformation induced by deformation occurs in two steps $\gamma \rightarrow \varepsilon \rightarrow \alpha'$ and $\alpha'$ martensite tends to be the major phase as deformation increases. It was also showed that $\alpha'$ and $\varepsilon$ martensite reversion into austenite completes itself at 700°C regardless of the deformation amount and, after annealing at higher temperatures, $\varepsilon$ and $\alpha'$ martensites forms again during quenching. For the steel in study, Kurdjumov-Sachs is the orientation relationship between austenite and $\alpha$’ martensite while for $\varepsilon$ martensite and austenite it is Shoji-Nishiyama. The $\alpha$’ martensite have different dislocation density and irregular shape in the deformed material while in the annealed sample showed many annealing twins by TEM. The transformation texture analysis showed that austenite reversion occurs without simultaneous recrystallization. As reversion proceeds, Goss component tends to be replaced by Brass in austenite. This fact is beneficial because it becomes {332}<113> in $\alpha$’ martensite after phase transformation and could promote good formability as well as high strength and toughness.

**Keywords:** High manganese steel, texture, cold rolling, annealing, austenite reversion

## 7.1. Introduction

The search for steels that combine high mechanical strength, good formability and low density is a constant demand in automotive industry. It is in this context that arise steels containing high levels of Mn, Si and Al, which exhibit adequate plasticity when subjected to deformation due to twinning, known as effect TWIP (Twinning Induced Plasticity), or martensitic transformation, called TRIP effect (Transformation Induced plasticity)[1,2].

The generation of ultra-fine grain size is possible through reverse transformation of α' martensite into austenite and it has aroused the interest in martensitic phase transformation for metastable austenitic steels[3,4]. This refinement of the final microstructure through martensite reversion into austenite usually induces a good formability without strength loss[5,6].

Several techniques, such as XRD (X-Ray Diffraction), EBSD (Electron Backscatter Diffraction) and TEM (Transmission Electron Microscopy), have been used to investigate the austenite reversion into martensite. These techniques are complementary to each other in these studies, since, for example, there are difficulties in indexing twins in reversed austenite via EBSD, because such crystal defects generally are only tens of nanometers thick[7-9]. In addition, conventional TEM is not simple and convenient for the study of crystallographic orientation relationship[10].

Mechanical properties of steels subjected to rolling and annealing are determined by the nature and intensity of the transformation texture, once the plastic anisotropy of a material is greatly dependent on the texture. In this regard, investigations on the formation of the transformation texture during cold rolling and subsequent recrystallization has been performed[11].

It is well known for steels that if the matrix phase (austenite) has a determined crystallographic texture, the material after phase transformartion (ferrite, martensite, acicular ferrite or bainite) will also present a texture which is related with the previous

texture through precise rules[11]. These orientation relationships (OR) are necessary to evaluate the evolution of texture between matrix and product phases and describe the phases transformation. These are the OR proposed by Bain, Kurdjumov-Sachs, Nishiyama and Wassermann, and Greninger and Troiano between bcc and fcc crystalline structures[12]. Studies on metastable austenitic steels have indicated that the Kurdjumov-Sachs OR is associated with the transformation from ferrite or α' martensite into austenite, and vice versa, where $\{111\}_{\gamma}//\{011\}_{\alpha'}$ and $<1\bar{1}0>_{\gamma}//<1\bar{1}1>_{\alpha'}$[13,14].

Thus, as there is a limited amount of publications concerning the reversion of α' martensite and evolution of the microstructure and texture processing for these new TRIP/TWIP steels, more studies are needed to establish how the reversion mechanism and the transformation texture can control the final microstructure. In this work microstructural characterization and texture evolution were evaluated by EBSD and TEM techniques in a 17%Mn and low carbon content steel, subjected to cold rolling with 60 and 90% reduction followed by annealing at different temperatures.

## 7.2. Material and methods

### *7.2.1. Material*

Samples of a steel with low carbon content and high contents of manganese, silicon and aluminum, were homogenized at 1100°C and hot rolled with 52% reduction in thickness. The samples were then cold rolled (CR) to 60 and 90% thickness reductions. The samples with 10 mm wide and 15 mm length were cut from the cold rolled plates, with thicknesses of 13 mm and 1 mm for 60 and 90%, respectively. After that they were annealed at 625, 650, 675, 700, 800, and 1000°C with 5 min soaking. After annealing the samples were water cooled.

### *7.2.2. Methods*

EBSD analyzes were carried out in the center of the normal direction (ND) - rolling direction (RD) section. The samples were ground up to 1200 mesh, polished with 6 and

1 μm diamond suspension in a Struers Rotopol-1 polishing machine with 150 rpm. Subsequently, the samples were subjected to electrolytic polishing in a Struers-5 Lectropol with of 50 V, 1.2 A at 17°C, flow rate equals to 13 and 90 s polishing time in a $1cm^2$ polished area. The electrolytic solution used contains 40 mL perchloric acid, 330 mL methanol and 330 mL butoxyethanol. After electropolishing, the samples were etched with ferric chloride acid which is composed by 5% ferric chloride, 25% hydrochloric acid and 70% water.

Microstructural characterization, phase identification and crystallographic texture analysis were evaluated by Electron Backscatter Diffraction (EBSD) in a scanning electron microscope type Field Emission Gun (FEG) JEOL JSM-700 1F fitted with a Nordlys-II(S) camera and the Oxford Instruments AZtec acquisition software suite and operating at 15 keV and working distance (WD) equal to 12 mm. Texture analysis by EBSD was carried out with the Channel 5 software. The magnification, the step sizes and indexing after images cleaning and pre-treatment for each sample are presented in Table VII.1. It is known that the presence of complex microstructures and with more than one phase or containing a high density of crystalline defects causes improper identification of diffraction patterns and indexing errors by EBSD[15]. Because of that, the indexing is lower for more deformed samples.

The maps were obtained adopting at least three pixels to define a grain or subgrain. Misorientations smaller than 2° were disregarded. Low Angle Grain Boundaries (LAGBs) were defined as misorientations from 2 to 15° and High Angle Boundaries (HAGBs) from 15 to 57.5°. It is assumed that the Twin Boundaries (TBs) of first order (Σ3) are those having misorientation of 60°<111> whereas the second order (Σ9) exhibit 38.9°<101>. It was considered as Total High Angle Grain Boundaries (THAGBs) the addition of the area fraction of HAGBs and twin boundaries (TBs). The misorientation tolerance from the exact relation-axis angle (Δθ) was defined according to Palumbo-Aust criterion[16] -$\Delta\theta \leq 15° \Sigma^{-5/6}$ and tolerance limits for Σ3 and Σ9 are equal to 6 and 2.4°, respectively.

Table VII.1. Identification of samples and parameters used for EBDS maps acquisition as well as the indexing obtained.

| Thickness cold reduction (%) | Annealing temperature (°C) | Magnification | Step Size (μm) | Indexing (%) |
|---|---|---|---|---|
| 60 | - | 2300x | 0,07 | 52,80 |
| | 625 | 2000x | 0,05 | 56,10 |
| | 650 | | | 98,90 |
| | 675 | | | 99,64 |
| | 700 | | | 99,89 |
| | 800 | 1000x | 0,1 | 100,00 |
| | 1000 | | | 99,61 |
| 90 | - | 2000x | 0,05 | 53,16 |
| | 625 | | | 69,69 |
| | 650 | | | 99,99 |
| | 675 | | | 100,08 |
| | 700 | | | 100,03 |
| | 800 | 1000x | 0,07 | 99,942 |
| | 1000 | | | 100,00 |

Microstructural characterization was also performed by Transmission Electron Microscopy (TEM) analyzes in the samples just cold rolled to 60% thickness reduction, as well as in the annealed sample at 625°C which was initially subjected to the same cold reduction. It was used a transmission electron microscope JEOL JEM-2010. Slices were cut in the section normal direction (ND) - transverse direction (TD) with 0.3 mm thickness using Struers Accutom-50 equipment. Discs with a diameter of 3.0 mm were taken from these slices using a punch Disc Assy and then were grinded until 0.15 mm thickness in a 1200 mesh grind paper. To reduce the final thickness for producing the hole in the center for transmitting the electron beam it was used a Struers 5 TenuPol with flow rate equal to 29, 30 V and 150 A at -30°C, cooled with liquid nitrogen and methanol. The solution used contained 95% methanol and 5% perchloric acid. Gatan software was used for acquisition and post-processing of acquired images.

### 7.3. Results and discussion

Figure 7.1 shows the band contrast plus grain boundaries maps for samples cold rolled with 60 and 90% thickness reduction and then annealed at 625, 650, 675, 700, 800 and 1000°C. The black lines indicate 15° misorientation from one region to another while

gray indicates 2°. Red lines indicate Σ3 and pink indicate Σ9 twin boundaries, but the amount of this last one is not so significant making it hard to identify in the pictures. The average austenitic grain sizes obtained by EBSD for each condition are shown in Figure 6.2. Note that there is an increase in the austenitic grain size due to increase in annealing temperature for both 60 (Fig. 7.2(a)) and 90% (Fig. 7.2(b)) cold reductions. It was also found that the microstructure generated after austenite reversion is more refined for samples which were initially subjected to higher cold reduction (Fig. 7.2(b)), since this condition provides a larger number of potential nucleation sites which restrict the grain growth. It should be noted that for cold rolled samples as well as those submitted to lower annealing temperatures the indexing were low, weakening this grain size estimation. The areas analyzed in samples annealed at 1000°C were not large enough to be representative of grain size measurements, so they were not showed in these figutres (Fig. 7.2 (a,b)).

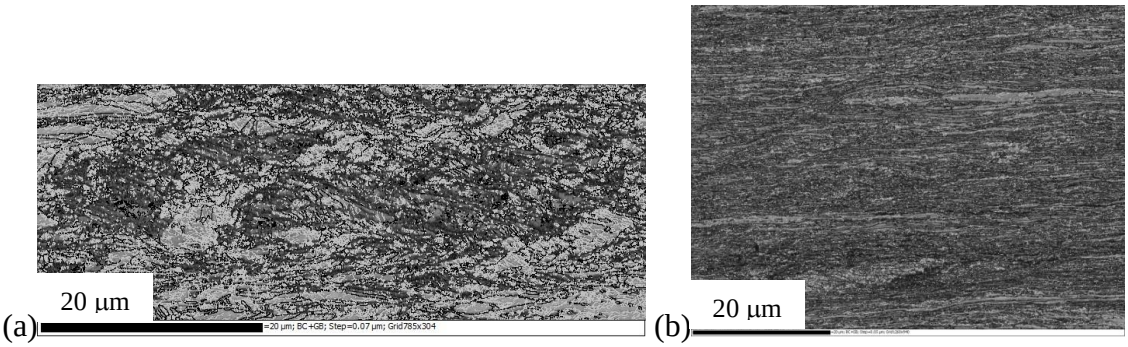


Figure 7.1. Band contrast and grain boundaries maps for samples cold rolled with the following thickness reductions and annealing: (a) 60%; (b) 90%; (c) 60%, 625°C; (d) 90%, 625°C; (e) 60%, 650°C; (f) 90%, 650°C; (g) 60%, 675°C; (h) 90%, 675°C; (i) 60%, 700°C; (j) 90%, 700°C; (k) 60%, 800°C; (l) 90%, 800°C; (m) 60%, 1000°C; (n) 90%, 1000°C. Black lines indicate 15° misorientation from one region to another while gray indicates 2°. Red lines indicate Σ3 twin boundaries and pink is related to Σ9 twin boundaries.

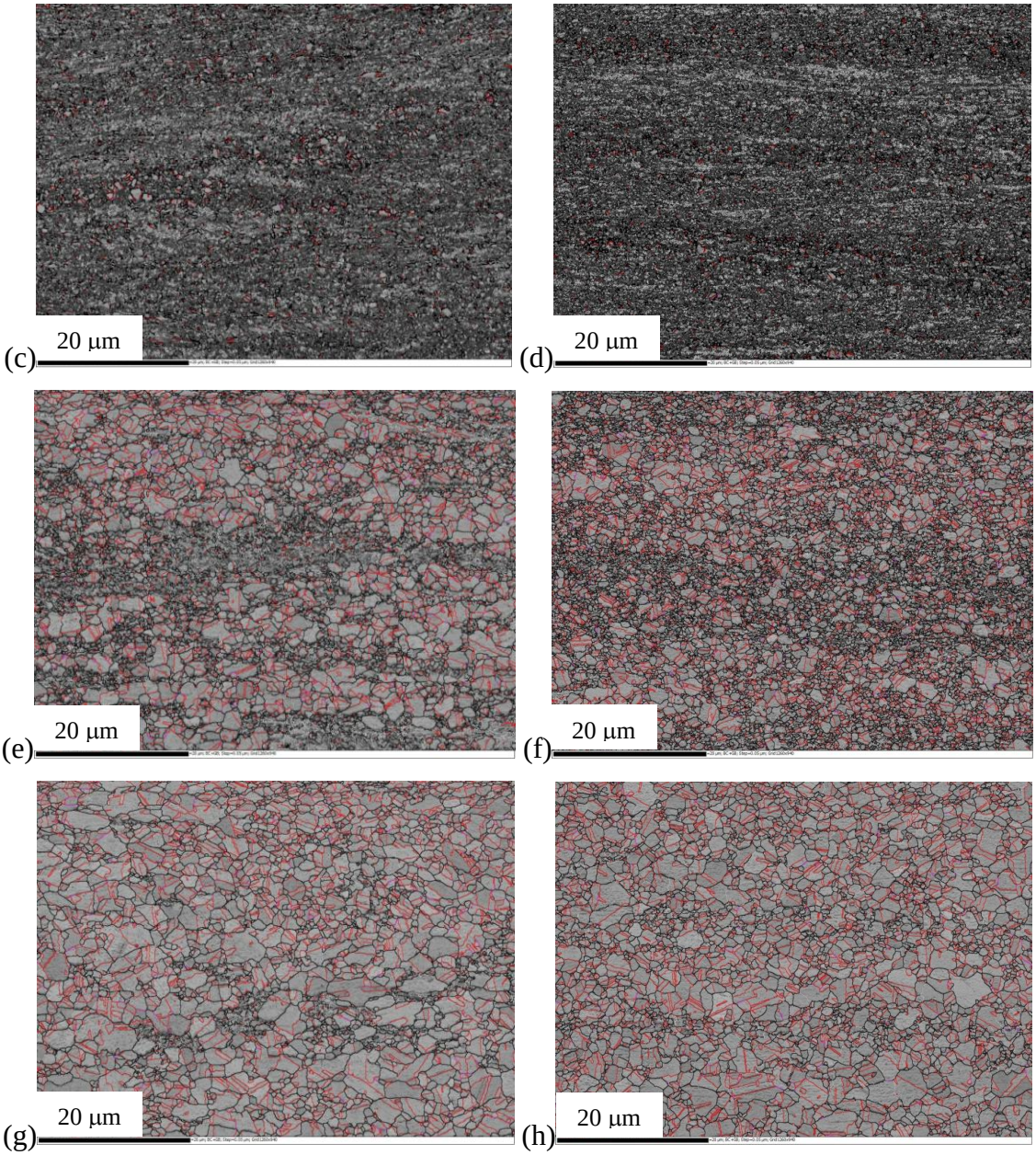


(cont.) Figure 7.1. Band contrast and grain boundaries maps for samples cold rolled with the following thickness reductions and annealing: (a) 60%; (b) 90%; (c) 60%, 625°C; (d) 90%, 625°C; (e) 60%, 650°C; (f) 90%, 650°C; (g) 60%, 675°C; (h) 90%, 675°C; (i) 60%, 700°C; (j) 90%, 700°C; (k) 60%, 800°C; (l) 90%, 800°C; (m) 60%, 1000°C; (n) 90%, 1000°C. Black lines indicate 15° misorientation from one region to another while gray indicates 2°. Red lines indicate Σ3 twin boundaries and pink is related to Σ9 twin boundaries.

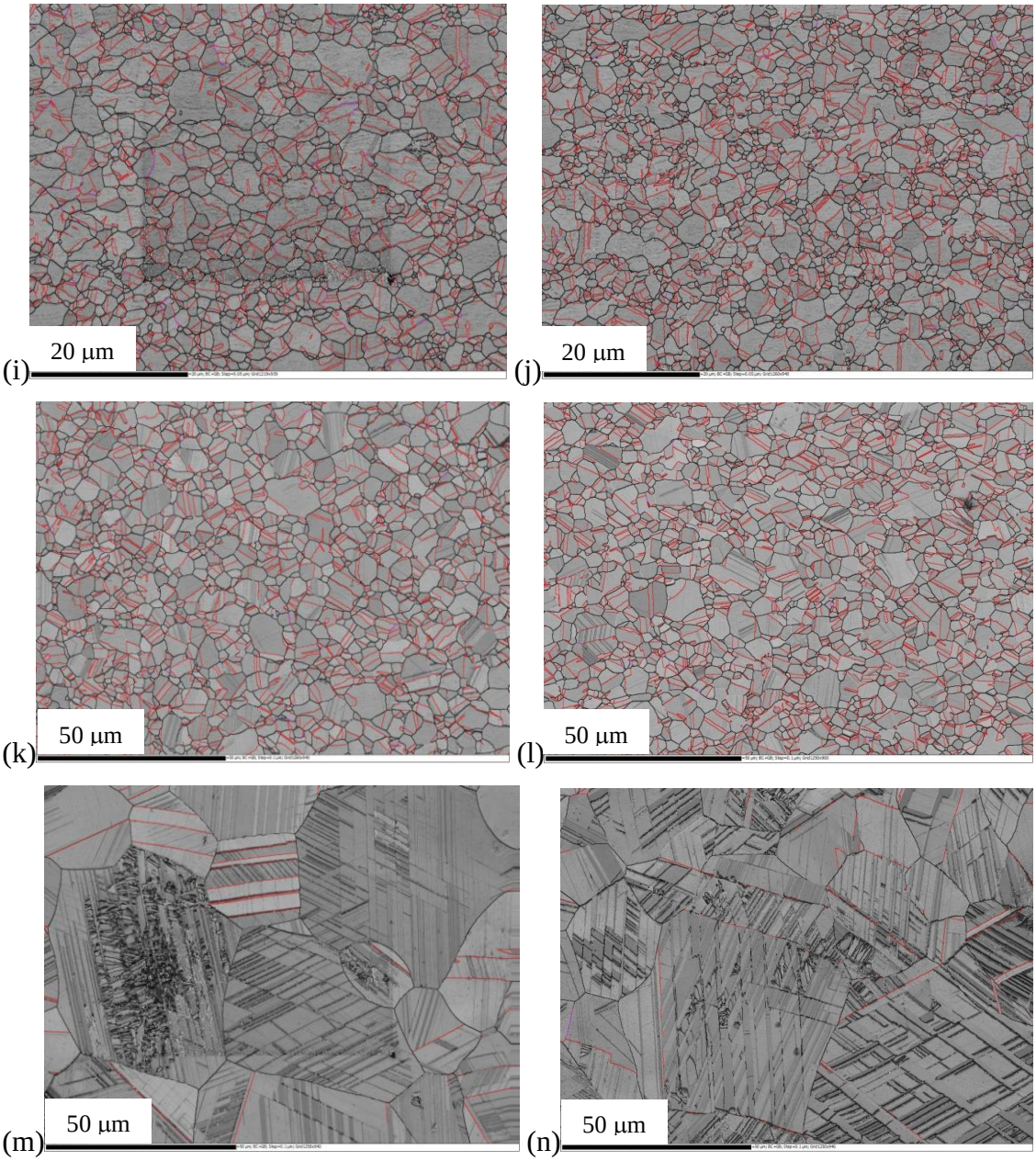


(cont.) Figure 7.1. Band contrast and grain boundaries maps for samples cold rolled with the following thickness reductions and annealing: (a) 60%; (b) 90%; (c) 60%, 625°C; (d) 90%, 625°C; (e) 60%, 650°C; (f) 90%, 650°C; (g) 60%, 675°C; (h) 90%, 675°C; (i) 60%, 700°C; (j) 90%, 700°C; (k) 60%, 800°C; (l) 90%, 800°C; (m) 60%, 1000°C; (n) 90%, 1000°C. Black lines indicate 15° misorientation from one region to another while gray indicates 2°. Red lines indicate Σ3 twin boundaries and pink is related to Σ9 twin boundaries.

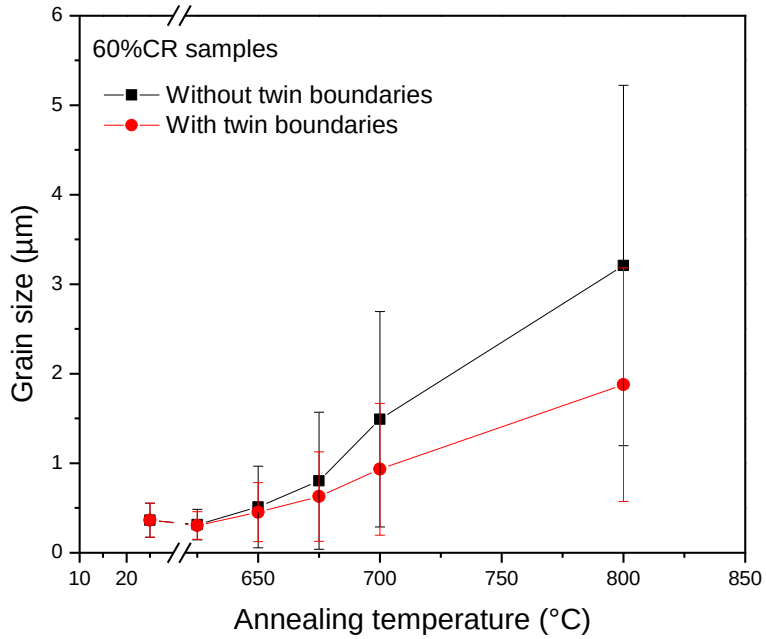


(a)

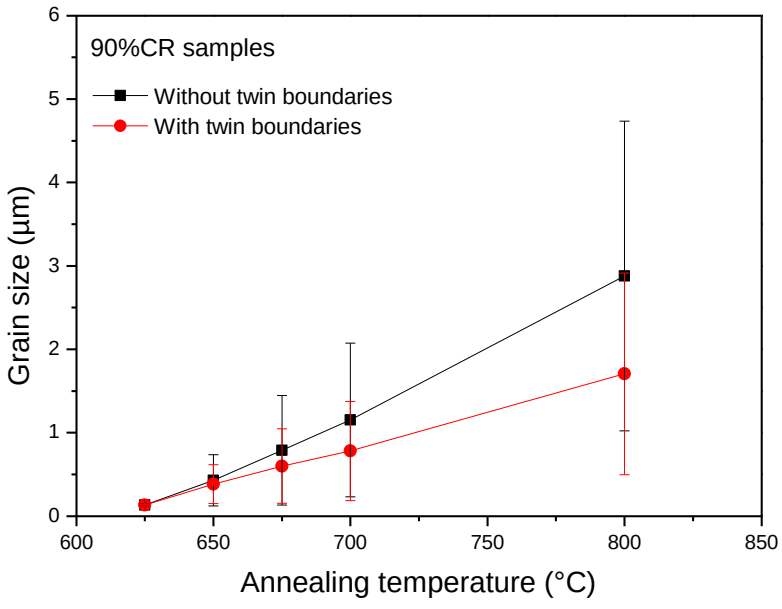


(b)

Figure 7.2. Austenitic grain size for the samples submitted to 60% (a) and 90% (b) cold reduction and annealed at different temperatures.

Figure 7.3 shows the area fraction in austenite of Low Angle Grain Boundaries (LAGBs), first order (Σ3) and second order (Σ9) twin boundaries as well as Total High Angle Boundaries (THAGBs) for samples cold rolled with 60% (Fig. 7.3 (a)) and 90% (Fig. 7.3 (b)) reduction. As the annealing temperature increases, the fraction of LAGBs decreases while the fraction of annealing twin boundaries Σ3 increases and hence the THAGBs, indicating the recrystallization progress for both cold reductions. However, note that the THAGBs value is higher at 625°C for the sample which was initially cold rolled with 90% reduction (Fig. 7.3(b)), indicating that the kinetics of nucleation and growing process are faster for this condition due to the greater stored energy during deformation. The second order twin boundaries (Σ9) values are almost zero for both reductions. As explained before the areas analyzed in samples annealed at 1000°C were not representative for these calculations, so they were not showed in these figures (Fig. 7.3 (a,b)).

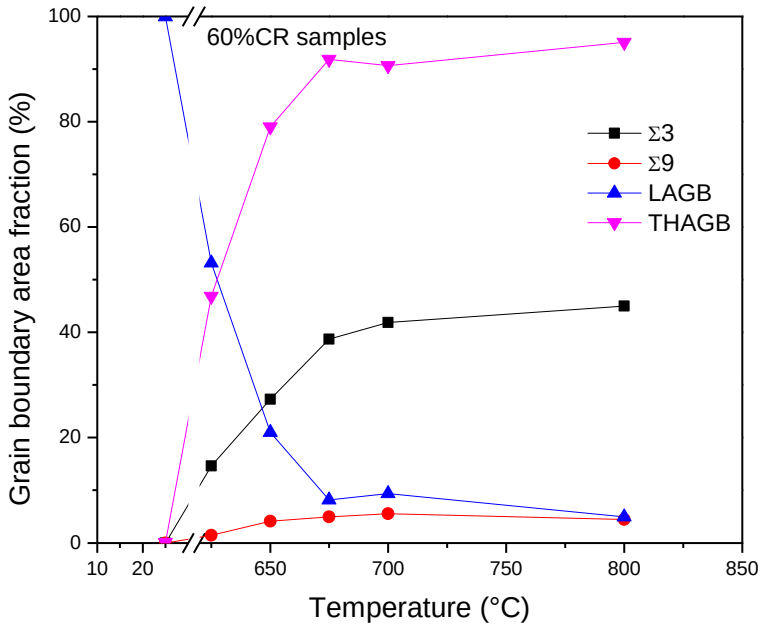


(a)

Figure 7.3. Grain boundary area fraction in austenite for the samples submited to 60% (a) and 90% (b) cold reduction and annealed at different temperatures.

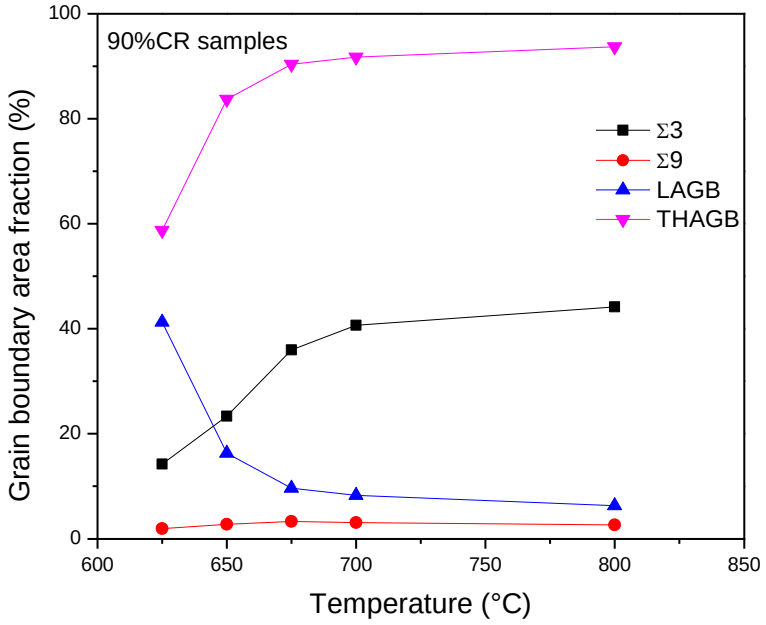


(b)

(cont.) Figure 7.3. Grain boundary area fraction in austenite for the samples submited to 60% (a) and 90% (b) cold reduction and annealed at different temperatures.

Figure 7.4 shows maps with the phases present as well as the high angle grain boundaries (> 15°), in black, for samples cold rolled with 60 and 90% reduction and subsequently annealed at different temperatures. Austenite (fcc) is in blue, α' martensite (bcc) red and ε martensite (hcp) yellow. Figure 7.5 shows the area fraction calculated for the all phases in the 60 (Fig. 7.5 (a)) and 90% (Fig. 7.5.b) cold rolled samples. It is pertinent to remember that for cold rolled samples and also for that samples which were submitted to lower annealing temperatures the indexing were low and the areas analyzed in samples annealed at 1000°C were not large enough to be representative.

It was verified the existence of α' and ε martensites, as well some retained austenite, in the sample subjected to 60% cold reduction (Fig. 7.4 (a)). But, for greater cold reduction (Fig. 7.4 (b)), α' martensite formation was induced more intensely. This indicates that phase transformation induced by deformation occurs in two steps $\gamma \rightarrow \varepsilon \rightarrow \alpha'$ and that α' martensite tends to be the major phase when deformation increases.

This is in accordance with previous studies for different metastable austenitic alloys[17,18]. Note also that the reversion of α' and ε martensite into austenite during annealing is practically complete at 700°C for both cold rolling conditions (Fig. 7.4 (i,j)). It is also noted that for samples 90% cold rolled and after annealed at 625 to 650°C (Fig. 7.4(d,f)) the reversion occurs faster compared to the samples 60% cold rolled and after annealed at the same temperatures(Fig. 7.4(c,e)). However, at 800 and 1000°C annealing temperatures for both cold rolling conditions (Fig. 7.4(k-n)), the ε and α' martensites start to appear again and it is difficult to eliminate them completely. This fact leads to conclude that these ε and α' martensites were formed during water quenching after soaking. This phenomena has been also reported in other Fe-Mn alloys[19-22].

It is easy to check in samples annealed at 1000°C for both cold rolling conditions (Fig. 7.4(m,n)) that the α' martensite has formed within two twin boundaries or at the intersection of two ε martensite plates and in some regions at grain boundaries and spread within the parent γ grain. This preferred nucleation sites for α' martensite detected here are in accordance with the literature[23-25]. On the other, hand Ding *et al.*[2] have reported that ε martensite nucleates through the stacking faults generated by partial dislocations or from the overlap of these faults.

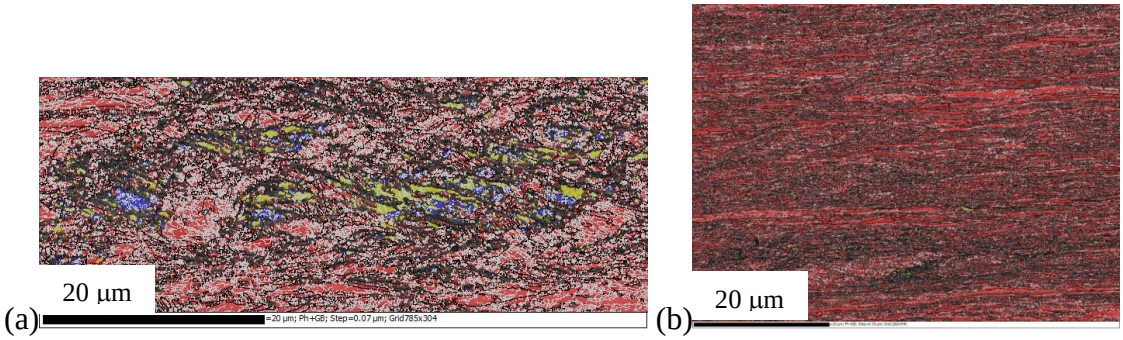

(a) (b)

Figure 7.4. Phase maps of the samples cold rolled with the following thickness reductions and annealing: (a) 60%; (b) 90%; (c) 60%, 625°C; (d) 90%, 625°C; (e) 60%, 650°C; (f) 90%, 650°C; (g) 60%, 675°C; (h) 90%, 675°C; (i) 60%, 700°C; (j) 90%, 700°C; (k) 60%, 800°C; (l) 90%, 800°C; (m) 60%, 1000°C; (n) 90%, 1000°C. Austenite (fcc) is in blue, red is α' martensite (bcc) and yellow is martensite ε (hcp). The high angle grain boundaries (>15°) are in black.

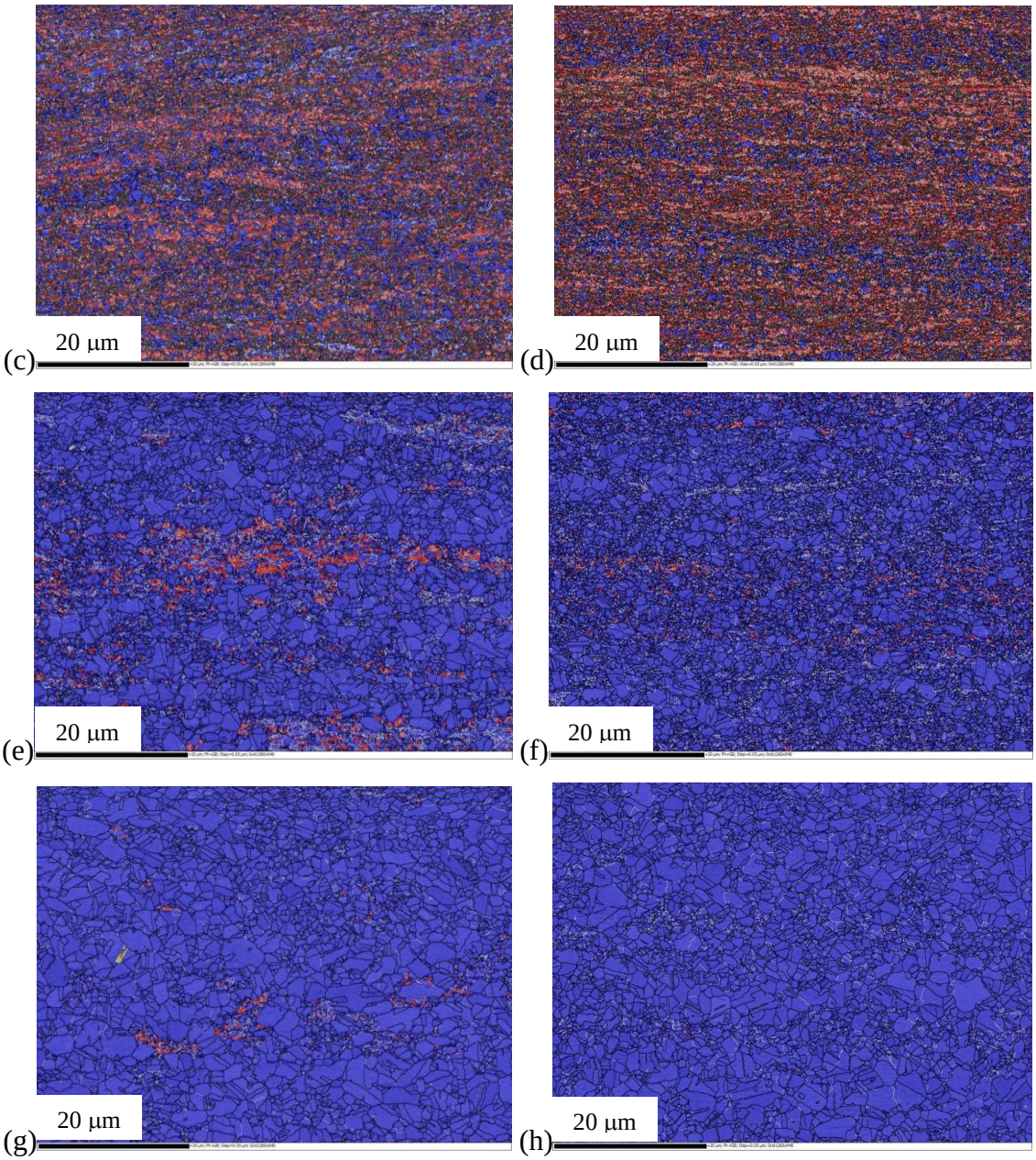


(cont.) Figure 7.4. Phase maps of the samples cold rolled with the following thickness reductions and annealing: (a) 60%; (b) 90%; (c) 60%, 625°C; (d) 90%, 625°C; (e) 60%, 650°C; (f) 90%, 650°C; (g) 60%, 675°C; (h) 90%, 675°C; (i) 60%, 700°C; (j) 90%, 700°C; (k) 60%, 800°C; (l) 90%, 800°C; (m) 60%, 1000°C; (n) 90%, 1000°C. Austenite (fcc) is in blue, red is α' martensite (bcc) and yellow is martensite ε (hcp). The high angle grain boundaries (>15°) are in black.

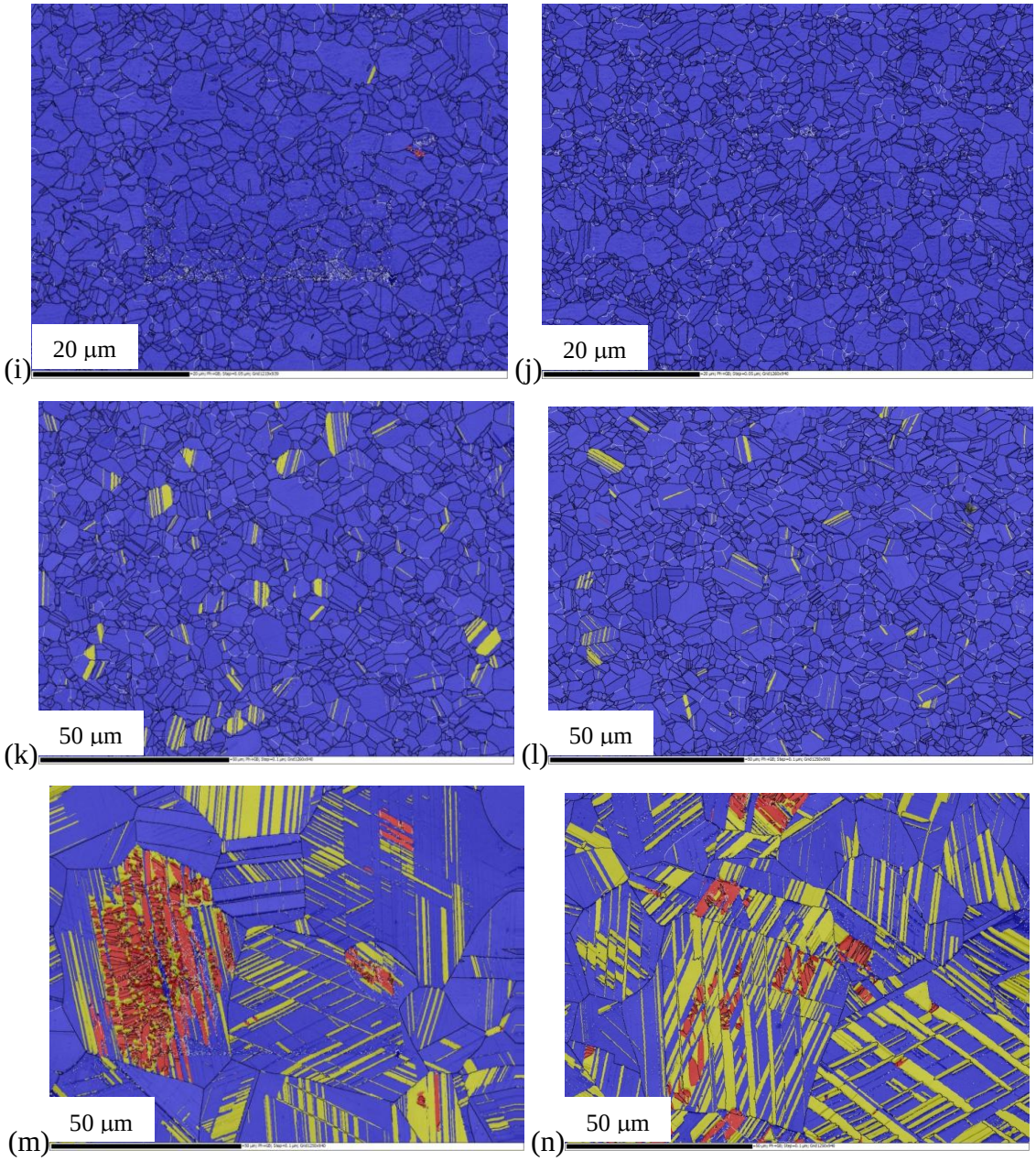


(cont.) Figure 7.4. Phase maps of the samples cold rolled with the following thickness reductions and annealing: (a) 60%; (b) 90%; (c) 60%, 625°C; (d) 90%, 625°C; (e) 60%, 650°C; (f) 90%, 650°C; (g) 60%, 675°C; (h) 90%, 675°C; (i) 60%, 700°C; (j) 90%, 700°C; (k) 60%, 800°C; (l) 90%, 800°C; (m) 60%, 1000°C; (n) 90%, 1000°C. Austenite (fcc) is in blue, red is α' martensite (bcc) and yellow is martensite ε (hcp). The high angle grain boundaries (>15°) are in black.

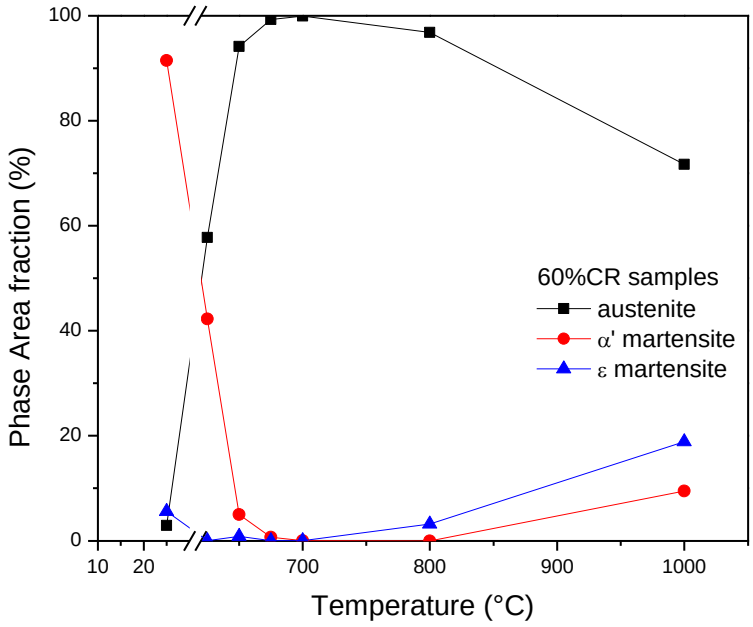


(a)

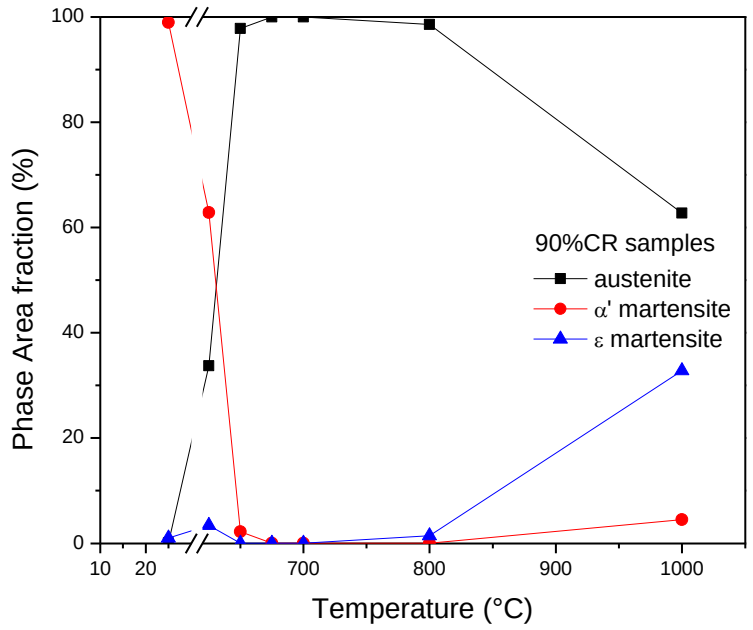


(b)

Figure 7.5. Phase area fraction for the samples submitted to 60% (a) and 90% (b) thickness reduction and annealed at different temperatures.

Figure 7.6 shows the misorientation distributions for each phases present in the samples annealed at 1000°C initially subjected to 60 (Fig. 7.6 (a,c,e)) and 90% (Fig. 7.6 (b,d,f)) cold reduction. For austenite (Fig. 7.6 (a-b)) besides the presence of low angle boundaries, it is possible to verify first order twin boundaries (Σ3), which are associated with 60° <111> misorientation[26,27].

According to K-S orientation relationship 24 equivalent crystallographic variants in α' martensite may be formed from an austenitic grain due to the cubic symmetry[23]. Morito *et al.*[28] reported the axis/angle pairs between different variants of the K-S OR, which are consistent with the presented results. In the K-S relationship, there are certain combinations of the variants that show special coincidence site lattice (CSL) relationships, such as Σ3. The Table VII.2 show the 24 possible variants which satisfy the K-S OR and the 10 different angles which can be formed from these variants[23,27]. Table VII.2 also indicates the CSL relationships when Brandon criterion is satisfied[29].

Figures 7.6 (c, d) show that, for α' martensite in this steel under study, it is noted that beyond low angle boundaries is remarkable the presence of 50.51° misorientation angles. These angles simply indicate misorientation between two distinct variants in α' martensite according to Naraghi *et al*[23]. Literature commonly reports 5 to 10° misorientations from the ideal <011>10.53º misorientation relationship between two variants[27,28], but these peaks does not appear for α' martensite in this analysis. Figures 7.6 (c, d) also show 60° misorientation angles for α' martensite. Sang-Gyu Park *et al.* reported that packet boundaries with misorientation angles of 60° corresponds to the coincidence site lattice (CSL) Σ3 boundary[30].

According to Yang Ping *et al.*[31] the approximately 70° misorientation in ε martensite (Fig. 7.6(e,f)) is the misorientation angle between two variants formed on different $\{111\}_\gamma$, 70°<110>. Jae-Bok Seol *et al.*[32] affirm that the habit plane between γ and ε-plates is $\{111\}_\gamma$ and that this OR is Shoji-Nishiyama (S-N)[12], $\{111\}_\gamma//\{0002\}_\varepsilon$ and $[112]_\gamma//[1100]_\varepsilon$ or $[110]_\gamma//[1120]_\varepsilon$. This ~70° are also easy to see in the phase maps showed before for samples annealed at 1000°C for both cold rolling conditions (Fig. 7.4(m,n)) and it has being frequently reported in the literarture[33,34].

Table VII.2. The 24 K-S variants and misorientations angles from the variant V1[23, 27].

| Variant number | Plane parallel | Direction parallel | Misorientations angles from V1 (°) | CSL* |
|---|---|---|---|---|
| 1 | $(111)_\gamma//(011)_{\alpha'}$ | $[\bar{1}01]_\gamma//[\bar{1}\bar{1}1]_{\alpha'}$ | - | - |
| 2 | | $[\bar{1}01]_\gamma//[\bar{1}1\bar{1}]_{\alpha'}$ | 60.0 | Σ3 |
| 3 | | $[01\bar{1}]_\gamma//[\bar{1}\bar{1}1]_{\alpha'}$ | 60.0 | - |
| 4 | | $[01\bar{1}]_\gamma//[\bar{1}1\bar{1}]_{\alpha'}$ | 10.53 | Σ1 |
| 5 | | $[1\bar{1}0]_\gamma//[\bar{1}\bar{1}1]_{\alpha'}$ | 60.0 | - |
| 6 | | $[1\bar{1}0]_\gamma//[\bar{1}1\bar{1}]_{\alpha'}$ | 49.47 | Σ11 |
| 7 | $(1\bar{1}1)_\gamma//(011)_{\alpha'}$ | $[10\bar{1}]_\gamma//[\bar{1}\bar{1}1]_{\alpha'}$ | 49.47 | Σ19b |
| 8 | | $[10\bar{1}]_\gamma//[\bar{1}1\bar{1}]_{\alpha'}$ | 10.53 | Σ1 |
| 9 | | $[\bar{1}\bar{1}0]_\gamma//[\bar{1}\bar{1}1]_{\alpha'}$ | 50.51 | - |
| 10 | | $[\bar{1}\bar{1}0]_\gamma//[\bar{1}1\bar{1}]_{\alpha'}$ | 50.51 | - |
| 11 | | $[011]_\gamma//[\bar{1}\bar{1}1]_{\alpha'}$ | 14.88 | Σ1 |
| 12 | | $[011]_\gamma//[\bar{1}1\bar{1}]_{\alpha'}$ | 57.21 | - |
| 13 | $(\bar{1}11)_\gamma//(011)_{\alpha'}$ | $[0\bar{1}1]_\gamma//[\bar{1}\bar{1}1]_{\alpha'}$ | 14.88 | Σ1 |
| 14 | | $[0\bar{1}1]_\gamma//[\bar{1}1\bar{1}]_{\alpha'}$ | 50.51 | - |
| 15 | | $[\bar{1}0\bar{1}]_\gamma//[\bar{1}\bar{1}1]_{\alpha'}$ | 57.21 | - |
| 16 | | $[\bar{1}0\bar{1}]_\gamma//[\bar{1}1\bar{1}]_{\alpha'}$ | 20.61 | - |
| 17 | | $[110]_\gamma//[\bar{1}\bar{1}1]_{\alpha'}$ | 51.73 | - |
| 18 | | $[110]_\gamma//[\bar{1}1\bar{1}]_{\alpha'}$ | 47.11 | - |
| 19 | $(11\bar{1})_\gamma//(011)_{\alpha'}$ | $[\bar{1}10]_\gamma//[\bar{1}\bar{1}1]_{\alpha'}$ | 50.51 | - |
| 20 | | $[\bar{1}10]_\gamma//[\bar{1}1\bar{1}]_{\alpha'}$ | 57.21 | - |
| 21 | | $[0\bar{1}\bar{1}]_\gamma//[\bar{1}\bar{1}1]_{\alpha'}$ | 20.61 | - |
| 22 | | $[0\bar{1}\bar{1}]_\gamma//[\bar{1}1\bar{1}]_{\alpha'}$ | 47.11 | - |
| 23 | | $[101]_\gamma//[\bar{1}\bar{1}1]_{\alpha'}$ | 57.21 | - |
| 24 | | $[101]_\gamma//[\bar{1}1\bar{1}]_{\alpha'}$ | 21.06 | - |

* Coincidence site lattice is indicated when Brandon criterion[29] is satisfied.

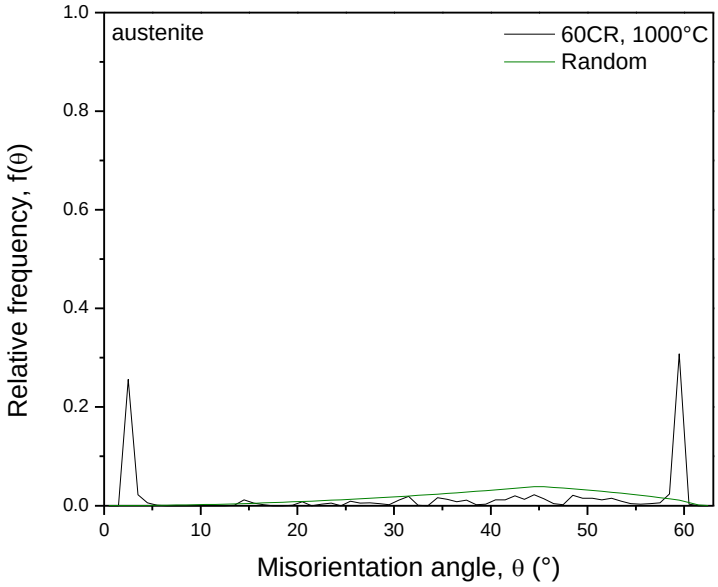


(a)

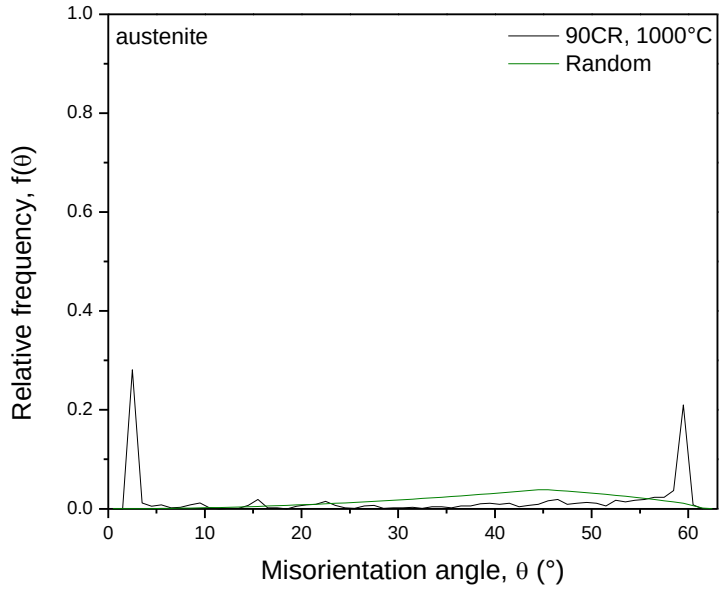


(b)

Figure 7.6. Misorientations distributions for samples annealed at 1000°C initially subjected to 60% cold rolled showing austenite (a), α' martensite (c) and ε martensite (e). The (b), (d) and (f) represent the same phases, respectively, but for the samples cold rolled with 90% thickness reduction and annealed at 1000°C.

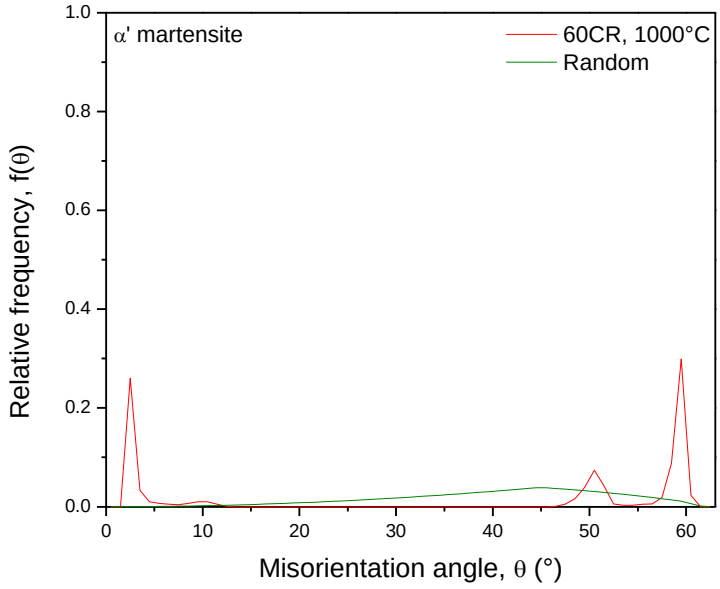


(c)

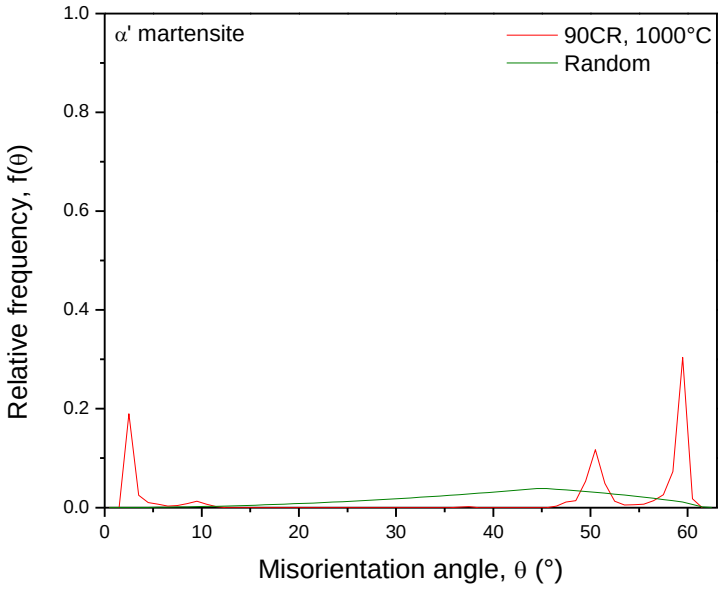


(d)

(cont.) Figure 7.6. Misorientations distributions for samples annealed at 1000°C initially subjected to 60% cold rolled showing austenite (a), α' martensite (c) and ε martensite (e). The (b), (d) and (f) represent the same phases, respectively, but for the samples cold rolled with 90% thickness reduction and annealed at 1000°C.

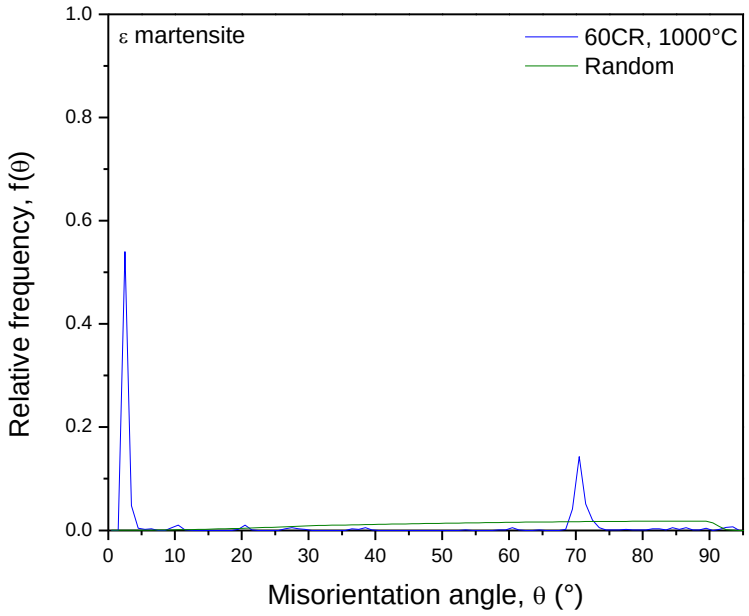


(e)

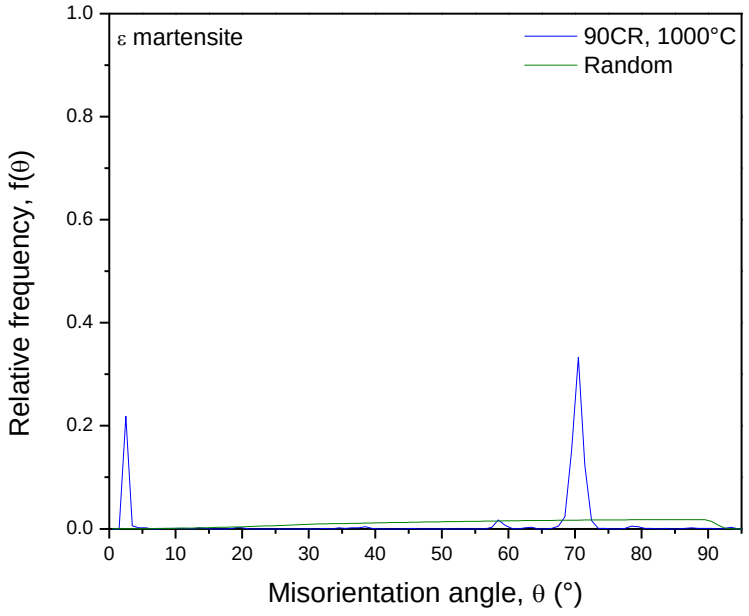


(f)

(cont.) Figure 7.6. Misorientations distributions for samples annealed at 1000°C initially subjected to 60% cold rolled showing austenite (a), α' martensite (c) and ε martensite (e). The (b), (d) and (f) represent the same phases, respectively, but for the samples cold rolled with 90% thickness reduction and annealed at 1000°C.

Figures 7.7 and 7.8 show the microstructural characterization by TEM. In the sample cold rolled with 60% thickness reduction residual austenite was not identified with this technique (Fig. 7.7), differently of the result obtained by EBSD (Fig. 7.4 (a)) which analysed a larger area. The α' martensite was found to have different dislocation density and irregular shape. Figure 7.7(a) shows areas of high while Figure 7.7(c) shows low dislocation density. According to Tae-Ho Lee *et.al.*[34] the intersection of two ε martensite plates results in α' martensite formation and their morphologies are diverse, as parallelograms confined within an intersecting area or irregular shapes consisting of several overlapped α' martensite laths.

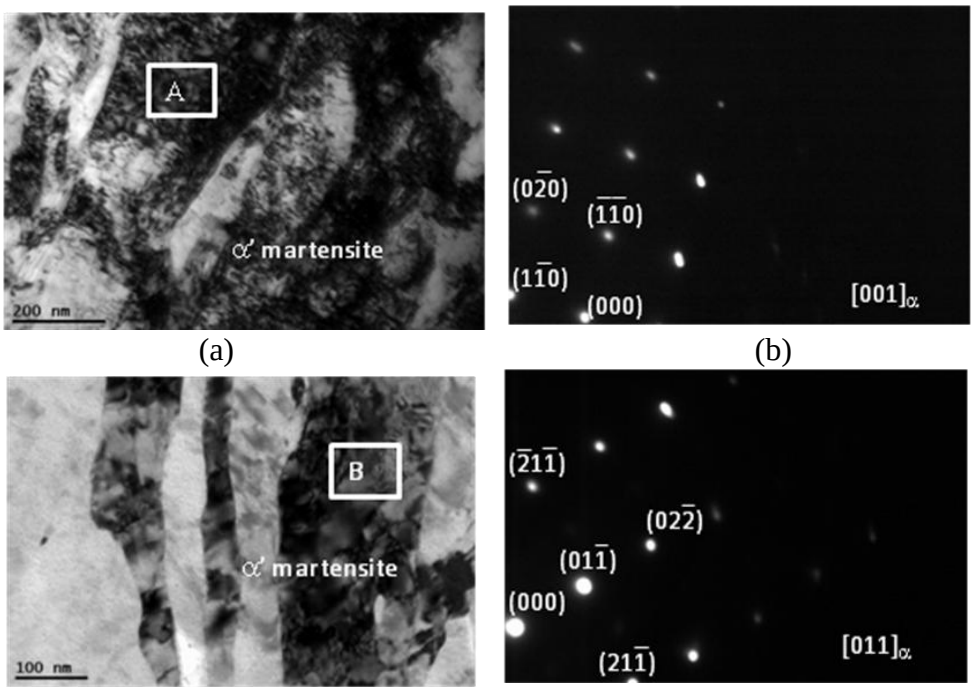


Figure 7.7. Representative bright field TEM micrograph (a) with a corresponding diffraction pattern, taken from region "A" (b), for the 60 % cold rolled steel showing high dislocation density martensitic grains. Bright field TEM micrograph (c) with a corresponding diffraction pattern, taken from region "B" (d), showing low dislocation density martensitic grains.

It is clear in Figure 7.8(a, b) that following annealing at 625°C austenite formation took place. Significant amount of annealing twins was observed in austenite (Fig. 7.8(a)) which corroborates the result presented in Figure 7.3(a) by EBSD. Sometimes there are

some difficulties for indexing by EBSD twins which are just tens of nanometers[10], but with TEM they became easier to be identified, as shown in Figure 7.8(a). It was verified in Figure 7.8(c) that there are austenitic grains with low dislocation density. The dislocation density in α' martensite significantly decreased after annealing (Fig. 7.8(d)) when compared to the cold rolled condition (Fig. 7.7(a)).

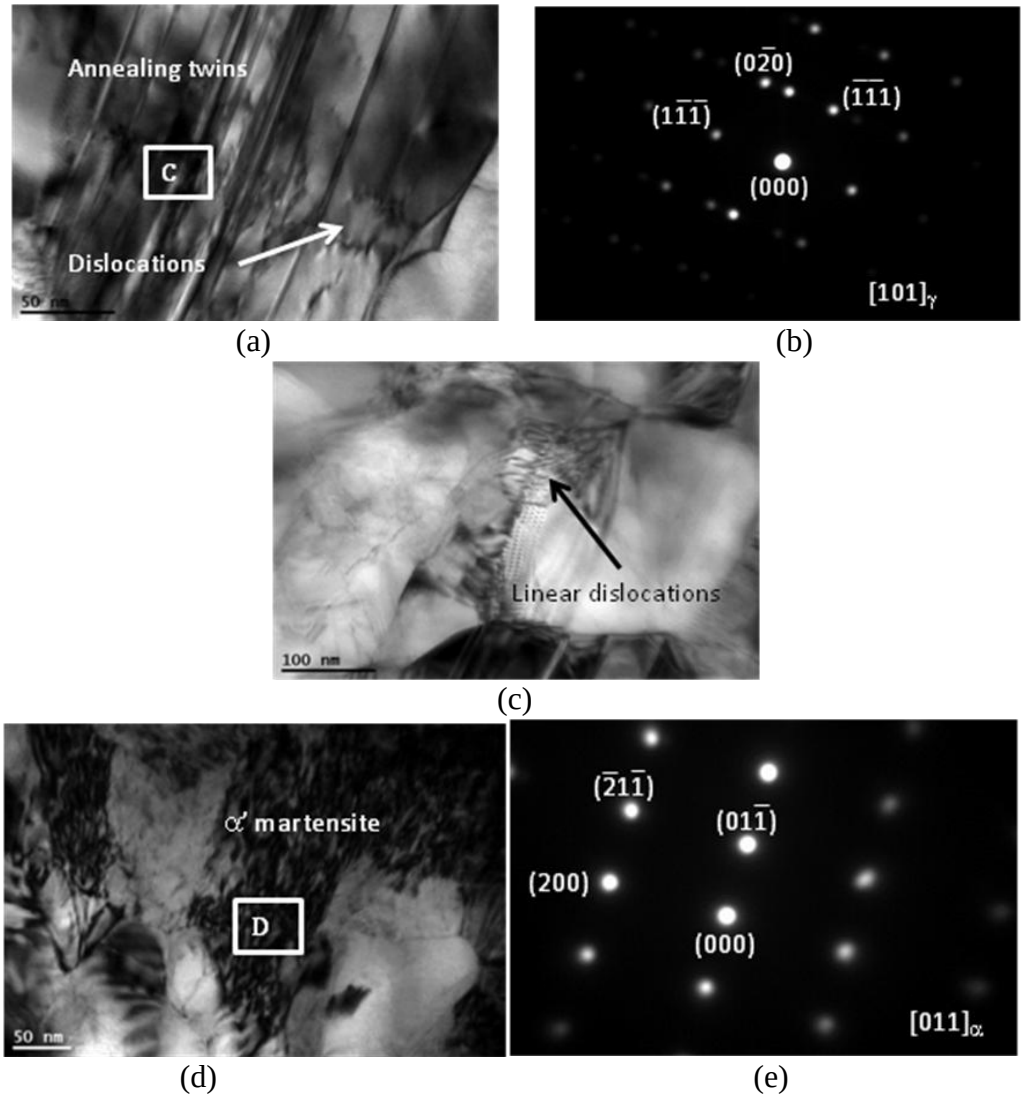


Figure 7.8. A representative bright field TEM micrograph (a) with a corresponding diffraction pattern, taken from region "C" (b), for the 60 % cold rolled and annealed at 625°C steel showing annealing twins and some dislocations in austenitic grain (a) as well a net-work of linear dislocations (c). Bright field TEM micrograph (d) with a corresponding diffraction pattern, taken from region "D" (e), showing dislocation structure in α' martensite.

Figure 7.9 shows the Inverse Pole Figure (IPF) obtained by EBSD for samples cold rolled with 60 and 90% reduction and annealed at different temperatures. In this crystallographic orientation maps the high angle boundaries (> 15°) are highlighted in black and the low angle (< 2°) in red.

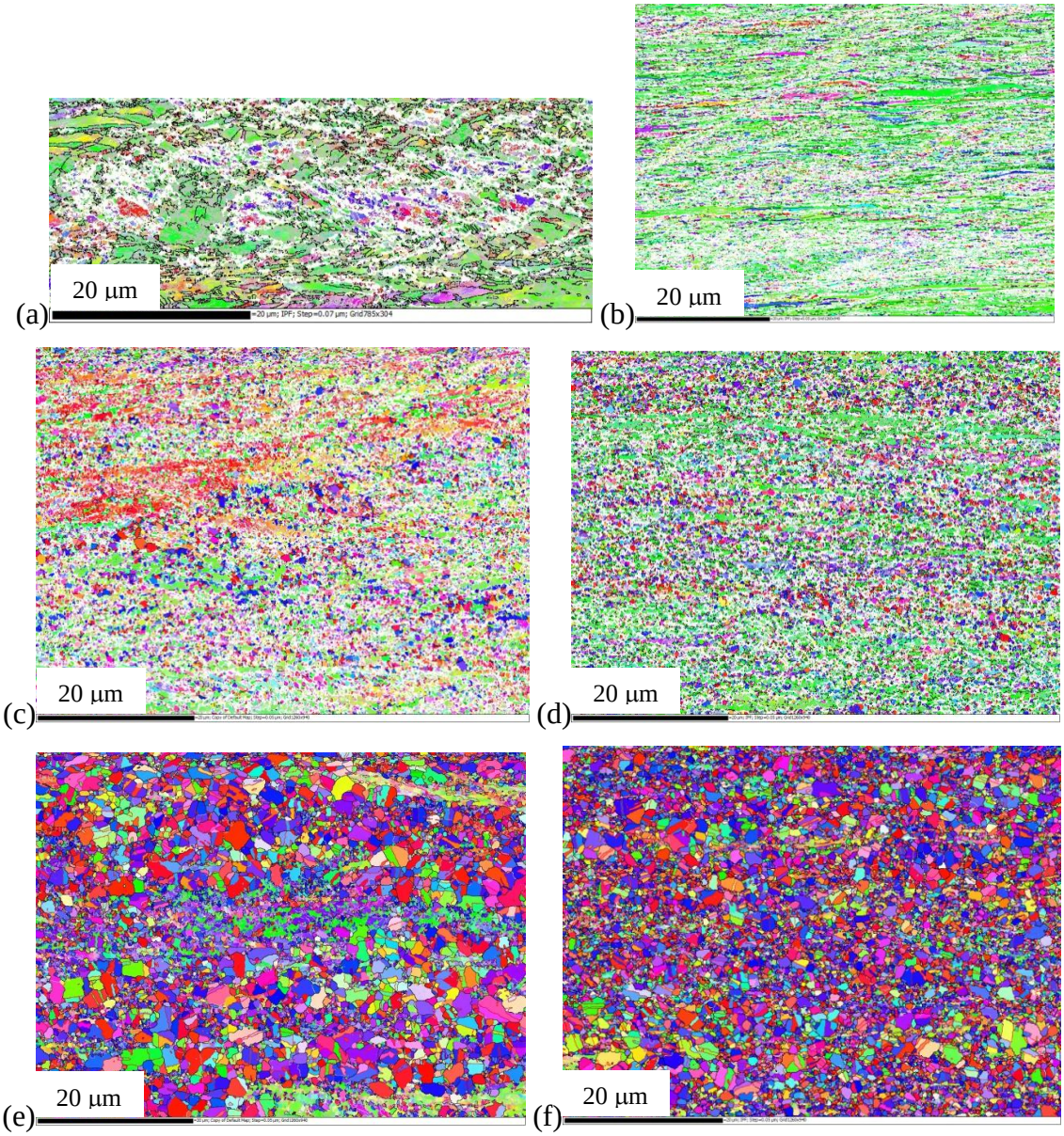


Figure 7.9. Inverse Pole Figure maps of the samples cold rolled with the following thickness reductions and annealing: (a) 60%; (b) 90%; (c) 60%, 625°C; (d) 90%, 625°C; (e) 60%, 650°C; (f) 90%, 650°C; (g) 60%, 675°C; (h) 90%, 675°C; (i) 60%, 700°C; (j) 90%, 700°C; (k) 60%, 800°C; (l) 90%, 800°C; (m) 60%, 1000°C; (n) 90%, 1000°C. (o) Reference stereographic triangles for each phase.

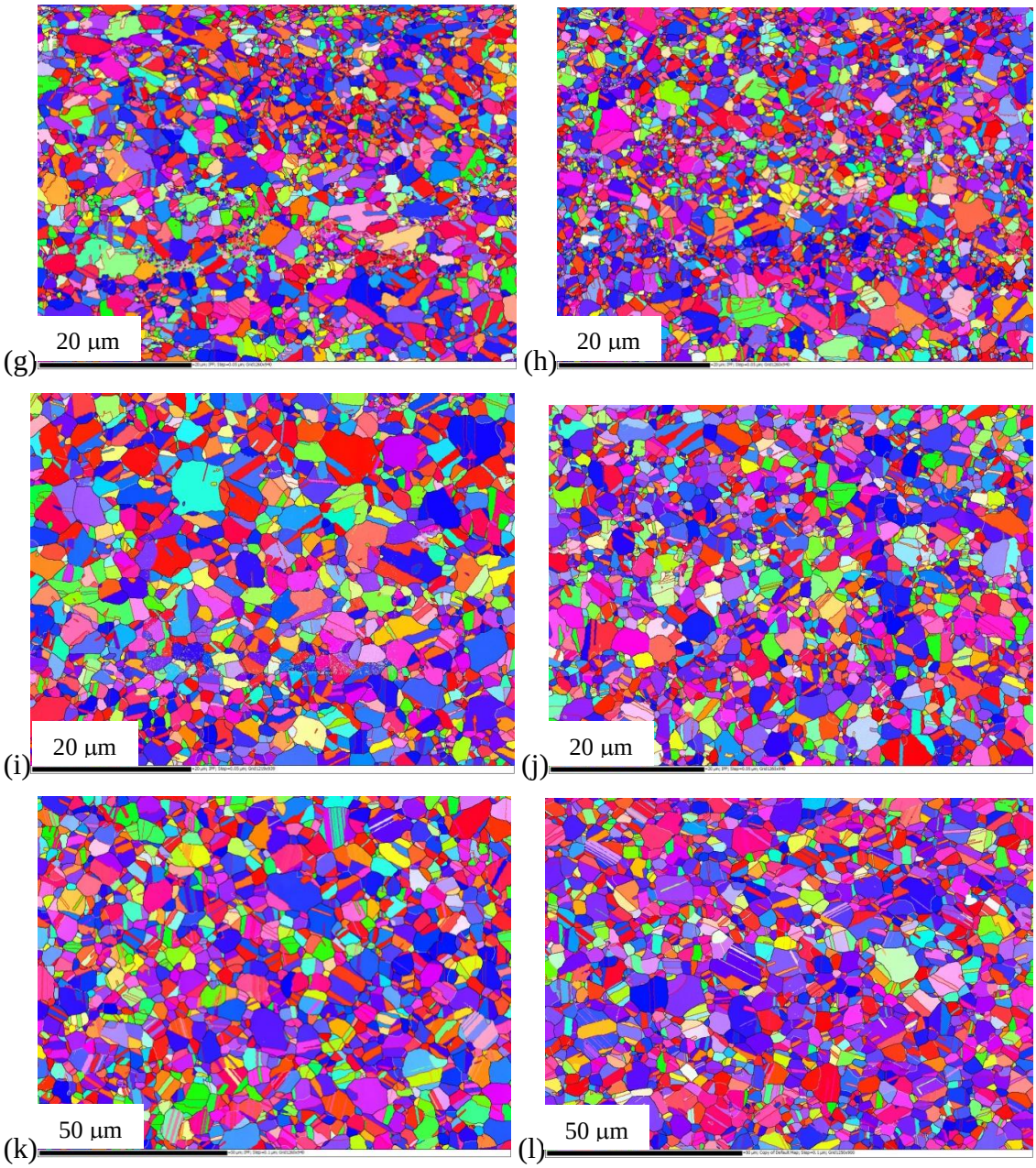


(cont.) Figure 7.9. Inverse Pole Figure maps of the samples cold rolled with the following thickness reductions and annealing: (a) 60%; (b) 90%; (c) 60%, 625°C; (d) 90%, 625°C; (e) 60%, 650°C; (f) 90%, 650°C; (g) 60%, 675°C; (h) 90%, 675°C; (i) 60%, 700°C; (j) 90%, 700°C; (k) 60%, 800°C; (l) 90%, 800°C; (m) 60%, 1000°C; (n) 90%, 1000°C. (o) Reference stereographic triangles for each phase.

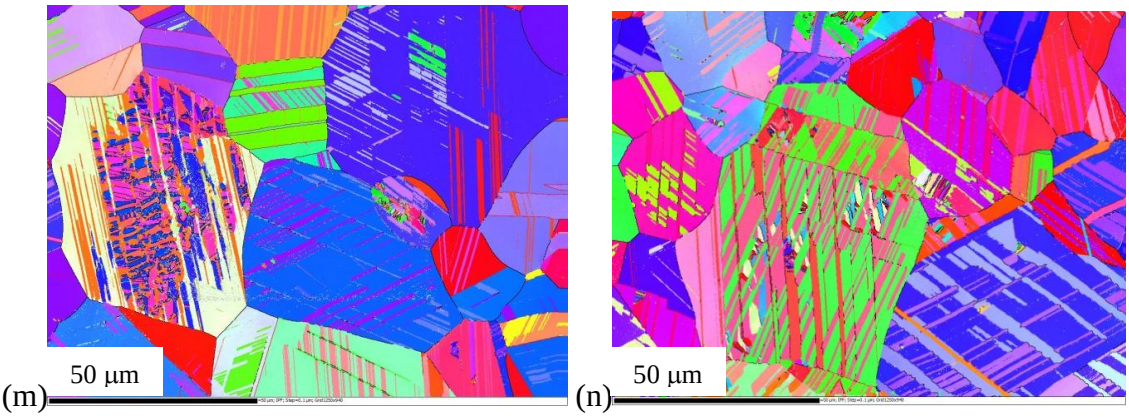


(m) (n)

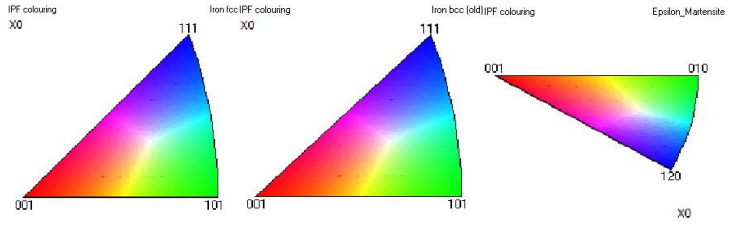


(o)

(cont.) Figure 7.9. Inverse Pole Figure maps of the samples cold rolled with the following thickness reductions and annealing: (a) 60%; (b) 90%; (c) 60%, 625°C; (d) 90%, 625°C; (e) 60%, 650°C; (f) 90%, 650°C; (g) 60%, 675°C; (h) 90%, 675°C; (i) 60%, 700°C; (j) 90%, 700°C; (k) 60%, 800°C; (l) 90%, 800°C; (m) 60%, 1000°C; (n) 90%, 1000°C. (o) Reference stereographic triangles for each phase.

The use of orientation distribution functions (ODFs) by three Euler angles, using the Bunge notation, is necessary for better interpretation of texture results. The section $\phi_2$=45° in the Bunge space (Fig. 7.10) has particular importance to evaluate the α' martensite and austenite textures in rolled metals because it shows the main components and fibers of interest[35].

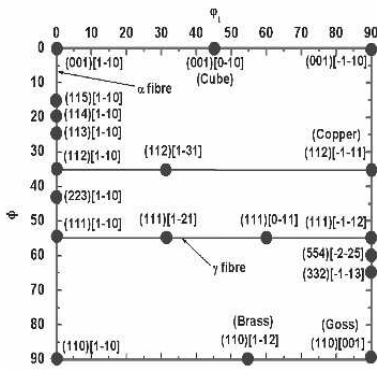


Figure 7.10. Section $\phi_2$=45° in Bunge space[35].

Figure 7.11 shows ODFs for α’ martensite, sections ϕ2=0° and ϕ2=45°, for samples cold rolled with 60 and 90% reduction and annealed at different temperatures. Similarly, Figure 7.12 shows the same ODFs for the same samples with respect to the austenite.

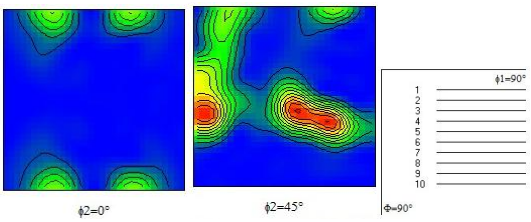


(a) 60% CR - α’ martensite

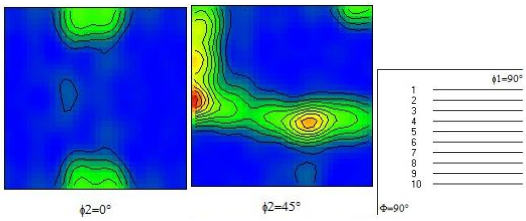


(b) 90% CR - α’ martensite

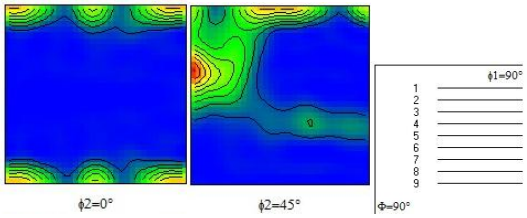


(c) 60% CR, 625°C - α’ martensite

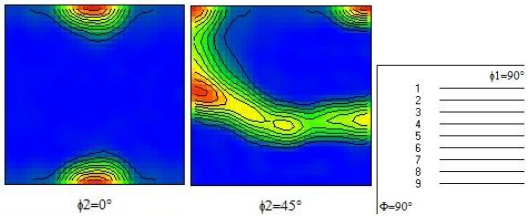


(d) 90% CR, 625°C - α’ martensite

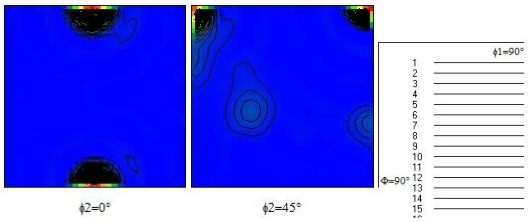


(e) 60% CR, 650°C - α’ martensite

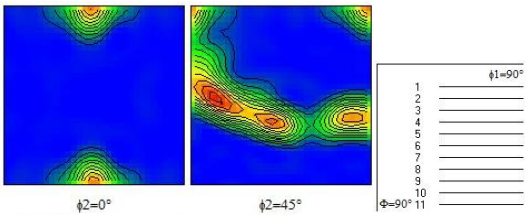


(f) 90% CR, 650°C - α’ martensite

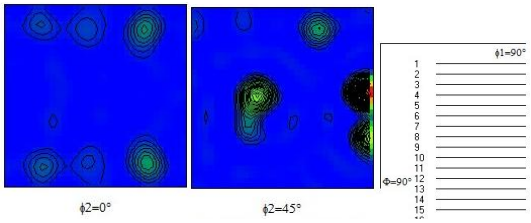


(g) 60% CR, 1000°C - α’ martensite

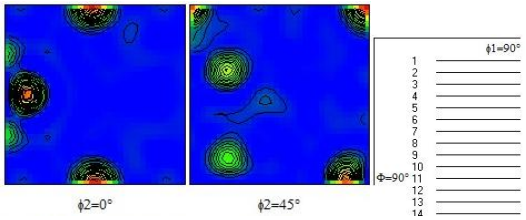


(h) 90% CR, 1000°C - α’ martensite

Figure 7.11. α’ martensite orientation distribution functions (ODFs), sections ϕ2=0° and ϕ2=45°, for samples cold rolled with 60 and 90% reduction and annealed at different temperatures.

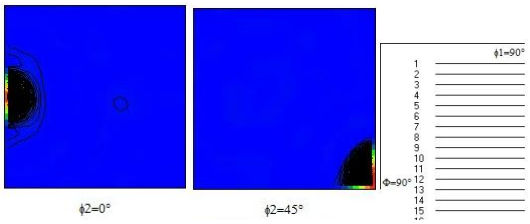


(a) 60% CR – austenite

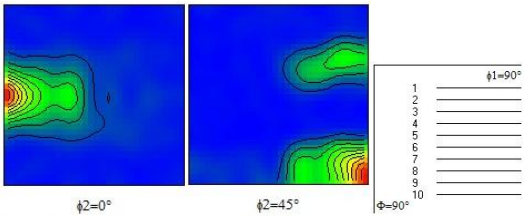


(b) 60% CR, 625°C – austenite

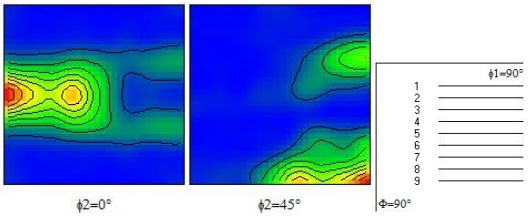


(c) 90% CR, 625°C - austenite

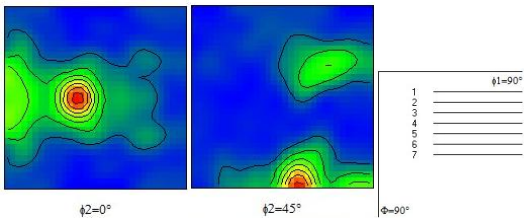


(d) 60% CR, 650°C – austenite

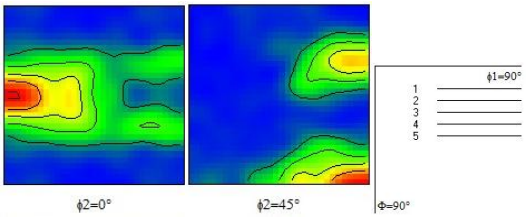


(e) 90% CR, 650°C – austenite

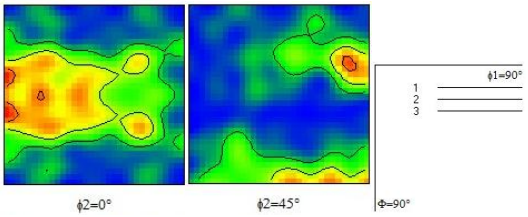


(f) 60% CR, 675°C – austenite

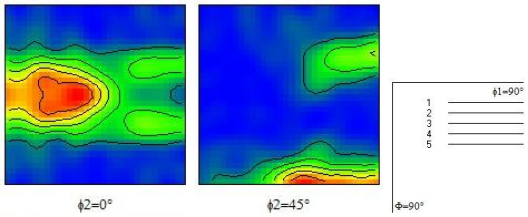


(g) 90% CR, 675°C – austenite

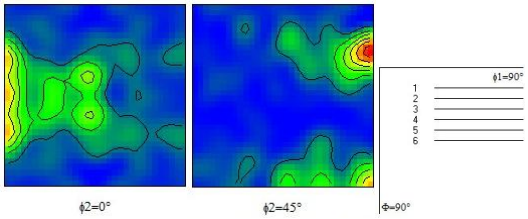


(h) 60% CR, 700°C – austenite

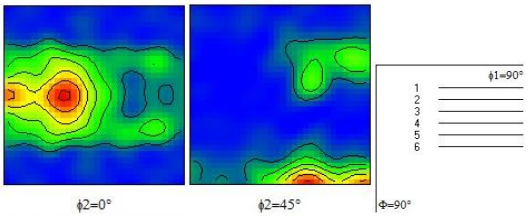


(i) 90% CR, 700°C – austenite

Figure 7.12. Austenite orientation distribution function (ODF), sections ϕ2=0° and ϕ2=45°, for samples cold rolled with 60 and 90% reduction and annealed at different temperatures.

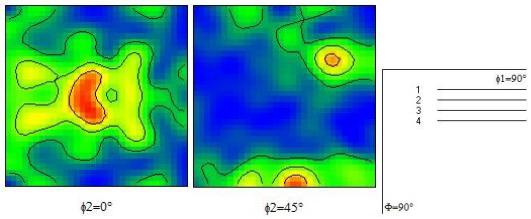


(j) 60% CR, 800°C – austenite

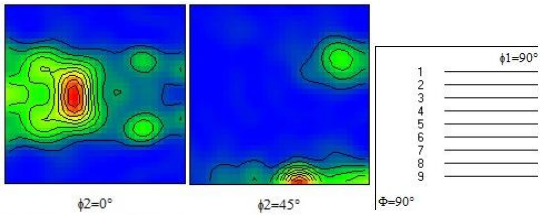


(k) 90% CR, 800°C – austenite

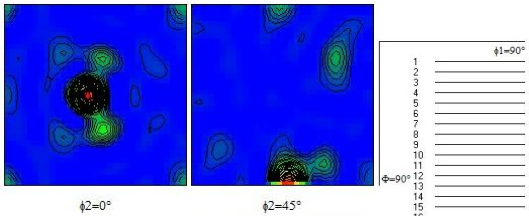


(l) 60% CR, 1000°C – austenite

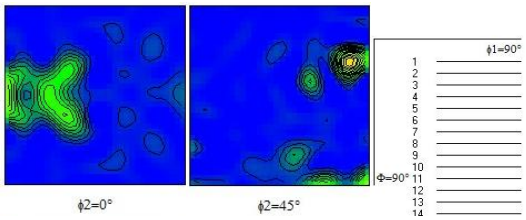


(m) 90% CR, 1000°C – austenite

(cont.) Figure 7.12. Austenite orientation distribution function (ODF), sections ϕ2=0° and ϕ2=45°, for samples cold rolled with 60 and 90% reduction and annealed at different temperatures.

When α' martensite reverts to austenite during annealing two kinds of transformation texture can be expected. The austenite formed can recrystallize at the same time while the reversion process proceeds. If this simultaneous process occurs, the recrystallization texture is formed, whose intensity depends on the amount of strain accumulated before recrystallization. In this case, austenite shows Cube {100}<001> texture, which comes from Rotated Cube {001}<110> , Goss {110}<001> and Rotated Goss {011}<011> in α' martensite. On the other hand, if there is no austenite recrystallization, this phase develops a relatively sharp texture containing Brass {110}<112>, Copper {112}<111> and S {123}<634>, besides Goss {110}<001> component, as shown in Figure 7.12. The main components in α' martensite which give rise to texture in austenite, without recrystallization, are {332}<113> and {113}<110>, which promote in austenite Brass {110}<112> and Copper {112}<111 >, respectively. Grains with orientations belonging to α Fiber (<110> parallel to rolling direction) also give rise to the Copper in austenite. The transformation component S {123}<634> also tends to have their formation from α'martensite orientations cited above, close to {112}<131> and also close to α Fiber components. The Goss {110}<001> component in the austenite originates in α' martensite being part of them form Rotated Cu {112}<011>, or in components of γ

Fiber ({111} parallel to rolling plane), such as {111}<110>, and some parts also in α Fiber[11,36-39].

Figure 7.13 summarizes the major components involved in transformation texture relationship when there is no austenite recrystallization[39].

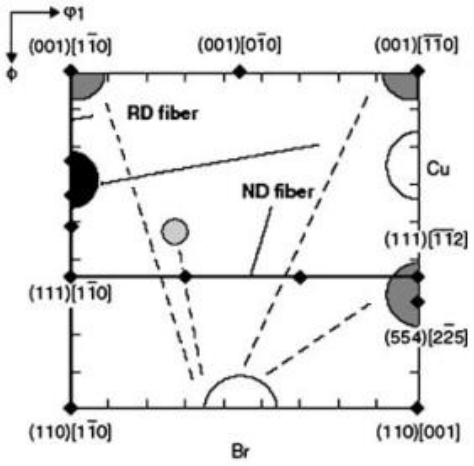


Figure 7.13. Section ϕ2 = 45° of Euler space: transformation texture relationship when there is no austenite recrystallization[39].

Thus, according to Figures 7.11 and 7.12, it was verified that the reversion of austenite occurs without simultaneously recrystallization. It can be proven because the Cube component is observed only in austenite for the sample 60% cold rolled and annealed at the higher temperature, 1000°C. This indicates that austenite recrystallization occurs only in such high temperature for this steel submitted to the already described thermomechanical treatment. It is also important to emphasize that the α' martensite rolling texture is similar to ferritic steels subjected to high cold reductions in thickness (Fig. 7.11(a,b))[11,36].

Figure 7.12 (a-c) show that for samples cold rolled with 60% reduction and the least recrystallized (60 and 90% cold reduction, annealed at 625°C) there is a representative presence of grains with Goss orientation in austenite and that as reversion proceeds this component tends to decrease in intensity and giving way to the Brass component arise. This trend is clearer in section $\phi_2$=0 of ODFs. This fact is beneficial because is desirable

to have a higher Brass intensity in the final texture, since it becomes {332}<113> in α' martensite and promotes good formability[11]. It is known that two α' martensite transformation components, {001}<110> and {113}<110>, produce significantly greater anisotropy of toughness compared to the third main direction, {332}<113>. Thus, from the point of view of good deep drawing, as well as strength and toughness, the component {332}<113> is the most beneficial among the principal texture components in α' martensite and, consequently, its corresponding in austenite, Brass. In addition, this increase in Brass intensity in austenite (Fig. 7.12) occurs not only due to decreased of Goss component in the same phase, but mainly due to the disappearance of {332}<113> and components belonging to γ Fiber in α' martensite[11,39].

## 7.4. Conclusions

- It was found that the microstructure generated after austenite reversion is more refined for samples which were initially subjected to higher cold reduction due to more intense nucleation.
- Through the boundaries analysis (LAGB, Σ3 and THAGBs) via EBSD it was verified that the nucleation and growing processes are faster for the 625°C annealed sample, initially cold rolled with 90% reduction, due to the greater stored energy during deformation.
- The transformation induced by deformation occurs in two steps $\gamma \rightarrow \varepsilon \rightarrow \alpha'$ and α' martensite tends to be the major phase with the deformation increasing.
- The α' and ε martensite reversion into austenite during annealing is practically complete at 700°C regardless of deformation amount and it occurs faster for samples initially 90% cold rolled.
- The ε and α' martensites start to form again for samples annealed at 800 and 1000°C in the quenching.
- The misorientations at phase boundaries are mostly corresponding to K-S OR between austenite and α' martensite.
- The 60°<111> misorientation in austenite corresponds to Σ3 twin boundaries.

- The 50.51° misorientation angle in α' martensite indicates misorientation between two distinct variants in this phase and the 60° misorientation also corresponds to Σ3 boundaries.
- The approximately 70° in ε martensite is the misorientation angle between two variants formed on different $\{111\}_{\gamma}$, 70°<110> and it assumes the S-N OR.
- The microstructural characterization by TEM showed that the α' martensite have different dislocation density and irregular shape in the 60% cold rolled sample. In addition, the subsequently annealed sample at 625°C showed significant amount of annealing twins corroborating the EBSD results. It was also detected by TEM that there are austenitic grains with low dislocation density.
- It was proved by transformation texture analysis that the reversion of austenite occurs without simultaneously recrystallization because the Cube component was observed only in austenite for the sample 60% cold rolled and annealed at 1000°C, indicating that austenite recrystallization occurs just in such high temperature.
- As reversion proceeds Goss component tends to give place to Brass in austenite. This fact is beneficial because it becomes {332}<113> in α' martensite after phase transformation and could promote good formability as well as high strength and toughness.

**Acknowledgements**

Sara S. F. de Dafé acknowledges the scholarship provided by CAPES Foundation, Ministry of Education of Brazil, process number 0804-12-6 and the use of facilities within the University of Wollongong (UOW) Electron Microscopy Centre, Australia.

## References


1. FROMMEYER, G., BRÜX, U., NEUMANN, P. Supra-ductile and high-strength manganese-TRIP/TWIP steels for high energy absorption purposes, *ISIJ International*, v. 43, n. 3, p. 438-446, 2003.
2. DING, H., DING, H., SONG, D., TANG, Z., YANG, P. Strain hardening behavior of a TRIP/TWIP steel with 18.8% Mn, *Materials Science and Engineering: A*, v. 528, n. 3, p. 868-873, 2011.
3. MA, Y., JIN, J-E., LEE, Y-K. A repetitive thermomechanical process to produce nano-crystalline in a metastable austenitic steel, *Scripta Materiallia*, v. 52, p. 1311-1315, 2005.
4. DI SCHINO, A., BARTERI, M., KENNY, J. M. Development of ultra fine grain structure by martensitic reversion in stainless steel, *Journal of Materials Science Letters*, v. 21, n. 9, p. 751-753, 2002.
5. JOHANNSEN, D. L., KYROLAINEN, A., FERREIRA, P. J. Influence of annealing treatment on the formation of nano/submicron grain size AISI 301 austenitic stainless steels, *Metallurgical and Materials Transactions A*, v. 37A, p. 2325-2338, 2006.
6. KNUTSSON, A., HEDSTRÖM, P., ODÉN, M. Reverse martensitic transformation and resulting microstructure in a cold rolled metastable austenitic steel, *Steel Research International*, v. 79, n. 6, p. 433-439, 2008.
7. RENARD, K., JACQUES, P.J. On the relationship between work hardening and twinning rate in TWIP steels, *Materials Science and Engineering: A,* v. 542, p. 8-14, 2012.
8. D. BARBIER, N. GEY, S. ALLAIN, N. BOZZOLO, HUMBERT, M. Analysis of the tensile behavior of a TWIP steel based on the texture and microstructure evolutions, *Materials Science and Engineering: A*, v. 500, p. 196-206, 2009.
9. GUTIERREZ-URRUTIA, I., ZAEFFERER, S., RAABE, D. The effect of grain size and grain orientation on deformation twinning in aFe–22 wt.% Mn–0.6 wt.% C TWIP steel, *Materials Science and Engineering: A*, v. 527, p. 3552-3560, 2010.

10. ALBOU, A., GALCERAN, M., RENARD, K., GODET, S., JACQUES, P. Nanoscale characterization of the evolution of the twin–matrix orientation in Fe–Mn–C twinning-induced plasticity steel by means of transmission electron microscopy orientation mapping, *Scripta Materialia*, v. 68, n. 6, p. 400-403, 2013.
11. RAY, R. K., JONAS, J. J., BUTRÓN-GUILLÉN, M. P., SAVOIE, J. Transformation Texture in Steels, *ISIJ International*, v. 34, n. 12, p. 927-942, 1994.
12. NISHIYAMA, Z. Martensitic transformation. New York: Academic Press, 1978.
13. VERBEKEN, K., BARBÉ, L., RAABE, D. Crystallographic characterization of a phosphorus added TRIP steel, *Ceramic Transactions*, v. 200, p. 333-340, 2009.
14. VERBEKEN, K., BARBÉ, L., RAABE, D. Evaluation of the Crystallographic Orientation Relationships between FCC and BCC phases in TRIP Steels, *ISIJ International*, v. 49, n. 10, p. 1601-1609, 2009.
15. VERBEKEN, K., CAENEGEM N. V., RAABE, D. Identification of ε martensite in a Fe-based shape memory alloy by means of EBSD. *Micron*, v. 40, p. 151-156, 2009.
16. PALUMBO, G., AUST, K.T. Structure-dependence of intergranular corrosion in high purity nickel, *Acta Metallurgica et Materialia*, v. 38, p. 2343-2352, 1990.
17. SAHU, P., SHEE, S.K., HAMADA, A.S., ROVATTI, L., SAHU, T., MAHATO, B., CHOWDHURYF, S. G., PORTER, D.A., KARJALAINEN, L.P. Low strain rate deformation behavior of a Cr-Mn austenitic steel at -80°C, *Acta Materialia*, v. 60, n. 20, p. 6907‑6919, 2012.
18. SATO, A., SOMA, K., MORI, T. Hardening due to pre-existing ε-martensite in an Fe-30Mn-1Si alloy single crystal, *Acta Metallurgica*, v. 30, p. 1901-1907, 1982.
19. DINI, G., NAJAFIZADEH, A., MONIR-VAGHEFI, S.M., UEJI, R. Grain size effect on the martensite formation in a high-manganese TWIP steel by the Rietveld method. *Materials Science and Technology*, v. 26, p. 181-186, 2010.
20. SAHU, P., HAMADA, A.S., GHOSH, R.N., KARJALAINEN, L. P. X-ray diffraction study on cooling-rate-induced γ fcc → ε hcp martensitic

transformation in cast-homogenized Fe-26Mn-0.14C austenitic steel. *Metallurgical and Materials Transactions A*, v. 38, p. 2007-1991, 2000.

21. HAMADA, A.S., SAHU, P., CHOWDHURY, S. G., KARJALAINEN, L.P., LEVOSKA, J., OITTINEN, T. Kinetics of the α' martensitic transformation in fine-grained Fe-26Mn-0.14C austenitic steel. *Metallurgical and Materials Transactions A*, v. 39, p. 462-465, 2008.
22. SAHU, P., HAMADA, A. S., CHOWDHURY, S. G., KARJALAINEN, L. P. Structure and microstructure evolution during martensitic transformation in wrought Fe-26Mn-0.14C austenitic steel: an effect of cooling rate. *Journal of Applied Crystallography*, v. 40, p. 354-361, 2007.
23. NARAGHI R., HEDSTRÖM, P., BORGENSTAM, A. Spontaneous and deformation-induced martensite in austenitic stainless steels with different stability, *Steel research International*, v. 82, n. 4, p. 337-345, 2011.
24. LU, F., YANG, P., MENG, L., CUI, F., DING, H. Influences of Thermal Martensites and Grain Orientations on Strain-induced Martensites in High Manganese TRIP/TWIP Steels, *Journal of Materials Science & Technology*, v. 27, n. 3, p. 257-265, 2011.
25. LIANG, X. Structure and Mechanical Properties of Fe-Mn Alloys. Beijing: University of Science and Technology Beijing, 2008. 254p. (Thesis, Degree of Master of Applied Science).
26. HAILE, Y., NAN, J., XIANG, Z. Influence of shear banding on the formation of brass-type textures in polycrystalline f.c.c metals with low stacking fault energy, *Sciencepaper Online*, p. 1-13, 2012.
27. KITAHARA, H., UEJI, R., TSUJI, N., MINAMINO, Y. Crystallographic features of lath martensite in low-carbon steel, *Acta Materialia*, v. 54, n. 5, p. 1279-1288, 2006.
28. MORITO, S., TANAKA, H., KONISHI, R., FURUHARA, T., MAKI, T. The morphology and crystallography of lath martensite in Fe-C alloys, *Acta Materialia*, v. 51, p. 1789-1799, 2003.
29. BRANDON, D. G. The structure of high-angle grain boundaries, *Acta Metallurgica*, v.14, n. 11, p. 1479-1484, 1966.

30. PARK, S. G., LEE, K. H., KIM, M. C., LEE, B. S. Effects of boundary characteristics on resistance to temper embrittlement and segregation behaviour of Ni-Cr-Mo low alloy steel, *Materials Science & Engineering A*, v. 561, p. 277-284, 2013.
31. CHANDRA, T., IONESCU, M., MANTOVANI, D. Crystallographic behaviors of uni-axial deformed high manganese steels, *Materials Science Forum*, v. 706-709, p. 2668-2673, 2012.
32. SEOL, J. B., LEE, B. H., CHOI, P., LEE, S. G., PARK, C. G. Combined nano-SIMS/AFM/EBSD analysis and atom probe tomography, of carbon distribution in austenite/ε-martensite high-Mn steels, *Ultramicroscopy*, v. 132, p. 248–257, 2013.
33. WEINA, Z., ZHENYUN, L., ZHIBO, Z., GUODONG, W. The crystallographic mechanism for deformation induced martensitic transformation observed by high resolution transmission electron microscope, *Materials Letters*, v. 91, p. 158-160, 2013.
34. LEE, T. H., SHINB, E., OHA C. S., HAA, H. Y., KIMA, S. J. Correlation between stacking fault energy and deformationmicrostructure in high-interstitial-alloyed austenitic steels, *Acta Materialia*, v. 58, 3173-3186, 2010.
35. HE Y., GODET, S., JACQUES, P. J., JONAS, J. J. Crystallographic Features of the g-to-a Transformation in a Nb-Added Transformation-Induced Plasticity Steel, *Metallurgical and Materials Transactions A*, v. 37A, p. 2641-2653, 2006.
36. JONAS, J. J. Transformation Texture Associated with Steel Processing. London: Microstructure and Texture in Steels and Other Materials, 2009. p. 3-17.
37. JONAS, J. J. Effect of austenite recrystallization on toughness of pipeline steels, *Materials Science Forum*, v. 753, p. 546-553, 2013.
38. SOMANI, M.C., JUNTUNEN, P., KARJALAINEN, L.P., MISRA, R.D.K., KYRÖLÄINEN, A. Enhanced Mechanical Properties through Reversion in Metastable Austenitic Stainless Steels, *Metallurgical and Materials Transactions A*, v. 40, n. 3, p. 729-744, 2009.
39. CHAPELLIER, PH., RAY, R. K., JONAS, J. J. Prediction of transformation textures in steels, *Acta Metallurgica et Materialia*, v.38, p. 1475-1490, 1990.

# CHAPTER 8: FINAL CONSIDERATIONS

## 8.1. Summary of results

From the thermodynamic, kinetic, crystallographic, microstructural and mechanical studies the main conclusions were:

- The stacking fault energy for the TRIP/TWIP steel in study was estimated to be 14.5 $mJ/m^2$, indicating the possible occurrence of martensitic transformation as deformation mechanism before twinning.
- Both ε and α′ martensite formed after different cooling rates are assisted by some strain resulting from solidification or thermal contraction.
- The phase-transformation kinetics is favored by a longer cooling time, as inside furnace.
- The hardening ability is enhanced due to the TRIP effect resulting from strain-induced martensitic transformation producing a high work hardening exponent, n = 0.33.
- α' martensite into austenite reversion occurs via shearing together with diffusion mechanism.
- Austenite reversion is more effective and faster at higher temperatures when it has greater stored energy from deformation process.
- The dislocation density is high in austenite, even for samples after annealing, proven that the presence of the shear reversion mechanism is noteworthy.
- It was found that the microstructure generated after austenite reversion is more refined for samples which were initially subjected to higher cold reduction due to more intense nucleation. In addition the nucleation and growth processes are faster during annealing for samples initially cold rolled with higher reduction, due to the greater stored energy during deformation.
- The martensitic transformation occurs in two steps $\gamma \rightarrow \varepsilon \rightarrow \alpha'$ and α' martensite tends to be the major phase with the deformation increasing.
- The α' and ε martensite reversion into austenite during annealing is practically complete at 700°C regardless of deformation amount in cold rolling.

- The ε and α' martensites form by quenching after annealing at temperatures higher than 800°C.
- The misorientations at phase boundaries are mostly corresponding to K-S OR between austenite and α’ martensite and to S-N OR between ε martensite and austenite.
- The reversion of austenite occurs without simultaneously recrystallization once the Cube component was not observed in full annealed samples, just at 1000°C.
- As reversion proceeds Goss component tends to give place to Brass in austenite. This fact is beneficial because it becomes {332}<113> in α’ martensite after phase transformation and could promote good formability as well as high strength and toughness.

### 8.2. Suggestions for future investigations

- Evaluate via interrupted tensile tests the deformation mechanisms involved and to estimate via XRD/MAUD the stacking fault probability in austenite for low deformation.
- Investigate through EBSD the internal misorientation and/or the difference in grain size associated austenitic grains, separating them in those formed due the reversion of α’ martensite from those recrystallized. Thus, according to the texture evolution to determine more accurately the temperature at which reversed austenite starts to recrystallize. This is possible because the higher is the internal misorientation it means that this austenitic grain could just be from reversion process and not recrystallized.
- Evaluate if variant selection occurs during the reversion process of austenite by EBSD and/or TEM.

### 8.3. Original contribution from this thesis

1) "Effect of cooling rate on (ε, α') martensite formation in twinning/transformation-induced plasticity Fe-17Mn-0.06C steel”

- Authors: Sara S. F. Dafé, Felipe L. Sicupira, Flávia C. S. Matos, Naiara S. Cruz, Débora R. Moreira, Dagoberto B. Santos
- Paper published by *Materials Research*. Ahead of print.

2) "Martensite Formation and Recrystallization Behavior in 17Mn0.06C2Si3Al1Ni TRIP/TWIP Steel after Hot and Cold Rolling"
- Authors: Sara S. F. Dafé, Débora R. Moreira, Mariana S. Matoso, Berenice M. Gonzales, Dagoberto B. Santos
- Paper published by *Materials Science Forum*, p. 185-190, 2013.

3) "Microstructural characterization and mechanical behavior of 17% Mn Steel with low C"
- Authors: Mirelle O. Spindola, Sara S. F. Dafé, Denilson J. Carmo, Dagoberto B. Santos
- Paper submitted to *Materials Research*.

4) "Caracterização microestrutural e comportamento mecânico de um aço baixo C contendo 17%Mn laminado a morno, a frio e recozido"
- Authors: Mirelle O. Spindola, Sara S. F. Dafé, Dagoberto B. Santos
- Paper published in the Proceedings of the *48° Seminário de Laminação - ABM*, Santos, Brazil, October 2011.

5) "Martensite Formation and Recrystallization Behavior in 17Mn0.06C2Si3Al1Ni TRIP/TWIP Steel after Hot and Cold Rolling"
- Authors: Sara S. F. Dafé, Débora R. Moreira, Mariana S. Matoso, Berenice M. Gonzales, Dagoberto B. Santos
- Paper published in the Proceedings of the *5th International Conference on Recrystallization & Grain Growth*, Sydney, Australia, 2013.

6) "Deformation and recrystallization behavior of a TRIP/TWIP steel with 17% Mn and low C"

- Authors: Mirelle O. Spindola, Sara S. F. Dafé, Denilson J. Carmo, Dagoberto B. Santos

- Abstract published in the Proceedings of the *XII Encontro da SBPMat*, Campos do Jordão, Brazil, September, 2013.

This work received the Prize of Best Work of the Symposium E: Structure- properties relationship of advanced metallic materials

7) "Efeito da laminação a frio na formação de martensita, recristalização e comportamento mecânico do aço TRIP/TWIP 17Mn0.06C"

- Authors: Sara S. F. Dafé, Débora R. Moreira, Patrícia Bertolini Valadão, Dagoberto Brandão Santos

- Paper published in the Proceedings of the *50° Seminário de Laminação – ABM*, Ouro Preto, Brazil, November, 2013.


XII Encontro da SBPMat
Campos do Jordão
2013
Certificate
Hereby we certify that the work
Deformation and recrystallization behavior of a TRIP/TWIP steel with 17% Mn and low C,
having as author(s)
Mirelle Oliveira Spindola, Sara Silva Ferreira de Dafé, Denilson José do Carmo and Dagoberto Brandão Santos
received the Prize of Best Work of the Symposium E
at the XII Brazilian MRS Meeting, in Campos do Jordão-SP, from September 29th to October 3rd 2013.
José Alberto Giacometti
Conference Chair
Julio Ricardo Sambrano
Conference Chair
Roberto Mendonça Faria
Brazil MRS President